Plasmon-exciton coupling: from DNA origami to graphene nanoribbons

Dissertation

zur

Erlangung des Doktorgrades (Dr. rer. nat.)

der

Mathematisch-Naturwissenschaftlichen Fakultät

der

Unversität zu Köln

von

Mo Lu

aus

Nei Mongol, China

Köln, October 2020

Dieser Forschungsbericht wurde als Dissertation von der Mathematisch-Naturwissenschaftlichen Fakultät der Universität Köln angenommen und ist auf dem Hochschulschriftenserver der KUPS Köln `https://kups.ub.uni-koeln.de` elektronisch publiziert.

1. Supervisor:	Prof. Dr. Klas Lindfors
2. Supervisor:	Prof. Dr. Malte Gather
Tag der Promotion:	24. 11. 2020
Erscheinungsjahr:	2021

Erklärung zur Dissertation
gemäß der Promotionsordnung vom 12. März 2020

Diese Erklärung muss in der Dissertation enthalten sein.
(*This version must be included in the doctoral thesis*)

„Hiermit versichere ich an Eides statt, dass ich die vorliegende Dissertation selbstständig und ohne die Benutzung anderer als der angegebenen Hilfsmittel und Literatur angefertigt habe. Alle Stellen, die wörtlich oder sinngemäß aus veröffentlichten und nicht veröffentlichten Werken dem Wortlaut oder dem Sinn nach entnommen wurden, sind als solche kenntlich gemacht. Ich versichere an Eides statt, dass diese Dissertation noch keiner anderen Fakultät oder Universität zur Prüfung vorgelegen hat; dass sie - abgesehen von unten angegebenen Teilpublikationen und eingebundenen Artikeln und Manuskripten - noch nicht veröffentlicht worden ist sowie, dass ich eine Veröffentlichung der Dissertation vor Abschluss der Promotion nicht ohne Genehmigung des Promotionsausschusses vornehmen werde. Die Bestimmungen dieser Ordnung sind mir bekannt. Darüber hinaus erkläre ich hiermit, dass ich die Ordnung zur Sicherung guter wissenschaftlicher Praxis und zum Umgang mit wissenschaftlichem Fehlverhalten der Universität zu Köln gelesen und sie bei der Durchführung der Dissertation zugrundeliegenden Arbeiten und der schriftlich verfassten Dissertation beachtet habe und verpflichte mich hiermit, die dort genannten Vorgaben bei allen wissenschaftlichen Tätigkeiten zu beachten und umzusetzen. Ich versichere, dass die eingereichte elektronische Fassung der eingereichten Druckfassung vollständig entspricht."

Teilpublikationen:

Xin, Ling, Mo Lu, Steffen Both, Markus Pfeiffer, Maximilian J. Urban, Chao Zhou, Hao Yan, Thomas Weiss, Na Liu, and Klas Lindfors. "Watching a single fluorophore molecule walk into a plasmonic hotspot." ACS Photonics 6, no. 4 (2019): 985-993.

Lu, Mo, Markus Pfeiffer, Boris V. Senkovskiy, Danny Haberer, Dirk Hertel, Klaus Meerholz, Felix R. Fischer, Yoichi Ando, Alexander Grüneis, and Klas Lindfors. "Probing the origin of photoluminescence blinking in graphene nanoribbons: Influence of plasmonic field enhancement." 2D Materials 7, no. 4 (2020): 045009.

Datum, Name und Unterschrift

Mo Lu
02.10.2020

Mo
LU

Digitally signed by Mo LU
DN: C=DE, OU=Physical Chemistry department, O=University of Cologne, CN=Mo LU, E=lumo0417@gmail.com
Reason: I agree to the terms defined by the placement of my signature in this document
Location: your signing location here
Date: 2020-10-02 00:16:47
Foxit Reader Version: 9.7.1

Abstract

Plasmonic nanostructure can serve as optical antennas that convert freely propagating optical radiation into localized energy. Coupling between plasmon and an exciton leads to a strong modification of the decay rate, emission direction, and quantum efficiency of an emitter. The coupling efficiency varies drastically on a length scale that is much smaller than the incident wavelength. Combined with single-molecule techniques, plasmon-exciton coupling provides a versatile platform for studying nanoscale motions and interactions.

In this dissertation, we have investigated dynamic light-matter interaction nanosystems enabled by the DNA origami nanotechnology. We first studied a dynamic plasmonic walker structure, where a plasmonic nanorod can walk progressively and reversibly on a DNA origami template and interact with a fluorophore assembled along the walking track. We tracked the dynamic motion on individual walker devices by monitoring the change of brightness and fluorescence dynamics, which can not be resolved by the ensemble-level observation reported earlier [1]. Additionally, we demonstrated a dynamic DNA-origami directed nanomachine, where a single fluorophore molecule can autonomously and unidirectionally walk into the hotspot of a plasmonic nanoantenna along a designed origami track. Successive fluorescence intensity increase and lifetime reduction are *in situ* monitored using single-molecule fluorescence spectroscopy, while the fluorophore walker gradually approaches and eventually enters the plasmonic hotspot. Our approach offers a dynamic platform that can be used to develop functional materials, investigate intriguing light-matter interaction phenomena, and serve as a prototype system for examining theoretical models.

The highly confined plasmonic hotspot also allows probing inherent weak features. By coupling plasmonic nanoantennas to semiconducting armchair graphene nanoribbons (AGNRs), we observed blinking of spectrally narrow photoluminescence from the AGNRs next to the metal nanostructure [2]. Such blinking is a typical signature of emissions from single quantum emitters. In this dissertation, we probe in detail the origin of the blinking. In particular, we clarify the relative roles in field enhancement in the vicinity of a plasmonic nanoantenna. We conclusively demonstrate that the field enhancement alone enables being able to observe photoluminescence blinking. Thus, the blinking is an intrinsic feature of light emission from the graphene nanoribbons and not due to, e.g., contact with the environment. This work has thus provided a key contribution in understanding light emission in

seven atom-atom wide armchair-edge graphene nanoribbons.

Contents

CHAPTER 1

Introduction

As Moore's law states, the number of transistors in integrated circuits doubles approximately every two years [3]. Driven by the demands of miniaturization and integration of electronic units, nanoscience and nanotechnology have received massive attention in recent decades. This inevitably requires a rigorous study of the interaction of light with nanoscale objects. In particular, it is essential to understand optically induced excitations in nanomaterials. For example, light can induce collective oscillation of conduction electrons in metal nanostructures, so-called surface plasmon resonance. Localized surface plasmons allow focusing light into a sub-wavelength volume so that the metal nanostructures can work as nanoantennas at optical frequencies [4]. More importantly, light can induce the formation of bound electron-hole pairs in quantum emitters such as molecules or semiconductor nanocrystals, so-called excitons. The exciton can undergo radiative recombination, resulting in a narrow bandwidth and bright light emission. Moreover, some excitonic materials exhibit size dependent transition frequencies, which have attracted particular attention in biological sensing [5, 6] and integrated photonic circuits [7–9].

The coupling of surface plasmon to excitons brings new features and new functionalities. The coupling process can be understood analogous to a radio-frequency antenna configuration: the quantum emitter serves as a receiver or transmitter and interacts with free optical radiation via a plasmonic metal nanostructure, which acts as an optical antenna. The antenna converts the propagating electromagnetic fields into localized energy so that the receiving efficiency is enhanced. Reciprocally, it can substantially enhance and impedance matching the outgoing radiation of a transmitter. Plasmon-exciton coupling enables the control of light-matter interaction on the a single quantum system level and a strong modification of the properties of the quantum emitter, including transition rates [10–16], and energy-level structures [17].

A key challenge for applying and exploring plasmon-exciton coupling is to fabricate nanosystems

with plasmonic and excitonic components with controllable shape, size, number, and arrangement. In particular, it is crucial to control the relative position between a plasmonic particle and an emitter with nanometer precision. Traditional top-down fabrication techniques have often been used for this aim, but it is difficult achieving the required accuracy. Also, precisely placing a quantum emitter in a plasmonic hotspot is still formidable to achieve. Either metal nanostructures are fabricated around randomly located emitters, or emitters are deposited randomly on top of prefabricated gold nanostructures [13–15, 18–21].

In contrast, DNA nanotechnology intrinsically gives nanometer accuracy and three-dimensional positioning capabilities [22, 23]. In a method called DNA origami, sets of single-stranded DNA oligonucleotides can serve as staples to direct the folding path of a long single-stranded viral DNA 'scaffold' strand forming a predesigned DNA architecture with almost arbitrary shape and full addressability. Additionally, the origami template can serve as a 'molecular breadboard' to position a variety of nanoparticles, including metal particles and excitonic emitters. Most importantly, in combination with dynamic DNA nanotechnology, it is possible to realize dynamic control of the light-matter interaction by fabricating reconfigurable structures [1, 16, 24–26]. DNA origami technology is a versatile tool to tackle the aforementioned technological challenges and open new pathways to realizing hybrid plasmon-exciton nanosystems with novel functionalities.

Another means to optimize plasmon-exciton interactions is to employ novel excitonic materials for coupling to surface plasmons. Two-dimensional (2D) materials including graphene, transition metal dichalcogenides (TMDs), black phosphorus, and hexagonal boron nitride have been intensively investigated for this aim. 2D materials with atomic thickness show extraordinary optical properties such as single-photon emission from localized excitons or defects [27–29], valley polarized photoluminescence [30–32], and distinctive Raman signals [33, 34]. Most importantly, coupling surface plasmons to 2D materials not only circumvents the challenge of extremely low absorption efficiency but also brings new features. For example, it allows to probe inherently weak features such as exciton energy transfer [35], and emission with low quantum yield [2]. Additionally, 2D materials support electroluminescence [36], and it is straightforward to integrate 2D materials into lithographically fabricated nanostructures. This enables to generate and collect light locally, which holds the promise for applications in integrated nanoscale optoelectronics.

One dimensional semiconducting armchair graphene nanoribbons (GNRs) with well-defined structures are examples of novel excitonic materials. They can be fabricated by surface-assisted bottom-up fabrication techniques with atomic precision [37–48]. In this way, doping, control of the edge topology, and even nanoribbon heterostructures can be achieved, which allows obtaining, e.g., metallic, semiconducting, and emissive nanoribbons by proper choice of precursors [38, 49–56]. Coupling plasmonic antennas to GNRs allows probing weak optical transitions, which is very important for understanding the light emission process in GNRs.

In this dissertation, we present several applications that are enabled by plasmon-exciton coupling.

We start with an introduction to the fundamental theory and the terminologies. We continue with a chapter on the optical experimental methods that are employed throughout this dissertation.

In the subsequent chapter, we have presented a study on the dynamic light-matter interaction nanosystems that are fabricated by DNA origami self-assembly techniques. Most previous works in this area either stick to static structures or track the dynamic motion of an active plasmonic structure at the ensemble-level [57–62]. Here we focus on tracking the dynamic motion of individual devices using single-molecule techniques. We first studied a plasmonic walker system, where the interaction of an isolated fluorophore molecule and a plasmonic nanorod can be modulated by moving the nanorod in steps of 7 nm along an origami template. A numerical simulation is carried out to understand the optical interaction during the walking process. Then a number of static devices were characterized to study the position-dependent fluorescence lifetime distribution. At last, we performed a dynamic operation on individual walker devices, including a walker-release experiment and walking experiment, and in real-time tracked the change in fluorescence.

We also studied another DNA-origami directed dynamic nanomachine, where a single fluorophore molecule can be autonomously and unidirectionally transported into the hotspot of a plasmonic gap antenna along a designated origami track. We first demonstrated the walking mechanism at the ensemble-level with Förster resonance energy transfer (FRET). Then we tracked the individual device by recording fluorescence micrographs and fluorescence decay traces on individual device level during the walking process. Additionally, we determined the fluorescence brightness and fluorescence lifetime for a large number of devices before and after the walking, and measured the same data for static devices with the emitter positioned either at the start or stop position.

Finally, we studied the origin of photoluminescence blinking from aligned seven-atom wide armchair-edge graphene nanoribbons when they are coupled to a plasmonic antenna. We tuned the plasmon's spectral position through the fluorescence spectrum of the GNRs by varying the size and material of the optical antenna, leading to a change in the plasmonic field enhancement. Additionally, we performed single-molecule localization studies to investigate the correlation between emission localization shifts and the plasmonic field enhancement.

CHAPTER 2

Basics

This chapter summarizes the fundamental concepts that are important to this dissertation. We start by the quantum electrodynamics (QED) description of light-matter interaction, which are focus on the spontaneous decay of a two-level quantum system in an environment described by a local photon density of states. Next, we turn to the basics of plasmonics starting from the optical properties of plasmonic materials. We discuss localized surface plasmon resonances in sub-wavelength metal particles, followed by an overview of the plasmonic antennas. We then proceed with a discussion of coupling a quantum emitter to a plasmonic antenna from the perspective of emission modification. In the following part, we will present a brief review of the DNA origami-directed method to realize the light-matter interaction nanosystem. A short introduction of nanostructured graphene and its optical properties will be given at the end.

2.1 Light-matter interaction

Light interacts with a quantum system such as an atom that can give rise to a resonant light-matter interaction if the frequency of light coincides with the atom's optical transition. Two-level atom approximation[1] assumes that only resonant levels of the atom are relevant to the interaction. By absorbing or emitting a photon, an atom can make a transition from an energy state E_i to E_f. The angular frequency ω of the optical fields satisfies [65, 66]

$$\hbar\omega = E_f - E_i. \tag{2.1}$$

[1] Two-level approximation only holds under the following conditions: (1) the dipole approximation holds, that is, the atomic dimension is much smaller than the incident wavelength; (2) the rotating wave approximation holds, that is, just near-resonant term is relevant for the description of the interaction [64].

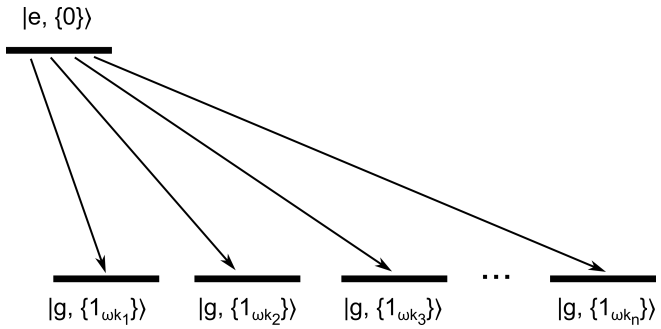

Figure 2.1: Transition from an initial state $|i\rangle = |e, \{0\}\rangle$ to a number of final sates $|f\rangle = |g, \{1_{\omega k}\}\rangle$ with the same energy E_g. Adapted from Ref. [63].

The process that an atom is promoted from a ground state to an excited state by absorbing a photon is called absorption, while the radiative process that the atom relaxes from an excited state to the lower state is called spontaneous emission. Based on time-dependent perturbation theory, the transition rate of spontaneous emission γ from an initial sate $|i\rangle$ with an angular frequency of ω_i to a final state $|f\rangle$ with an angular frequency of ω_f is given by Fermi's golden rule [67]

$$\gamma = \frac{2\pi}{\hbar^2} \sum_f |\langle f|\hat{H}|i\rangle|^2 \delta(\omega_i - \omega_f), \tag{2.2}$$

where $\hat{H}$ is the interaction Hamiltonian and $\delta(\omega_i - \omega_f)$ is the Dirac delta function. In the dipole approximation, the interaction Hamiltonian is $\hat{H} = -\hat{\mathbf{p}} \cdot \hat{\mathbf{E}}$ where $\hat{\mathbf{p}}$ is dipole moment operator and $\hat{\mathbf{E}}$ is the electric field operator. The initial state is a product of excited state and a zero-photon state $|e, \{0\}\rangle$. Similarly, the final states can be written as a product of ground state and the single photon states associated with different wavevector k and frequency ω, given as $|f\rangle = |g, \{1_{\omega k}\}\rangle$ (see Figure 2.1). $\delta(\omega_i - \omega_f)$ accounts for the energy conservation statement that the energy difference between excited and ground state has to be the same as the energy of the emitted photon $\hbar\omega$. By introducing partial local density of states (LDOS) ρ_p, the transition rate at position $\mathbf{r}_0$ and transition frequency ω can be written as

$$\gamma = \frac{\pi\omega}{3\hbar\varepsilon_0} |\mathbf{p}|^2 \rho_p(\mathbf{r}_0, \omega). \tag{2.3}$$

Here $\mathbf{p} = \langle e|\hat{\mathbf{p}}|g\rangle$ denotes the transition dipole matrix element. The local density of states ρ_p represents the number of available electromagnetic states per unit volume and frequency when the quantum system has a fixed dipole axis $\mathbf{n}_p$. It can be determined using the system's dyadic Green's function $\overleftrightarrow{G}$ as [63, 68]

$$\rho_p(\mathbf{r}_0, \omega) = \frac{6\omega}{\pi c^2} [\mathbf{n}_p \cdot \mathrm{Im}\{\overleftrightarrow{G}(\mathbf{r}_0, \mathbf{r}_0; \omega)\} \cdot \mathbf{n}_p], \tag{2.4}$$

Eq.(2.3) and Eq.(2.4) reveal that the spontaneous decay rate of an atom is determined by the transition dipole moment and the electromagnetic environment. In the case of free space, we obtain

$$\rho = \frac{\omega^2}{\pi^2 c^3} \text{ and } \gamma_0 = \frac{\omega^3 |\mathbf{p}^2|}{3\pi\varepsilon_0 \hbar c^3}. \tag{2.5}$$

Modification of electromagnetic environment such as coupling the atom to dielectric cavities [69, 70], photonic crystals [71] or plasmonic structures [12] leads to a change of spontaneous decay rate compared to free space. The figure of merit $F_p = \gamma/\gamma_0$ is known as Purcell factor. Here only the weak coupling regime where the coupling constant is much larger than the radiative rate. In the strong coupling regime where a reversible energy exchange between the atom and environment occurs, new hybridized states will emerge. In this dissertation, we will focus on modifying spontaneous emission by coupling to a plasmonic nanoantenna in the weak coupling regime. Theoretical discussion will be found in Section 2.3.

2.2 Plasmonics

Metal nanoparticles support collective oscillations of conduction electrons known as localized surface plasmons. The electromagnetic field is enhanced in the vicinity of the particle when plasmon oscillation takes place. The metal nanostructure thus efficiently converts propagating electromagnetic fields to localized energy. Reciprocally, a plasmonic nanoparticle can substantially enhance and outgoing radiation of a local emitter to the far-field. Plasmonic nanoparticles are thus often called optical antennas in analogy to radio frequency antennas. There is another class of surface plasmon that propagates at the planar metal-dielectric interface, so-called surface plasmon polariton. It finds application in nanoscale waveguides [72, 73], gratings [74], and metamaterials with a variety of functionalities [75, 76]. Together with surface plasmon polariton, localized surface plasmon forms the field of plasmonics. In this dissertation, we will focus exclusively on metal nanoparticles.

2.2.1 Optical properties of bulk metal

We first study the interaction of bulk metal with light, which is described by the complex dielectric function of metal. At low optical frequencies where interband transitions are not excited, the optical response of a metal can be explained by applying the Drude-Sommerfield model [77]. Here unbounded conduction electrons are treated as electron gas that move freely in a fixed array of atomic core. Electrostatic interactions between electrons and lattice potential are neglected. The motion of a free conduction band electron under an external electric field $\mathbf{E}(t) = \mathbf{E}_0 e^{-i\omega t}$ is therefore described by the equation of motion [63],

$$m_e \ddot{\mathbf{r}} = -\Gamma m_e \dot{\mathbf{r}} + e\mathbf{E}_0 e^{-i\omega t}, \tag{2.6}$$

where e and m_e is the charge and effective mass of free electrons respectively, and Γ is the damping constant. $\mathbf{E}_0$ and ω are the amplitude and angular frequency of the incident field. The displacement of the electron $\mathbf{r}$ can be solved to be

$$\mathbf{r} = \frac{e\mathbf{E}_0 \exp(-i\omega t)}{m(\omega^2 + i\Gamma\omega)}. \tag{2.7}$$

For an electron gas with density n, the induced macroscopic polarization $\mathbf{P}(\omega)$ will be

$$\mathbf{P}(\omega) = -ne\mathbf{r} = \frac{ne^2\mathbf{E}_0 \exp(-i\omega t)}{m(\omega^2 + i\Gamma\omega)}. \tag{2.8}$$

The macroscopic polarization can also be expressed in terms of the material's electric susceptibility χ_e,

$$\mathbf{P}(\omega) = \varepsilon_0 \chi_e \mathbf{E}(t). \tag{2.9}$$

Combining (2.8) and (2.9), χ_e can be expressed as

$$\chi_e = \frac{ne^2}{m_e \varepsilon_0} \left[-\frac{1}{\omega^2 + \Gamma^2} + i\frac{\Gamma}{\omega(\omega^2 + \Gamma^2)} \right]. \tag{2.10}$$

From this we obtain frequency dependent complex dielectric function of the metal $\varepsilon_{\text{Drude}}(\omega)$ as,

$$\varepsilon_{\text{Drude}}(\omega) = 1 + \chi_e = 1 - \frac{\omega_p^2}{\omega^2 + \Gamma^2} + i\frac{\Gamma\omega_p^2}{\omega(\omega^2 + \Gamma^2)}, \tag{2.11}$$

where $\omega_p = \sqrt{\frac{ne^2}{m_e \varepsilon_0}}$ is the plasma frequency of bulk metal. When ω is smaller than the plasma frequency ω_p, the negative real part $\text{Re}(\varepsilon)$ leads to a large imaginary part of the refractive index $n = \sqrt{\varepsilon}$, so that light can not penetrate into the metal significantly. Above ω_p, the metal becomes transparent. At plasma frequency ω_p, a collective oscillation of free electrons can be induced, so called volume plasmon. Light can propagate through metal as a strongly damped collective charge density fluctuation [78, 79], but can not be coupled to the volume plasmon directly as it is longitudinal. However, it is possible to couple light to spatially confined plasmon at the metal-dielectric interface, so-called surface plasmon polariton, or plasmon localized on the surface of metal nanostructure, so-called localized surface plasmon. The excitation of surface plasmons requires the metal to possess a large negative $\text{Re}(\varepsilon)$ and a small $\text{Im}(\varepsilon)$ [63], which is usually fulfilled for metals like gold in visible frequency. The excitation of localized surface plasmon in metal nanoparticle will be discussed in Section 2.2.2.

We plot in Figure 2.2 the imaginary and real parts of the dielectric function of gold as a function of photon energy according to Equation (2.11) together with experimental data. The experimental data is in good agreement with the Drude model in the region with photon energy is smaller than 2 eV. In the

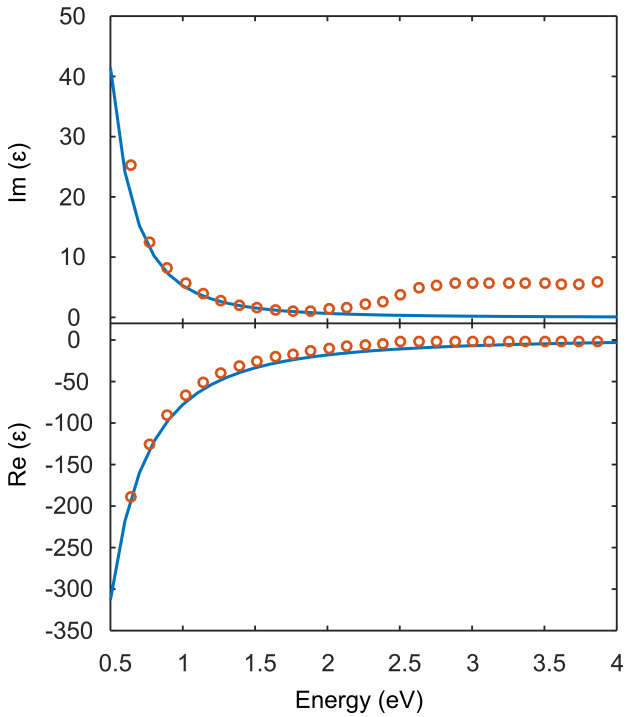

Figure 2.2: Imaginary part (top) and real part (bottom) of the dielectric function of gold. Experimental data (red circle) is taken from Johnson and Christy (1972) [80]. The solid line is calculated using equation (2.11) with $\hbar\omega_p$ = 8.95 eV and $\hbar\Gamma$ = 65.8 meV [63].

region above 2 eV, the experimental data deviate from the metal strongly due to interband transitions[2]. For higher optical frequency, the bound electrons in d band close to the Fermi surface can be promoted into the sp conduction band. If we consider the transition process as exciting the oscillation of bound electrons, the motion of a bound electron will be influenced by a radiative damping force and binding potential. By introducing an offset constant ε_∞ to account for the integrated effect of all interband transitions [82], the complex dielectric function (2.11) can be rewritten as

$$\varepsilon(\omega) = \varepsilon_\infty - \frac{\omega_p^2}{\omega^2} + i\frac{\Gamma\omega_p^2}{\omega^3}. \tag{2.12}$$

By properly choosing the ε_∞ value, (2.12) gives a better agreement with experimental data than (2.11). Detailed discussion can be found in Refs.[82–85].

[2] The imaginary parts of the experimental determined dielectric constant of gold contain large relative error as the refractive index value in visible and near-infrared region is small [80, 81].

2.2.2 Plasmonic nanoparticles

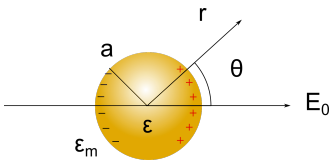

Figure 2.3: Sketch of a metallic sphere in a homogenous external incident field.

We now discuss how light interacts with a metal particle. It can be seen as a scattering problem of a metal nanoparticle in an oscillating electromagnetic field. If the nanoparticle's size is much smaller than the incident wavelength, the interaction can be treated within the quasi-static approximation. It assumes that the phase of the incident field in the particle region is constant so that the problem can be simplified as a particle in an electrostatic field (see Figure 2.3). By solving Laplace equation $\nabla^2\phi = 0$ [86], the induced electric potential inside and outside particle can be solved as

$$\phi_{\text{in}} = -\frac{3\varepsilon_m}{\varepsilon + 2\varepsilon_m}\mathbf{E}_0 r\cos\theta, \tag{2.13}$$

$$\phi_{\text{out}} = -\mathbf{E}_0 r\cos\theta + \frac{\varepsilon - \varepsilon_m}{\varepsilon + 2\varepsilon_m}\mathbf{E}_0 a^3\frac{\cos\theta}{r^2}, \tag{2.14}$$

where ε and ε_m are the dielectric functions of the metal sphere and the surrounding medium. The first term of ϕ_{out} is the potential of the incident field and the second term can be seen as the potential from a static point dipole with dipole moment $\mathbf{p}$ in the center of the nanosphere. Equation (2.14) can be written

$$\phi_{out} = -\mathbf{E}_0 r cos\theta + \frac{\mathbf{p}\cdot\mathbf{r}}{4\pi\varepsilon_0\varepsilon_m r^3}, \tag{2.15}$$

where the dipole moment is defined as,

$$\mathbf{p} = 4\pi\varepsilon_0\varepsilon_m a^3\frac{\varepsilon - \varepsilon_m}{\varepsilon + 2\varepsilon_m}\mathbf{E}_0. \tag{2.16}$$

The distribution of the electric field derived from potential is,

$$\mathbf{E}_{out} = -\nabla\phi_{\text{out}} = \mathbf{E}_0 + \frac{3\mathbf{n}(\mathbf{n}\cdot\mathbf{p}) - \mathbf{p}}{4\pi\varepsilon_0\varepsilon_m}\frac{1}{r^3}. \tag{2.17}$$

Given that $\mathbf{p} = \varepsilon_0\varepsilon_m\alpha E_0$, the polarizability of a metal nanosphere is therefore

$$\alpha = 4\pi a^3\frac{\varepsilon - \varepsilon_m}{\varepsilon + 2\varepsilon_m}. \tag{2.18}$$

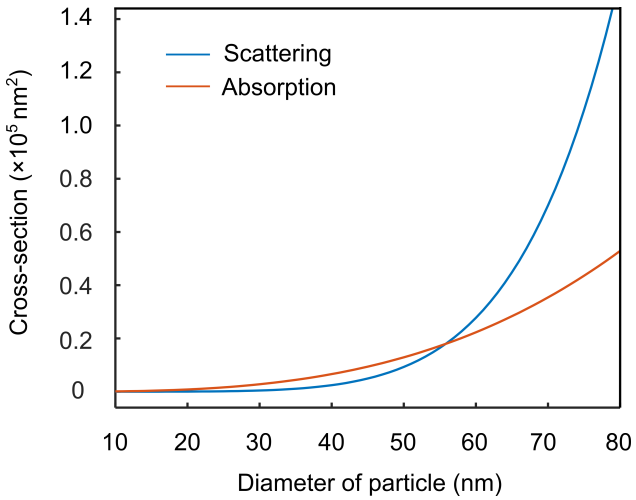

Figure 2.4: The normalized scattering cross-section and absorption cross-section as a function of particle size at 532 nm excitation, according to Eq. (2.19) and Eq. (2.20).

From (2.18), we observe that there is a resonance enhancement of polarizability when $\varepsilon = -2\varepsilon_m$. This is known as the Fröhlich resonance condition and the corresponding resonance mode is known as localized surface plasmon[3]. The resonance frequency is dependent on the dielectric environment but independent of particle size. For a metal sphere in vacuum and using a dielectric function according to the Drude model, this condition is met at frequency $\omega_{\text{res}} = \omega_{\text{p}}/\sqrt{3}$. Under a time-varying plane-wave excitation $\mathbf{E}(t) = \mathbf{E}_0 e^{-i\omega t}$, an induced oscillating dipole moment in the center of the nanosphere becomes $\mathbf{p} = \varepsilon_0 \varepsilon_m \alpha E_0 e^{-i\omega t}$. In reference to the electrostatic results in (2.17) and (2.18), it reveals that surface plasmon of a metal particle originates from a collective excitation of conduction electrons related to resonantly enhanced polarizability, and the scattered field of an induced oscillating dipole.

The scattering cross-section C_{sca} and absorption cross-section C_{abs} can be obtained from the scattered field (second term in (2.17)) radiated by the dipole [88]

$$C_{\text{sca}} = \frac{k^4}{6\pi}|\alpha|^2 = \frac{8\pi}{3}k^4 a^6 \left[\frac{\varepsilon - \varepsilon_m}{\varepsilon + 2\varepsilon m}\right]^2, \tag{2.19}$$

$$C_{\text{sca}} = k\text{Im}\alpha = 4\pi k a^3 \text{Im}\left\{\frac{\varepsilon - \varepsilon_m}{\varepsilon + 2\varepsilon m}\right\}, \tag{2.20}$$

where k is the wavevector of light in the medium. The extinction cross-section is given as the sum of

[3] Here $\varepsilon = 2\varepsilon_m$ is the resonant condition only for dipole surface plasmon. The general rule describing the resonant condition of each n-th multipole term is $\varepsilon = -\frac{n+1}{n}\varepsilon_m$ [87].

scattering and absorption cross-sections:

$$C_{\text{ext}} = C_{\text{sca}} + C_{\text{sca}}. \tag{2.21}$$

The scattering and absorption cross-sections as a function of particle size, according to Eq. (2.19) and Eq. (2.20), are plotted in Figure 2.4. Both absorption and scattering are resonantly enhanced at the surface plasmon resonance frequency, and the magnitude increases with the increase of particle size. Furthermore, we notice that scattering cross-section from a particle of radius varies as a^6, while absorption cross-section varies as a^3. Thus the absorption process is dominant for small particles, and scattering is dominant for larger ones. As a result, the far-field optical method to detect a nanoparticle with dimensions below 40 nm such as photothermal method [89] and interferometric scattering microscopy [90], usually make use of the slower scaling of absorption.

The quasi-static approximation can also be applied to an ellipsoid shape particle under the condition that the longest axis is still far smaller than the incident wavelength. Similarly to the case of a nanosphere, for an ellipsoid with semiaxes a_1, a_2, and a_3, the polarizabilities α_i along the axes ($i = 1, 2, 3$) will be

$$\alpha_i = 4\pi a_1 a_2 a_3 \frac{\varepsilon - \varepsilon_m}{3\varepsilon_m + 3L_i(\varepsilon - \varepsilon_m)}. \tag{2.22}$$

Here, L_i is a geometrical factor for the ith axis to account for the shape of the particle [88]. The resonance condition is now modified as $Re(|\varepsilon_m + L_i(\varepsilon - \varepsilon_m)|) = 0$. As a consequence, the resonance frequency exhibits a dependence on the particle shape. Moreover, (2.22) shows that an ellipsoid particle has plasmon resonances at a different frequencies, corresponding to oscillations of conduction electrons along different axes. The oscillation along the long axis of the particle is called longitudinal plasmon, which occurs in a low-energy regime compared to a sphere of the same volume. On the contrary, the oscillation along the short axis is called transverse plasmon. By tuning the ellipsoid aspect ratio, one can obtain a plasmon resonance ranging from visible to infrared regime.

In summary, light can induce a collective oscillation of conduction electrons in metal particles if the Fröhlich resonance condition is met. Additionally, the absorption and scattering cross-sections are also resonantly enhanced. So far, the quasi-static approximation approach can describe the plasmon resonance of small metal spheres and ellipsoids qualitatively. It can also be applied in the study of the coupling of nanoparticle pairs [91]. However, it does not include the change in resonance frequency and plasmon linewidth concerning particle size. First, the retardation effect in nanoparticle larger than 100 nm is not negligible. It can be considered as a depolarization field inside the particle resulting in a spectral red-shift of the plasmon resonance as particle size increases [92]. Moreover, a significant spectral broadening in plasmon resonance for a large particle is expected, which arises from two competing plasmon damping processes: radiative decay process into photons [93]; non-radiative decay due to intraband or interband excitations [94, 95]. Tuning the relative contribution

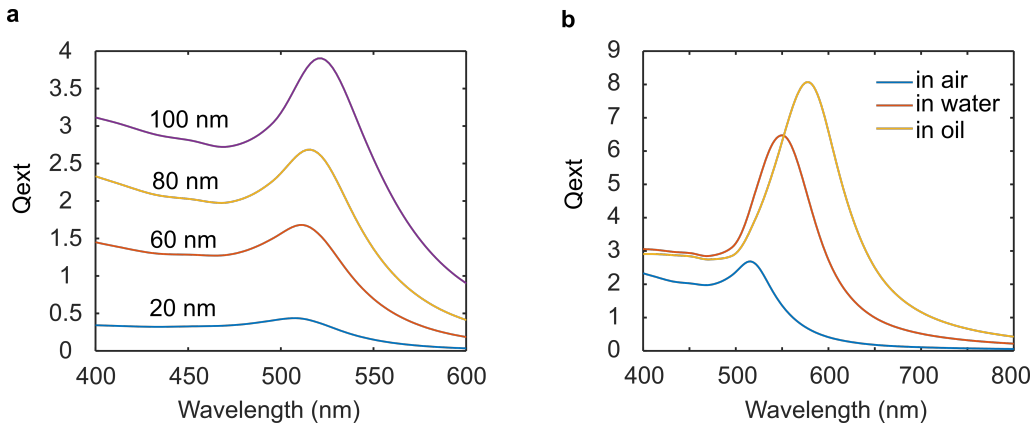

Figure 2.5: (**a**) Dimensionless extinction cross-section Q_{ext} of a gold sphere as a function of wavelength for different particle size: 100 nm, 80 nm, 60 nm, 20 nm from top to bottom. Q_{ext} is extinction cross-section that divided by πa^2, where a is the radius of the sphere. (**b**) Q_{ext} of a gold sphere with a diameter of 80 nm in air, water, oil. The curve is calculated by Mie theory.

of two decay pathways is essential to sensing application [95, 96]. The quantitative description beyond the quasi-static regime is a rigorous electrodynamic approach so-called Mie theory [97]. The dimensionless extinction cross-section $Q_{ext} = \frac{C_{ext}}{pia^2}$ of a gold sphere as a function of wavelength calculated by Mie theory for different particle sizes and the different medium is plotted in Figure 2.5. Here we can observe that the plasmon resonance exhibit a red-shift as the particle dimension increases, different from (2.18). Meanwhile, the spectral width increases and the extinction strength. Additionally, with the same particle dimension, an embedded medium with a higher refractive index results in a stronger plasmon resonance occurring at a higher wavelength regime.

2.2.3 Plasmonic nanoantenna

In analogy to a radio-frequency (RF) antenna, an optical antenna is a transducer between propagating optical radiation and localized energy. The initial interest for optical antenna was to improve the optical microscopy resolution, which is limited by the dimensional mismatch between nano objects and the wavelength of light. Metal nanostructures are often used for this aim as light can couple to surface plasmon modes effectively. They allow to focus the light into nanoscale volume with high spatial and spectral control. The idea of using metal nanostructure as an optical antenna is first demonstrated in near-field optics [98]. Later, the concept has been widely applied in photodetection [99–101], photoluminescence enhancement [10–16], biological sensing [96, 102], and spectroscopies [34, 103, 104].

Like an RF antenna, an optical antenna can enhance the light-receiving efficiency by increasing the absorption cross-section. It is determined by the cross-section of the antenna-receiver system, equivalent to the concept of antenna aperture in electromagnetic antenna theory. The increase of the

absorption cross-section scales with the local intensity enhancement factor. For a typical molecule with a cross-section of 11 nm^2, the intensity enhancement factor can be $10^4 - 10^6$ [4]. Additionally, applying optical antennas in photodetection devices allows to shrink the detector size without any loss in absorption, which holds promise in photovoltaic applications [101]. Additionally, an optical antenna can also operate in transmitting mode. The transmission efficiency is enhanced by increasing the total amount of radiation and directing the radiation to the receiver. The antenna gain is defined as a combination of antenna efficiency ε_{rad} and directivity D:

$$G = \varepsilon_{\text{rad}} D. \tag{2.23}$$

The most important application of a transmitting antenna is to enhance the spontaneous emission rate of a quantum emitter, which will be discussed in section 2.3.

Despite many analogies between RF antennas and optical antennas, there are differences in properties and parameters. Most of these differences arise from their small size and surface plasmon resonance. For example, the penetration of radiation at the optical frequency is on the order of the optical antenna's dimension. Therefore, the penetration effect is no longer negligible so that electrons in metal responds to an effective wavelength 2-5 times smaller than the incident wavelength [105].

On the one hand, these differences impede the direct transfer of the established RF antenna's experience into optical frequencies. Obviously, the fabrication process of optical antennas is much more demanding than an RF antenna due to their nanoscale dimensions. Traditional top-down techniques, such as electron-beam lithography is commonly applied for this aim. Although it offers 10 nm accuracy, the optical properties of metal structures are often suffering from polycrystallinity of thermally evaporated metals and structural imperfection introduced from lift-off process. An alternative is to apply a focused ion-beam milling fabrication technique on a chemically synthesized single-crystalline metal flakes. It allows for preparing metallic nanostructures with improved structural homogeneity and optical quality [106], but brings an issue of reproducibility at the same time [4].

Another challenge lies in the electro-optical conversion. Unlike a conventional radio antenna, which is locally connecting to the feed element driven by electric current, an optical antenna often couples to a localized light emitter, which is excited from the far-field. This brings several challenges. First, a large impedance mismatching between the source and the antenna needs to be compensated, which is very important for directivity control. Secondly, the bandwidth and frequency of the antenna are limited by the intrinsic properties of light emitters. Moreover, as most optical antennas operate based on light-in and light-out configurations, bulky lab-scale setups are involved. Regarding electrical detection, an optical rectenna based on a tunnel junction is reported [107], and a variety of established nanoscale photodetectors are waiting for implementation. However, It is more tricky to generate light locally and electrically. Hecht *et. al.* realized electrically driven directed light emission via inelastic tunnelling [108, 109]. But the emission process is very inefficient, and it requires single-crystalline

connector wires. Electroluminescence in 2D materials that are explored intensively in recent years could be an alternative [36]. Nevertheless, connecting an ultrathin wire to a nano-object is still technically very challenging.

On the other hand, these differences open the new possibilities. First, the surface plasmonic resonance is strongly geometry dependent so that optical antennas can take various unusual forms such as tips, nanoparticles. In particular, using a sharp tip as an optical antenna, which is commonly done in near-field optical microscopy, enables to probe highly localized field with nanometer spatial resolution. For example, Hillenbrand *et al.* visualized propagating and localized graphene plasmons in real space using a scattering near-field microscopy equipped with a metallic AFM tip [110]. Secondly, metals exhibit strong nonlinear characteristics at optical frequencies, which provide possibilities in frequency mixing and conversion. Besides, the temporal response of surface plasmons in metal is on the order of femtoseconds, which holds promise for coherent ultrafast nanophotonics [111]. Finally, an optical antenna can focus light into a volume spatially comparable to an atom or a molecule's length scale. This could open up transition channels beyond the electric dipole selection rule. The photoluminescence from gold nanostructure is generally attributed to this origin [112]. Additionally, Ebbesen *et al.* used a microfluid microcavity to realize a site selectivity in a chemical reaction by modifying the chemical landscape under strong coupling [17]. Similar experiments can be expected with a plasmonic antennas.

2.3 Quantum emitter coupled to a plasmonic antenna

2.3.1 Single quantum emitters

A quantum emitter is a system that possesses discrete energy levels and supports radiative optical transitions. It can be an atom, a fluorophore molecule, a quantum dot, or a quantum-confined system such as a nitrogen-vacancy center in nanodiamond. The interaction between light and a quantum emitter falls within the theoretical frame of the two-level atom approximation. As discussed in section 2.1, the optical properties of quantum emitters are very sensitive to the local electromagnetic environment and thus can act as a local sensor [5, 6]. Furthermore, as a two-level quantum system emits only one photon at a time, a single quantum emitter can serve as a single-photon source for the application in quantum optics [7–9].

Organic fluorophore molecules are one of the most commonly used single quantum emitters. Their interaction with light is illustrated in Figure 2.6. By absorbing photons, the molecule is promoted to an excited state from a ground singlet state S_0, followed by a fast relaxation to the first excited singlet state S_1. From here, it is possible to decay radiatively or nonradiatively into different vibrational modes of the electronic ground state. The radiative relaxation, so-called fluorescence, is red-shifted from the excitation. This enables experimental detection of fluorescence as it can be spectrally separated from

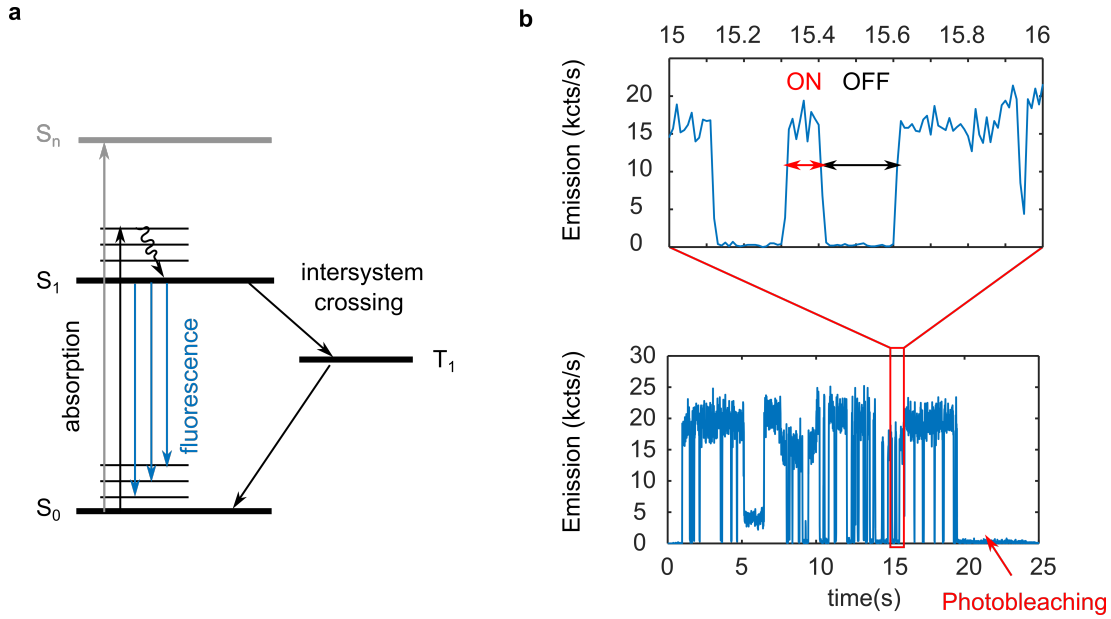

Figure 2.6: (**a**) Energy-level diagram for an organic fluorophore molecule. S_0, S_1, and T_1 stands for the ground singlet state, the first excited singlet state, and the lowest triplet state, respectively. Each electronic state contains several vibrational states. Possible transitions between different vibronic states are illustrated with lines. (**b**) Fluorescence time trace of an Atto 647N molecule in PBS buffer solution.

the excitation source. The photon emission efficiency of a fluorophore molecule is determined by quantum yield q_0

$$q_0 = \frac{\gamma_r^0}{\gamma_r^0 + \gamma_{nr}^0}, \tag{2.24}$$

where γ_r^0 is the radiative decay rate and γ_{nr}^0 is the non-radiative decay rate. An efficient fluorophore molecule possesses a low density of vibrational states of the electronic ground state at the energy of S_1, which reduces the possibility of non-radiative relaxation.

On the other hand, the molecule at S_1 can also make a transition to the lowest triplet state T_1 through intersystem crossing. This causes an interruption of the S_1- S_0 transition so that the fluorescence ceases abruptly for a period in the order of milliseconds, corresponding to the lifetime of T_1[4]. Under continuous excitation, the fluorescence of the molecule can exhibit a random switching between a bright state (ON) and a dark (OFF) state, so-called fluorescence blinking. The observation of fluorescence blinking between two intensity levels is considered a strong indication for a single emitter [114–116]. In addition, as the relaxation from T_1 to S_0 is a spin-forbidden transition, T_1 has a long

[4] A longer period dark state can be caused by photo-induced charge separations and subsequent trapping of electrons or holes [113].

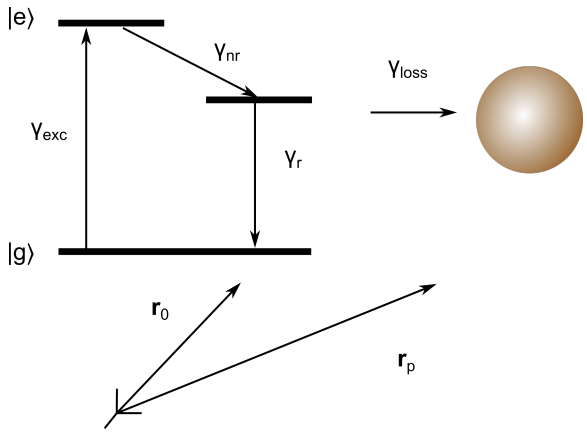

Figure 2.7: Schematic illustration of three-level quantum systems coupled to a particle antenna. $\mathbf{r}_0$ and $\mathbf{r}_p$ are the position vectors of the emitter and antenna, respectively.

lifetime. Accordingly, the triplet state is photochemically active and associated with photobleaching, a complete quench of fluorescence due to the molecule's permanent chemical alteration. Reducing the triplet state lifetime and removing the surrounding active oxidant can improve the photostability of the fluorophore molecule significantly [117, 118]. Finally, a single stepwise intensity drop caused by photobleaching is often used as a criterion to identify a single fluorophore molecule in practice [116, 119, 120].

Fluorescence blinking is observed in many different classes of quantum emitters. For example, the dark state of a semiconductor quantum dot is attributed to the charge and discharge effect of surface electron traps [113]. A local crystal disorder such as surface dangling bonds causes the blinking of an NV center in nanodiamond [121]. However, the one-step photobleaching approach can not be applied to all quantum emitters as not all of them undergo photobleaching very easily. Some other features also imply the existence of a single emitter, including spectral diffusion [122, 123], narrow spectral linewidth, and power-law dependent on- and off- time distribution [124]. The only direct proof of a single quantum emitter is the observation of photon antibunching, which is based on the fact that it can only emit one photon per excitation circle. In the correlation measurement using the Hanbury Brown-Twiss setup, photon antibunching is observed as the absence of coincidence events at zero time delay [125].

2.3.2 Enhancement and quenching of a single-emitter fluorescence

Let us consider a fluorescence process of an antenna-emitter system as shown in Figure 2.7. An external pump source with a photon energy of $\hbar\omega_{\text{exc}}$ excites the emitter from ground state to excited state with an intensity below saturation. The excitation rate ω_{exc} is determined by the transition dipole moment $\mathbf{p}$ and the local electric field which is obtained as the sum of the incident field at the location

of emitter $\mathbf{E}(\mathbf{r}_0, \omega_{\text{exc}})$ and the secondary field $\mathbf{E}_s(\mathbf{r}_0, \omega_{exc})$ at the location of emitter, which originates from the scattering from the antenna. With respect to the excitation rate of an isolated emitter γ^0_{exc}, the excitation rate becomes

$$\gamma_{\text{exc}} = \gamma^0_{\text{exc}} \frac{|\mathbf{p} \cdot [\mathbf{E}(\mathbf{r}_0, \omega_{\text{exc}}) + \mathbf{E}_s(\mathbf{r}_0, \omega_{\text{exc}})]|^2}{|\mathbf{p} \cdot [\mathbf{E}(\mathbf{r}_0, \omega_{\text{exc}})|^2}. \tag{2.25}$$

After excitation, the emitter relaxes to the ground state by radiative decay or by non-radiative decay that is associated with energy transfer to the coupled plasmon of the antenna or to the local environment. As the energy transfer occurs over a very short distance, the curvature of the antenna boundary is negligible. Therefore the non-radiative energy transfer rate γ_{loss} can be estimated from the interaction of an quantum emitter with its mirror image [63, 126]. The total decay rate γ_{total} as a sum of radiative decay rate γ_r and non-radiative decay rate γ_{loss} can be derived from Equation (2.3) as

$$\gamma_{\text{total}} = \gamma_r + \gamma_{\text{loss}} = \gamma^0_r \frac{2\pi c^3}{\omega^2} \rho(\mathbf{r}_0, \omega_r), \tag{2.26}$$

where γ^0_r is the radiative decay rate of an isolated emitter, $\rho_p(\mathbf{r}_0, \omega)$ is the local density of states and can be calculated with dyadic Green's function as [63]

$$\rho_p(\mathbf{r}_0, \omega_r) = \frac{6\omega_0}{\pi c^2} [\mathbf{n}_p \cdot \text{Im}\{\overleftrightarrow{G}(\mathbf{r}_0, \mathbf{r}_0; \omega_r)\} \cdot \mathbf{n}_p], \tag{2.27}$$

with $\mathbf{n}_p$ being the unit vector in direction of the molecule's dipole moment. Equ. (2.27) shows that both radiative and non-radiative process are influenced by the local environment, and hence can be mediated by changing the relative distance of emitter and antenna.

In the simplest case that a spherical gold nanoparticle serves as an optical antenna and the quantum emitter as a point dipole is placed next to it, the gold particle can be represented as a polarizability $\overleftrightarrow{\alpha}$. The radiative rate has the same form as excitation rate, which is attributed to reciprocity theorem [127], and can be expressed as

$$\gamma_r = \gamma^0_r \left| 1 + 2 \frac{a^3}{(a+z)^3} \frac{\varepsilon(\omega) - 1}{\varepsilon(\omega) + 2} \right|^2. \tag{2.28}$$

with z being the separation between the molecule and the antenna surface. The non-radiative rate γ_{loss} is expressed as

$$\gamma_{\text{loss}} = \gamma^0_r \text{Im}\left\{ \frac{\varepsilon - 1}{\varepsilon + 1} \right\} \frac{1}{(k_r z)^3} \frac{(p_x^2 + p_y^2 + 2p_z^2)}{|\mathbf{p}|^2}, \tag{2.29}$$

where k_r is the wave vector at the emission frequency and $\mathbf{p} = (p_x, p_y, p_z)$ [126]. We can now express the quantum yield of the antenna-emitter system by

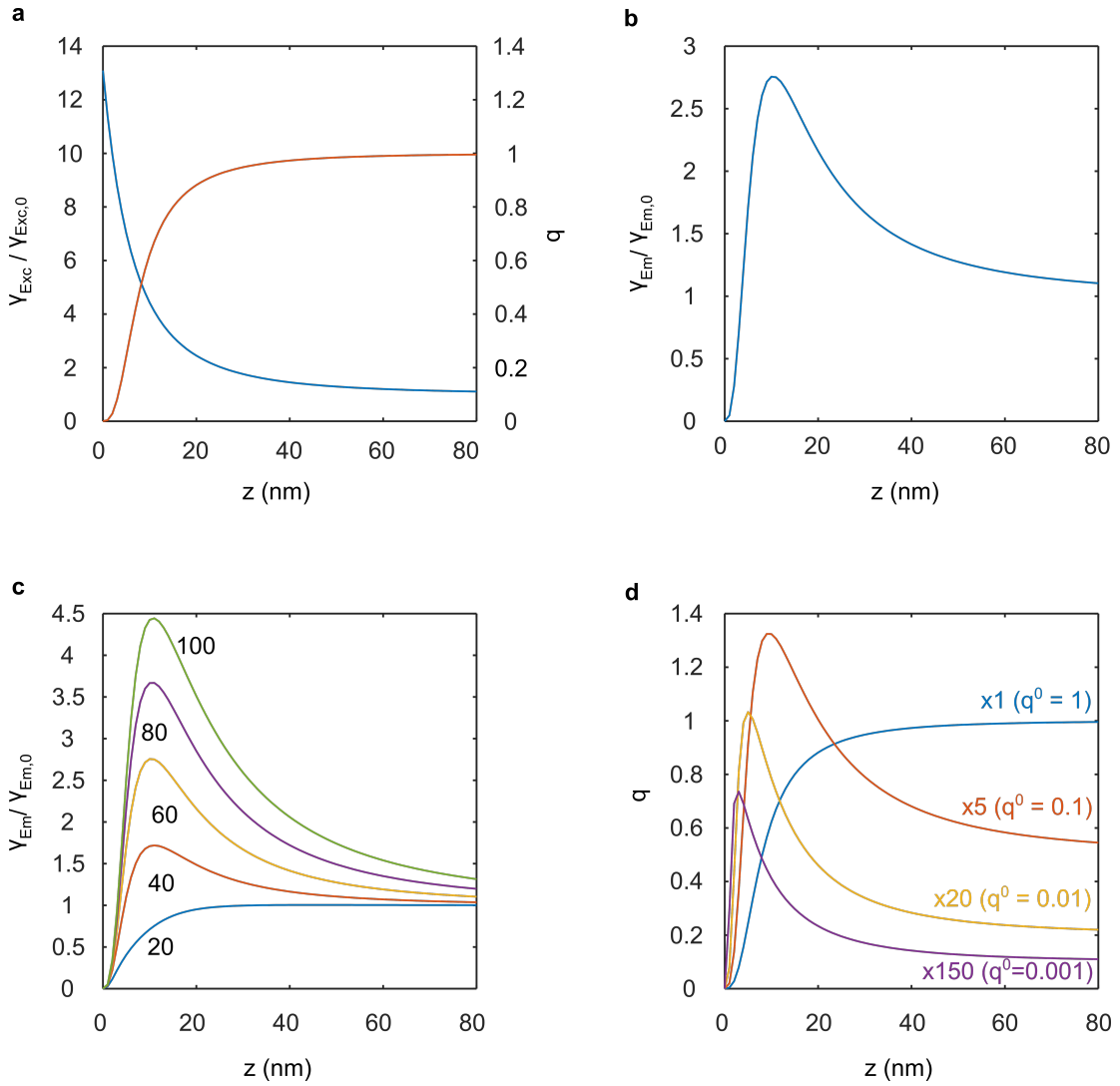

Figure 2.8: Calculated fluorescence enhancement of an emitter close to a gold nanosphere according to Eqs. (2.28) to (2.30). The system is evaluated at the excitation wavelength of λ_{exc} = 630 nm and emission at λ_{em} = 680 nm. The emitter is assumed to have a fixed orientation along $z - axis$. (**a**) Normalized excitation rate γ_{exc} (blue) and quantum yield q (red) as a function of particle-emitter separation z. Here the gold particle has a diameter of 60 nm and the emitter has an intrinsic quantum yield of $q^0 = 1$. (**b**) Normalized emission rate γ_{em} as a function of distance z for the same case as in (**a**). (**c**) Normalized emission rate γ_{em} as a function of separation z for different particle diameter: 100 nm, 80 nm, 60 nm, 40 nm and 20 nm, from top to down. Here $q^0 = 1$. (**d**) Quantum yield as a function of separation between a 60 nm gold particle and an emitter with different intrinsic quantum yield. The curves are scaled differently for better presentation.

$$q = \frac{\gamma_r/\gamma_r^0}{\gamma_r/\gamma_r^0 + \gamma_{\text{loss}}/\gamma_r^0 + (1-q^0)/q^0}. \tag{2.30}$$

Here, q^0 is the intrinsic quantum yield of the emitter and $(1-q^0)/q^0$ accounts for the intrinsic nonradiative decay inside the emitter, which is assumed not influenced by the antenna. The emission rate can be obtained as a product of excitation rate and quantum yield as the excitation and emission are incoherent processes: $\gamma_{\text{em}} = \gamma_{\text{exc}} \cdot q$.

We plot the excitation enhancement, quantum yield, and emission enhancement as a function of particle-emitter separation for different different particle size and emitters with different q^0 according to Eqs. (2.28) to (2.30) in Figure 2.8. The emitter is assumed to have a fixed dipole orientation pointing towards the particle. It shows that for an emitter with very high intrinsic quantum yield with almost no intrinsic loss, coupling to an antenna can only decrease the quantum yield. The emission enhancement is thus only a result of the acceleration of the excitation rate. This is different from the case of an emitter with very low q_0, in which the local environment can increase the photoemission drastically. For instance, the fluorescence of a single $Y_3N@C_{80}$ with $q_0 = 0.02$ is enhanced two orders of magnitude by a gold particle [11]. Furthermore, the emitter and particle's relative position is critical for emission enhancement: for large separation, the interaction between the emitter and particle becomes weak; for small separation, the dissipation process dominates, resulting in a fluorescence quenching. Additionally, from (2.29) and (2.28), we can observe a maximum of non-radiative decay process at $\varepsilon = -1$, which is blue-shifted from the plasmon resonance at $\varepsilon = -2$. Hence, the maximum of the fluorescence enhancement occurs at a longer wavelength than the plasmon resonance of the particle.

In summary, to optimize the emission enhancement of an antenna-emitter system, the ratio of radiative efficiency and non-radiative efficiency γ_r/γ_{nr} needs to be maximized. This can be achieved by tuning the antenna's materials and geometry, optimizing the emitter's dipole orientation, placing the emitter at emission favorable position with nanometer precision, and tuning the antenna resonance to the blue of the emission wavelength of the emitter. It is possible to obtain a larger enhancement through a more efficient antenna design. For example, a single molecule's fluorescence is observed to experience an enhancement up to 1340 with a bow-tie antenna [10]. Besides, the quenching effect resulting from the non-radiative process can be further suppressed by placing the emitter into an ultrasmall gap between a particle antenna and a metal substrate. In this hybrid-plasmonic system, higher-order modes which account for the dissipation in an isolated nanoparticle now radiate efficiently [128–130].

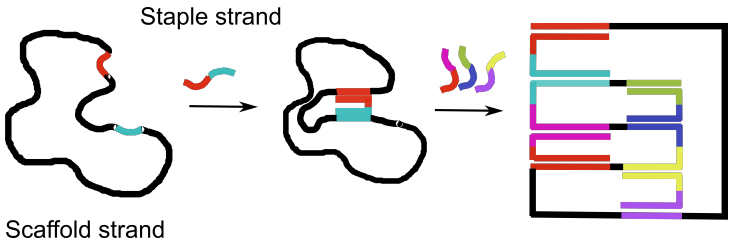

Figure 2.9: An illustration graphic of DNA origami

2.4 DNA origami for plasmon-exciton coupling

For the efficient coupling of a quantum emitter to an optical antenna, it is crucial to have their relative position controlled with nanometer accuracy (see Figure 2.8). Most works so far rely on randomly depositing emitters onto an array of antennas[5] [14, 19], or reversely, spreading chemically synthesized antennas on the pre-patterned emitters [18, 131]. The following post-selection applies to identify the emitter-antenna pairs. A method such as a two-step electron beam lithography combined with chemical functionalization [20, 21], manipulation of nano-emitter with a fiber tip [15], offers a tedious but better relative distance control.

Molecular self-assembly, DNA origami nanotechnology in particular, is an alternative solution to this challenge. It intrinsically gives nanometer accuracy since one base pair is 3.4 Å in length along the strand. Moreover, it also allows for creation of programmable three-dimensional DNA architectures with almost arbitrary shapes and full addressability [22, 23]. In addition, a DNA origami structure can also serve as a template for positioning a variety of nanoscale objects including metal nanoparticles [59, 132–135], fluorophores [16, 57, 58, 133, 136], quantum dots [133, 137, 138], carbon nanotubes [139], proteins [140, 141], etc. It has been proven that DNA origami assembled complex plasmonic system can enable enhanced radiative rate of emission [16, 57, 58], increased Fröster resonance energy transfer [62], and single molecule surface-enhanced Raman scattering [59–61]. Finally, incorporation of DNA molecular machine, DNA origami techniques facilitate the fabrication of reconfigurable nanostructures. In this section, we will provide an overview of basics of DNA origami nanotechnology and its application in light-matter interaction nanosystems.

2.4.1 DNA origami

The specificity and simplicity of Watson-Crick base pair interaction makes DNA a powerful construction material to build complex nanostructures from a large set of nucleotides. This stimulates the expansion and enrichment of the DNA nanotechnology field in the last decades. However, the synthesis of complex structures often involves large sets of DNA strands, multiple reaction and purification steps,

[5] The deposition of emitters usually refers to a low concentration of organic molecules embedded in a polymer thin film or a monolayer of atomically grown nano-structures with micrometer separation [104].

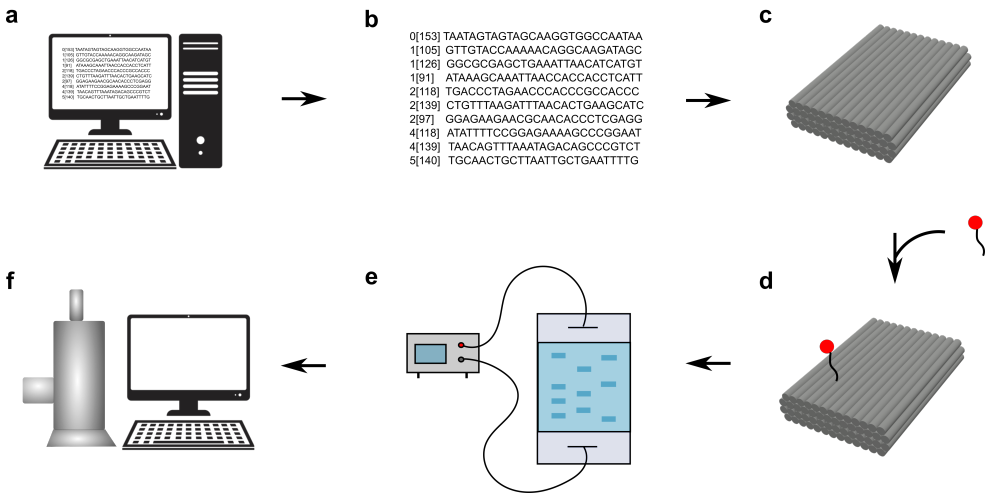

Figure 2.10: A typical DNA-origami assembled nanostructure fabrication process: (**a**) DNA origami structure design with caDNAno software; (**b**) synthesis of staple DNA strands; (**c**) assembly of DNA-origami structures by thermal annealing the mixture of a scaffold strand and excess amount of staple strands; (**d**) attachment of DNA functionalized nanoparticles to DNA origami nanostructure; (**e**) purification process using gel electrophoresis; (**f**) final characterization, e.g., transmission electron microscopy (TEM). Adapted from Ref. [142].

resulting in high expense and low yield. Most critically, most structures contain just a few unique positions which can be addressed as pixels due to the complexity of engineering diverse interactions [23]. This impedes positioning several discrete particles of predefined positions, which is very important for plasmonics application.

The DNA origami technique, first introduced by Paul Rothemund in 2006, offers a simple approach, with relatively low cost and high yield, to construct complex two- or three-dimensional DNA nanostructures capable of carrying diverse components with nanometer precision. The idea is to use a long single-stranded viral DNA molecule as a scaffold strand and fold it into the desired structure with the help of a set of short DNA oligonucleotides, as illustrated in Figure. 2.9. The scaffold DNA strand is usually from a known sequence with thousand base pairs, such as a sequence of genomic DNA from M13 bacteriophage. Each short oligonucleotide will bind the specific position of the scaffold, eventually forming a three-dimensional nanostructure. Attaching nano-objects to origami nanostructures is realized by single-stranded DNA extension as capture strands and chemical modifications such as biotin or amino groups. The assembly of nanoparticles, such as metal spheres, requires functionalization with complementary strands of the capture strands. This is different from a fluorophore, which is often incorporated into staple strands directly. Additionally, with chemical modification, it is possible to attach a protein molecule or even immobilize an origami structure on a substrate through biotin-streptavidin interaction.

A standard workflow of a DNA assembled nanostructure is as follows (see Figure 2.10): first,

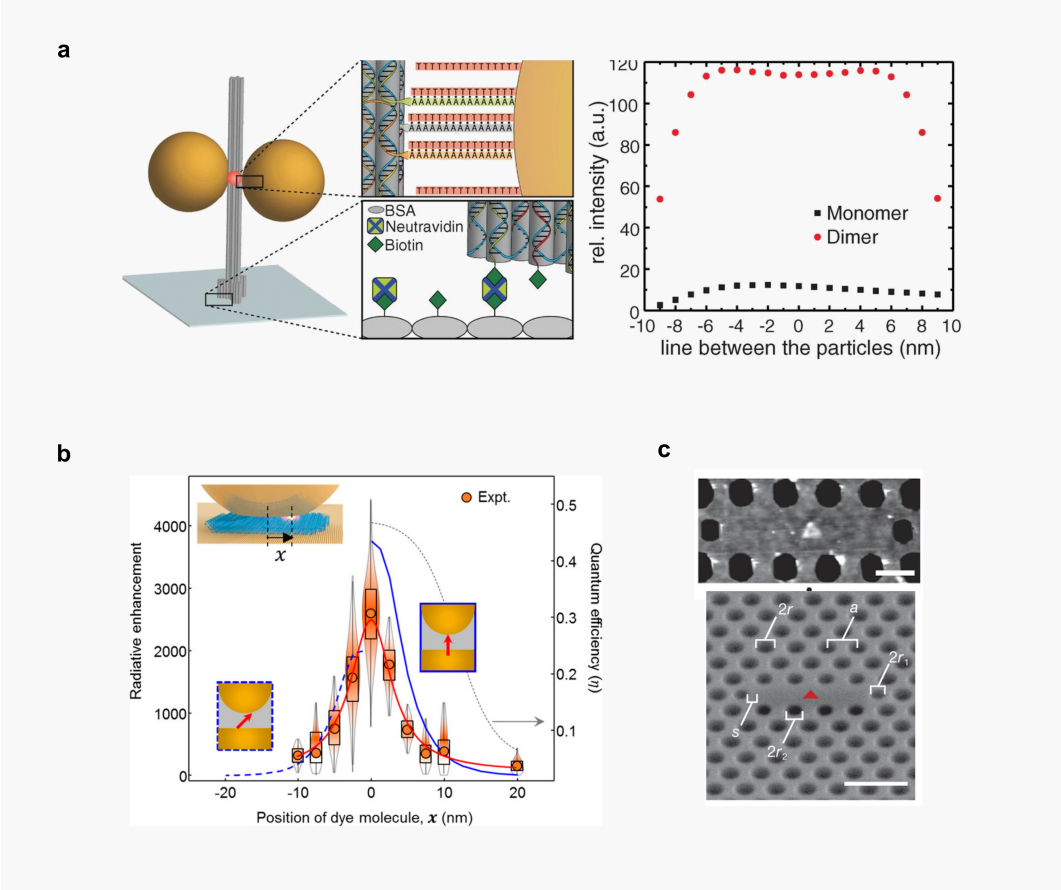

Figure 2.11: (**a**) optical gap antenna assembled by DNA origami technique for fluorescence enhancement [58]; (**b**) mapping the LDOS in plasmonic nanocavity when laterally displacing the position of single molecule on an origami template [19]; (**c**), combination of DNA origami assembled triangles with lithographic photonic crystal cavities [136]. Scale bars: 250 nm (top), and 500 nm (bottom).

conceiving the geometry of an origami structure and arrangement of nano-objects; next, using design software called caDNAno [22, 143] to generate sequences for all short and extension strands, and sending the sequences to commercial vendors for synthesis; assembly of the origami nanostructure with desired functionalities, followed by a gel electrophoresis purification process; last, structure inspection with transmission scanning spectroscopy or atomic force microscopy. After that, we can perform further investigations, such as optical microscopy [16, 57–62] or molecular force studies [144], on ensemble-level or individual origami structure.

2.4.2 Plasmon-excition hybrid nanosystem

DNA origami techniques have made significant progress in the fabrication of chiral plasmonic structures [1, 24, 134, 135], and plasmonic coupling systems containing multiple particles [145], due

to the possibility to arrange gold particles precisely on the origami template. However, the exploration of application in plasmon-exciton interaction is rather primitively that only a few configurations have been demonstrated. Earlier studies mostly focus on the distance-dependent energy transfer between a single fluorophore and a single small gold particle, as it is easy to position a small gold particle within 20 nm on origami bundles and control the relative distance precisely [146].

Acuna *et al.* put forward a DNA-origami assembled nanostructure for fluorescence enhancement of a dye molecule in 2012 (see Figure 2.11**a**). In this structure, two gold nanoparticles with a gap of 23 nm form a gap antenna, are attached to a DNA origami pillar, where a dye molecule within the pillar that is located at the center of the gap. The maximum observed enhancement is up to 117-fold [58]. Later, large varieties based on this configuration have been reported, including breaking the high concentration limit of single-molecule detection in life sciences [57, 147], fluorescence enhancement of a quantum dot [148] or a protein complex [149], detection of Zika virus nucleic acids [150] and a portable smartphone microscope [151]. On the one hand, this geometry demonstrates robust in emission enhancement, which is different from the case of a bowtie antenna. There is no evidence for a fluorescent enhancement in a DNA origami-assembled bowtie antenna nanosystem, even though many previous studies with traditional top-down fabrication techniques have proven it [60]. On the other hand, several critical limitations remain. First of all, there is a large spread in the enhancement factor, resulting from the imperfections of assembly, particle morphology, and antenna efficiency limited by particle size. A Large particle will exhibit stronger enhancement, but increase the chance of detachment from the origami pillar at the same time. Secondly, it requires a considerable effort to engineer the photostability of the fluorophore [117]. Therefore, emitters in this prototype have only a limited number of choices, restricting the system's enhancement efficiency.

A more complex hybrid plasmon-exciton nanosystem can be realized through a combination of DNA-origami assembled techniques and traditional top-down techniques. Here, the plasmonic structure is fabricated by electron beam lithography or ion-beam milling, while DNA-origami assembled structure serves as a sizing unit. This approach allows to circumvent the difficulties of attaching large metal particles or antenna with complex geometry. One simple example is to place a DNA origami template with a single molecule in a sub-5 nm plasmonic nanocavity. Changing the lateral position of the molecule precisely on origami template enables the direct map of the spatial profile of the LDOS (see Figure 2.11) [19]. Another attempt is to place the origami nanostructure onto lithographically patterned binding sites. Gopinath *et al.* demonstrated a reliable and controlled coupling of molecular emitters to photonic crystal cavities with this approach (see Figure 2.11**c**) [136]. We can foresee a similar method applied for plasmon-exciton coupling.

Most importantly, DNA origami techniques do not only support static devices. Incorporation of dynamic DNA nanotechnology into DNA origami-based plasmonic structures affords extra functionalities. For instance, the reconfigurable origami template allows the rearrangement of plasmonic nanoparticles under external stimuli such as specific DNA strands [24], pH [26], light [25],

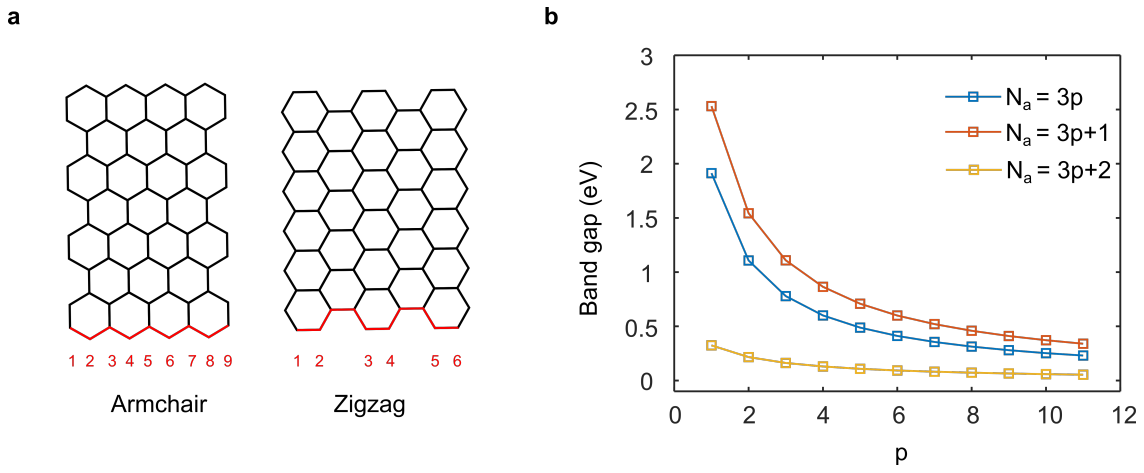

Figure 2.12: (**a**) Structure of seven-atom wide armchair-edge graphene nanoribbons (7-AGNRs) and six atom-wide zigzag-edge graphene nanoribbons (6-ZGNR). The edges in GNRs are passivated by hydrogen atoms. (**b**) Calculated band gap as a function of p for armchair graphene nanoribbons with edge carbon atoms: $N_a = 3p, 3p + 1, 3p + 2$; p is an integer. The value is calculated from equation in [152].

which give rise to a change of optical response. In addition, a metal particle and emitter can serve as a molecular walker moving on a static origami template through specific DNA reactions such as toehold-mediated strand displacement reaction [1]. Particularly, it is possible to trigger an autonomous sequence of change with the help of a DNA-RNA reaction [16]. This allows a rigorous study of the distance dependence of plasmon-exciton interactions, which is often achieved by the fabrication of multiple samples [19].

2.5 Nanostructured graphene

Exploring novel excitonic materials for plasmon-exciton interaction is an increasingly important area. In particular, two-dimensional (2D) materials such as graphene-based materials, transition metal dichalcogenides (TMD) have attracted tremendous interest due to their exceptional optical properties. For example, localized excitons and atomic defects in 2D materials can exhibit bright single-photon emission at room temperature, in which the emission wavelength is tunable through strain control [27], dimensional engineering [28, 29], magnetic field [153], and variation of doping concentration [154]. Therefore, 2D materials supported single emitters can be a more photostable and versatile alternative to the traditional fluorophore in quantum optics applications. Additionally, the electronic band structure of 2D materials such as TMD has a unique valley configuration, where the excitons in the same valley but opposite spin can be addressed selectively with different polarization of incident light [30–32]. This brings new modes in plasmon-exciton interaction when coupling to metal nanostructures. Most

importantly, new optical effects stem from the coupling effect between plasmons and excitons in 2D materials, including brightening dark-excitons [155, 156], improving the exciton energy transfer range [35], and supporting new hybrid states, namely exciton polariton, when entering into the strong coupling regime [157, 158]. It also allows to probe inherent weak features such as emissions with low quantum yield [2]. In this dissertation, we will focus on the plasmonically enhanced optical properties of graphene nanoribbons.

One dimensional graphene nanoribbons (GNRs) have emerged as a promising material for future optoelectronic applications due to their tunable electronic and optical properties [41–48]. The width and edge geometry strongly influence the properties of GNRs [49–52]. Based on the edge geometry, they are classified into two categories: armchair-shaped edge GNRs (AGNRs) and zigzag-shaped edge GNRs (ZGNRs), as shown in Figure 2.12**a**. AGNRs show semiconducting characteristics with a direct bandgap. The bandgap energy of an AGNR is inversely proportional to its width as the bandgap arises from the quantum confinement effect. Moreover, the variation of the bandgap energy exhibits a unique family behavior related to the number of dimer lines across the ribbon width N, that is, $E_{gap}^{N=3p+1} > E_{gap}^{N=3p} > E_{gap}^{N=3p+2}$, with p being a positive integer (see Figure 2.12**b**) [42]. Accordingly, $(3p+1)$-AGNR is very important for optical applications as its bandgap corresponds to the visible wavelength for small p. In contrast, although ZGNRs also have direct bandgaps, which shows a ribbon width dependence, there is no similar family effect. Instead, it has peculiar edge states allowing to couple ferromagnetically along the edge and antiferromagnetic between the edges, crucial for graphene-based spintronics [39, 41, 159]. Hence, it is possible to synthesize semiconducting nanoribbons with control of the bandgap energy [38, 53, 54], and even topological engineered bandstructure [55, 56] by tuning the width and edge of GNRs.

Importantly, using bottom-up wet-chemical fabrication techniques, atomically precise GNRs are feasible. In this context, GNRs can be seen as conjugated macromolecules with thousands of atoms, which are synthesized through surface-assisted polymerization of pre-designed precursor molecules, followed by a thermally activated cyclodehydrogenation reaction. As the precursor molecule determines the edge and width of GNRs, tuning the structures of GNRs can be realized by properly choosing the precursor molecule [37–40]. Furthermore, the bottom-up synthesis route allows substitutional doping with atomically precise control by employing a doped precursor, [160, 161]. It is also possible to form GNR heterojunctions by annealing a mixture of different precursors molecules or fusing different GNR segments [38, 162].

So far, seven-atom wide semiconducting armchair-edge graphene nanoribbons (7-AGNRs) are the most intensively studied GNRs. Previous optical studies on the ensemble level of 7-AGNRs such as Raman [34, 38, 165, 166], photoluminescence [33, 34], optical reflectance anisotropy [167], and absorption [168, 169] spectroscopy have revealed the excitonic nature of optical transitions. For wider lithographically prepared GNRs, edge plasmon oscillations have been observed using scanning probe techniques [170]. A major finding of these studies is that the photoluminescence of pristine

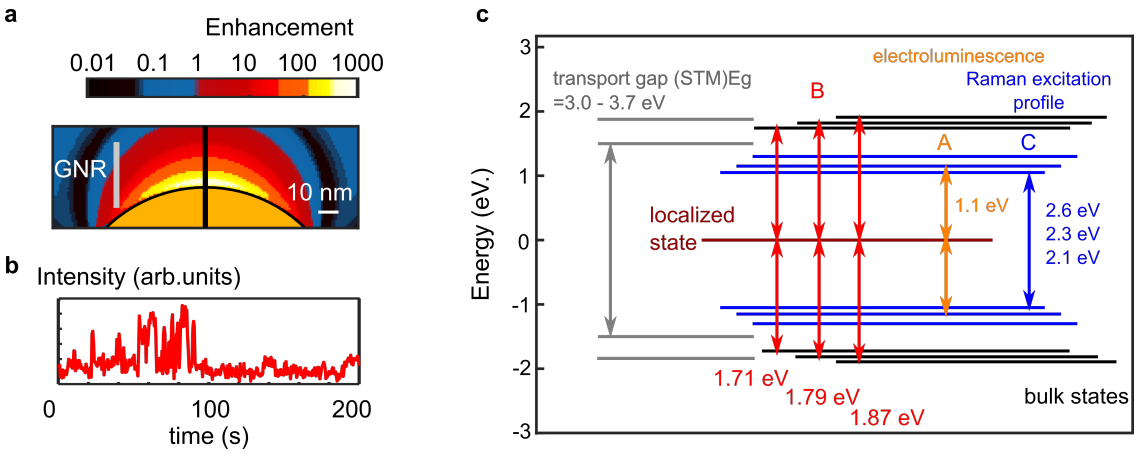

Figure 2.13: (**a**), zoom-in on a plasmonic hotspot. The lateral dimensions of one 7-AGNR are indicated with the white line. The enhancement is shown above the pseudocolor plot. (**b**), timetraces for the emission from a selected nanoantenna. (**c**) Proposed energy scheme for 7-AGNRs with three optical transitions: (A) transitions between localized states (Tamm states) and delocalized bulk states at the band edge; (B) transitions between Tamm states and deeper bulk states; (C) transitions between only bulk states. The transition energies for transitions A are taken from Ref. [163] assuming 30 nm long GNRs. Energies in B are taken from [2]. Energies for transitions C originate from Raman excitation profile measurements [33] and the value for the band gap is taken from scanning tunnelling spectroscopy studies [76, 164]. Adapted from Ref. [2]

7-AGNRs is very low. This is attributed to the presence of low-energy dark excitons, a common feature of $(3p + 1)$-GNRs. These dark excitons are energetically close to optical emissive states, providing a competing path for non-radiative decay of optical excitations [46, 50]. This has been further proved by extinction spectral changing during defect-induced brightening of 7-AGNRs. Here, 7-AGNRs experience a photoluminescence enhancement during defect formation, accompanied by the observation that a low-energy peak vanishes while high-energy peaks remain unmodified in the absorption [33, 168].

Apart from inducing defects to remove the dark excitons, the photoluminescence of AGNRs can also be significantly enhanced by coupling to a plasmonic nanoantenna [34]. The highly confined plasmonic hotspots allow the observation of emission from down to the single AGNR (see Figure 2.13). Surprisingly, the emission of AGNRs exhibits fluorescence bursts with narrow-band line widths and shows spectral diffusion, which are typical signatures of single quantum emitters. The current interpretation suggests that Tamm states, which are spatially located at the terminus of GNRs and energetically situated in the center of the bandgap, are crucial for observing fluorescence bursts [2]. The fluorescence bursts are attributed to the optical transition between Tamm states and bulk states delocalized along the whole GNRs, consistent with the electroluminescence findings in Ref. [163]. The nature of bright and dark states and emission processes still require further study.

CHAPTER 3

Experimental method

This chapter describes the far-field optical microscopy techniques and data analysis methods used in this dissertation. We introduce the principle of a confocal microscopy, followed by single-molecule localization studies. Then we proceed with time-resolved single-molecule techniques, where the excited state lifetime of a molecule can be determined. We continue with the optical microscopy of metal nanoparticles including extinction microscopy and dark-field microscopy, which allows measuring the extinction of single optical antenna. We additionally briefly introduce interferometric scattering microscopy which allows to detect particles smaller than 20 nm. The scheme of the experimental setups will be given at the end.

3.1 Confocal microscopy

Confocal microscopy is a standard far-field technique to image single molecules. As shown in Figure 3.1, the basic principle is to illuminate the sample with a focused spot from a collimated laser beam. The emitted photons are collected and spatially filtered by an aperture, which is in the plane conjugated to the illumination plane, so-called a confocal pinhole. This attenuates out-of-focus photons and stray light so that only light from the initial illumination spot's optical response can be detected. The confocal microscopy thus provides a better image contrast and axial resolution compared to wide-field microscopy.

The resolution of a confocal microscope is limited by diffraction. It is defined as the minimum distances of two objects that can be resolved. The lateral resolution is given by the Airy disk radius, which depends on the numerical aperture NA of the objective and illumination wavelength λ, given as [171]

$$\Delta r_{\parallel} = 0.6098 \frac{\lambda}{\mathrm{NA}} \tag{3.1}$$

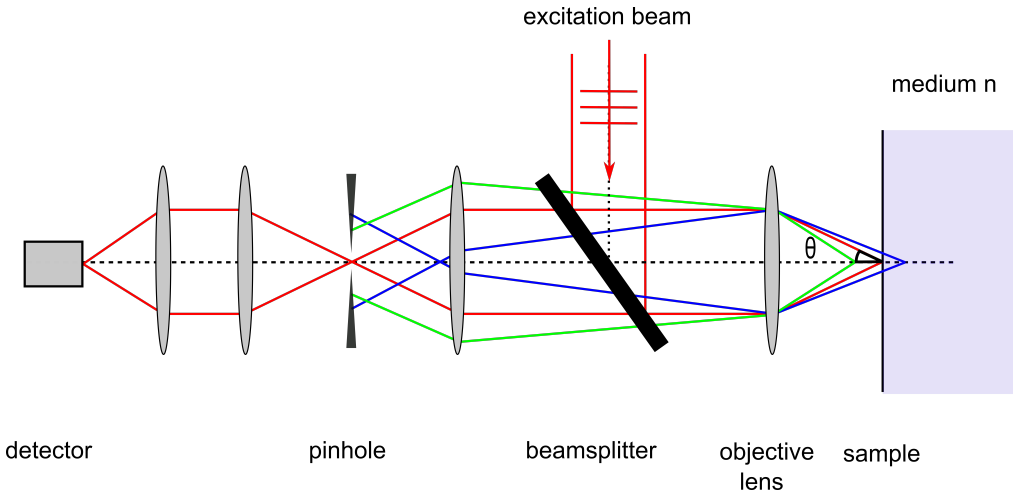

Figure 3.1: Principle of a confocal microscope: excitation beam is focused on the specimen by an objective lens to form a diffraction-limited spot. The optical response is collected with the same objective and separated from the excitation path by a beamsplitter. A pinhole at the conjugate plane of the focus spot, blocks out-of-focus light (green and blue) and only allows the light from the excitation spot (red) to reach the detector.

The numerical aperture is a product of the refractive index of the medium of the object and the sine of the maximum incident angle in which light can get through the objective, given as $\mathrm{NA} = n \sin\theta$. Accordingly, a high NA oil immersion objective is commonly used in single-molecule detection to achieve a better spatial resolution. The immersion oil has the nearly same refractive index as the microscope slide so that the reflected incident light is minimized. As a result, more light is directed through the objective. Additionally, introducing a pinhole gives rise to axial resolution as only light originating from sample plane can pass. The axial resolution is given as

$$\Delta r_{\perp} = 2\frac{n\lambda}{\mathrm{NA}^2}. \tag{3.2}$$

In our experimental setup, we use an oil immersion objective NA = 1.49 and an incident wavelength of 630 nm, which yields a lateral resolution of 278 nm and an axial resolution of 860 nm. We remark that the improvement of the lateral resolution using a confocal microscope is rather marginal. Nevertheless, introducing a pinhole is very useful for imaging a dense sample or a specimen with liquid immersion, where a lot of scattering takes place. Furthermore, combined with techniques such as stimulated depletion emission, confocal microscopy can achieve sub-diffraction-limit resolution [172].

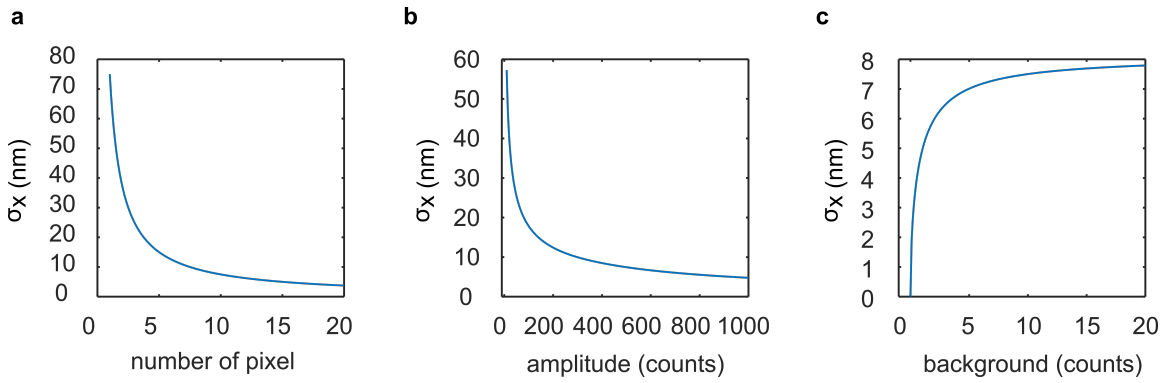

Figure 3.2: Position uncertainty σ_x as a function of pixels (a), signal amplitude (b), and background (c). Adapted from Ref. [63]

3.2 Single molecule localization microscopy

A point-like radiating source such as a single molecule produces a diffraction limited spot in the far-field optical image. This diffraction limited spot is described by a point-spread function (PSF). Reversely, the position of an emitter can be determined by fitting a PSF to the experimental data. A method called single-molecule localization microscopy (SMLM) is developed based on localizing single molecules from the PSF, which has important applications in the visualization of biological structures and tracking biological motions [173, 174]. However, the physical PSF models often involve non-trivial terms such as integrals and infinite series, leading to high complexity computations. In practice, we use the least-squares Gaussian approximation method to fit the PSF of a wide-field or confocal microscope, which results in simple and fast data processing [63, 175]. For a captured image pattern originating from an isolated emitter, the intensity $D_{i,j}$ at pixel with coordinates (i, j) is approximated by a two-dimensional (2D) Gaussian distribution:

$$G_{i,j} = B + A\exp\left[-\frac{(i-i_0)^2 + (j-j_0)^2}{2w^2}\right]. \tag{3.3}$$

There are five parameters: the coordinates of the maximum (i_0, j_0) (i.e., the emission center), the background signal B, the amplitude A, and width w. The least-squares method is then applied to find the optimal parameter sets by minimizing the sum of the squares of the residuals

$$\chi^2 = \sum_{i,j=1}^{N} [G_{i,j} - D_{i,j}]^2. \tag{3.4}$$

The fitting uncertainty depends on the number of pixels of the image pattern, the amplitude, and background noise (see Figure 3.2). In order to determine a molecule position with high accuracy,

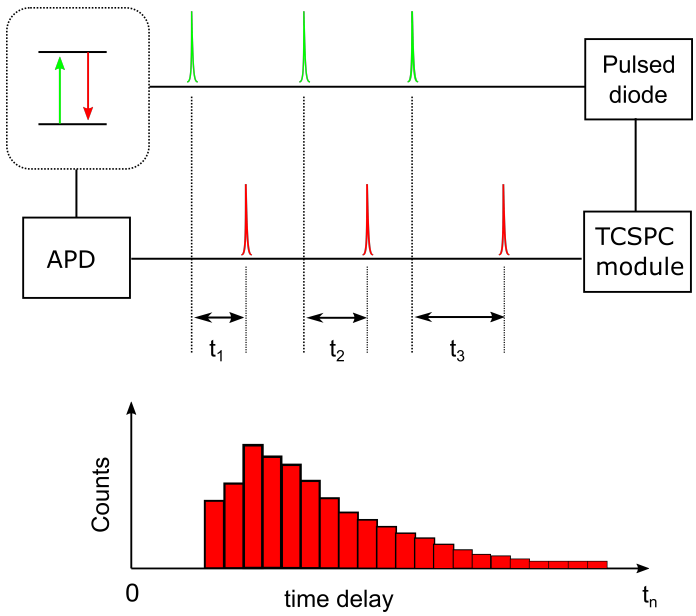

Figure 3.3: Working principle of time-correlated single-photon counting. The time delays are the difference between the emitted photon arriving time and the corresponding excitation pulse. The time delays forms a histogram, which allows to determine the emitter's excited-state lifetime.

it is important to have enough pixels for fitting, high intensity, and low background level. With the Gaussian approximation method, a position accuracy down to 10 nm can be achieved [176–179].

For a composite emission pattern from more than one emitter, it is possible to determine the individual position and the relative distance using Gaussian approximation if emitted photons from individual emitters are distinguishable through spectra, arrival time, or blinking statistics. Additionally, In the emitter-antenna coupled system, the emission pattern is the interference of the direct emission and that from the antenna. This interference results in a spatial shift of the emission spot from the actual position of the emitter. The spatial shift magnitude depends on the antenna size and the near-field coupling strength [180–183]. The shift in the observed emission localization of an emitter close to a plasmonic structure can therefore convey information about the optical near field [184–186].

3.3 Time-correlated single photon counting

3.3.1 Principle of time-correlated single-photon counting

An excited molecule can return to the ground state either radiatively or non-radiatively. The excited-state lifetime can be experimentally determined by a method called time-correlated single-photon counting (TCSPC). Figure 3.3 illustrates the working principle of this method. First, a pulsed laser sends out a short excitation pulse to excite the molecule, simultaneously sending an electric pulse to

a TCSPC module to trigger a ”start”. When an emitted photon from the molecule is detected, the single-photon detection module, such as an avalanche photo diode (APD) will send a signal to the TCSPC module as a ”stop”. The start-stop time difference, defined as time delay, is analyzed and converted into a digital timing result in the TCSPC module. Repeating this process many times builds up a distribution of time delays, which is the decay profile of the molecule.

If more than one photon is emitted in the system after one excitation cycle, the TCSPC module tends to only register the first one and ignore the following ones. This is the so-called pile-up effect, resulting in a distortion of the decay profile. In order to avoid the pile-up effect, the repetition rate of the excitation source is usually kept at least 20 times faster than the count rates at the detector in practice [187]. On the contrary, if no photon is detected after one excitation pulse, the TCSPC module will be reset by the next excitation pulse arises. When a high-frequency excitation source is applied, those no 'stop' events can be discarded to reduce the data rate without losing useful information. This is realized in Timetagger by a function called 'conditional filter'.

The instrument response function (IRF) characterizes the timing resolution of a TCSPC system. Factors such as timing accuracy of the detector, timing accuracy of the excitation source, the length of the excitation pulse, and timing jitter of the electronics can give rise to a broadening of the IRF. It can be measured by removing spectral filters, placing a cover glass in the sample holder so that there is no fluorescence but only reflected excitation light reaching the detector. Additionally, the IRF exhibits a spectral dependence. When using the deconvolution method to determine the fluorescence lifetime, it is important to measure IRF at the wavelength close to the fluorophore's emission.

3.3.2 Fitting fluorescence intensity decays

For a system with an excited state population n_0, the decay process can often be described by the differential equation

$$-\frac{dn(t)}{dt} = -[k_r + k_{nr}]n(t), \tag{3.5}$$

where $n(t)$ is the excited state population at time t, k_r, and k_{nr} are the radiative and non-radiative rate constants, respectively. Here the characteristic time-scale that a molecule spends in the excited state is defined as

$$\tau = (k_r + k_{nr})^{-1}. \tag{3.6}$$

Assuming that the fluorescence intensity is proportional to the excited state population $n(t)$, the intensity decay $I(t)$ is therefore exponential, given by

$$I(t) = I_0 \exp(-\frac{t}{\tau}), \tag{3.7}$$

with I_0 being the intensity at $t = 0$. Therefore, for a quick determination of the fluorescence lifetime, a mono-exponential tail fitting can be performed on the time-delays histogram using Equation 3.7. However, the first portion of the data in the histogram should be excluded for the fitting as the mono-exponential decay model is not valid for the initial rise when the laser pulse arrives. Additionally, if the system possesses more than one lifetime, the intensity decay can be described as the sum of the intensities from each decay

$$I(t) = \sum_j \alpha_j \exp\left(-\frac{t}{\tau_j}\right), \tag{3.8}$$

where α_j is the pre-exponential factor accounting for the fraction of lifetime τ_j.

A more accurate fitting approach is called deconvolution fitting[1] [188]. The measured intensity $N(t)$ in the histogram, is the convolution of the physical process of the fluorescence decay $I(t)$ with IRF $L(t)$, given as

$$N(t) = \int_0^t L(t')I(t-t')dt'. \tag{3.9}$$

Here $I(t-t')$ denotes the fluorescence intensity from the sample at time t, originating as a response to an excitation pulse at time t' and with amplitude $L(t')$. The goal is to determine $I(t)$, which yields the best overall fit between $N(t)$ and $L(t)$. In this dissertation, this fitting procedure is achieved using iterative reconvolution with a least-squares method with software DecayFit 1.4 [189], which finds the optimal parameter by minimizing the parameter χ_R^2

$$\chi_R^2 = \frac{1}{n}\left[\sum_{k=1}^{n} \frac{(N(t_k) - N_c(t_k))^2}{N(t_k)}\right]. \tag{3.10}$$

Here, n is the number of data points, while $N(t_k)$ and $N_c(t_k)$ are the measured counts and fitted counts at time t_k, respectively. For a good fit, χ_R^2 should approach to 1 and the residual should be randomly distributed around 0.

3.4 Optical microscopy for metal nanoparticles

The optical properties of metal nanoparticles can be experimentally determined using extinction spectroscopy (see Figure 3.4(**a**)). Here a broadband warm white light from a tungsten lamp illuminates the sample from the substrate, and then it is coupled to a 10x magnification microscope objective. The transmitted light is collected by the objective and sent to the spectrometer. The extinction spectra can be determined as the loss of the optical radiation. We remark that here we use a small NA objective (NA=0.25) so that only zero-order diffraction, i.e., direct transmission, is collected. Additionally, the spectrometer's slits in the image plane can be closed down to a small aperture, which allows measuring

[1] We remark that there is no actual deconvolution taking place, rather convoluting IRF with simulated decay instead.

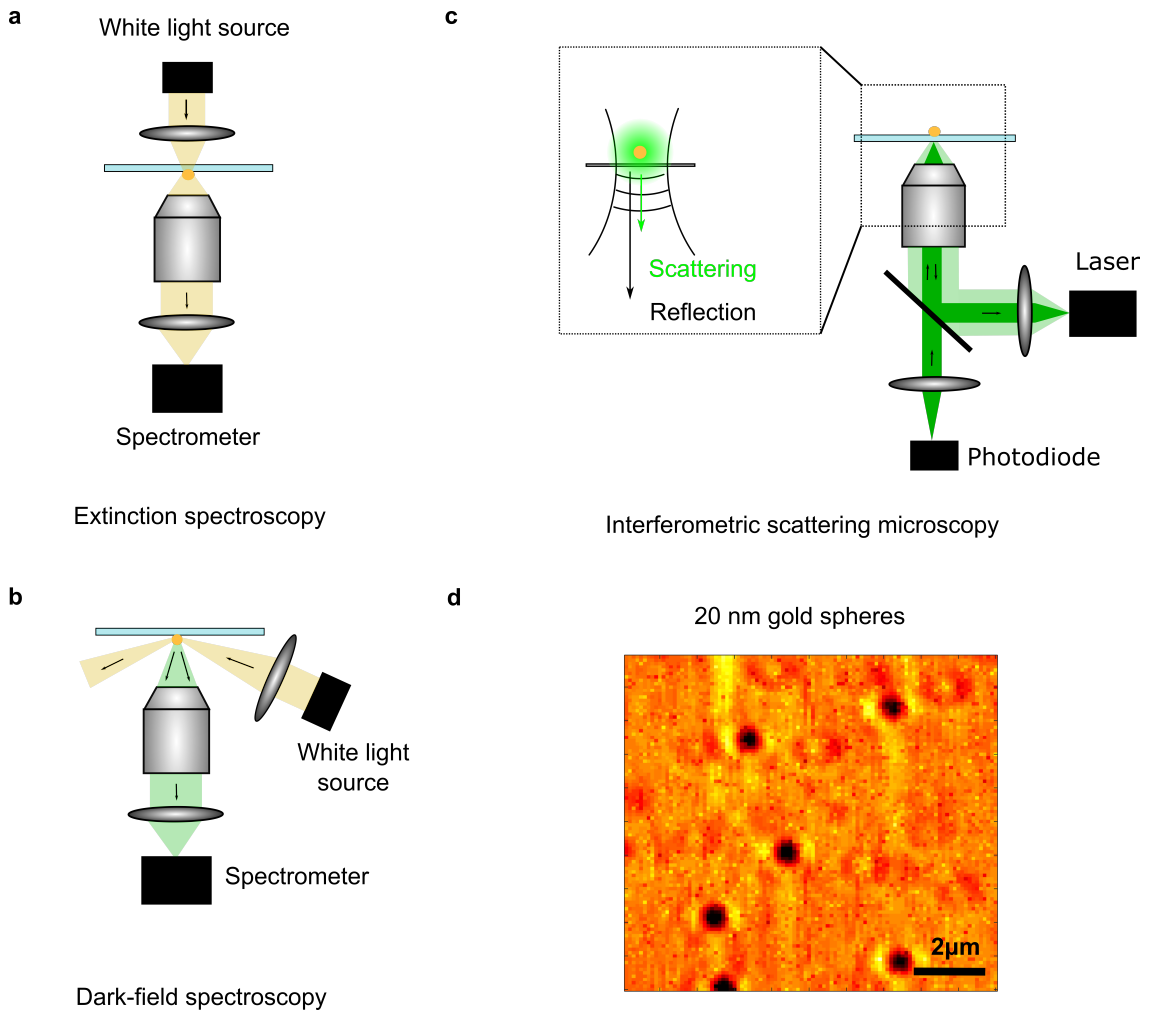

Figure 3.4: (**a**) extinction spectroscopy (**b**) dark-field spectroscopy (**c**) interforemetric scattering microscopy (iSCAT), where the inset is an illustration of the interaction between gold nanoparticle and the optical field. (**d**) An iSCAT image of 20 nm gold spheres on a coverslip.

the extinction from a single nanoparticle.

Another important method to spectrally characterize metal nanoparticles is dark-field spectroscopy, which provides a better signal-to-noise ratio compared to the transmission approach in the extinction spectroscopy. As is shown in Figure 3.4**b**, the white light source illuminates the sample in a way such that no reflected light enters into the objective. The scattered light is collected by the objective and sent to the spectrometer. Unlike extinction spectroscopy, dark-field spectroscopy allows applying a high NA objective (NA=0.8), and circumvents the artifacts arising from the illumination fluctuation in transimission arrangement.

Dark-field microscopy with high detection sensitivity is very important in single-particle based

bioimaging application [190–192]. However, it is very challenging to detect small nanoparticles with the dark-field method due to their weak scattering strength. A method called interferometric scattering microscopy (iSCAT) provides a way to overcome this challenge [193, 194] (see Figure 3.4**c**). In this method, the scattered field from a nanoparticle $\mathbf{E}_s = E_s e^{i\phi_s}$ interferes with a reference field $\mathbf{E}_r = E_r e^{i\phi_r}$, which is in our case the reflected light, yielding the measured intensity I_m as

$$I_m = |E_r + E_s|^2 = I_r + I_s + 2E_r E_s \cos\phi. \tag{3.11}$$

Here I_r and I_s are the intensity of the light reflected from substrate and scattered from the nanoparticle, respectively, and E_r and E_s are the corresponding amplitude of the electric fields. The phase ϕ in the cross-term contains the contribution of the propagation phase, a Gouy phase shift, and the contribution arising from the scattering from the nanoparticle. Here I_s drops with the sixth power of the particle size. Hence, it vanishes quickly into the background as the particle dimension decreases. On the other hand, the cross-term in Eq. 3.11 drops slower and, consequently, dominates in I_m for small nanoparticles. This enables the detection of single gold nanoparticles down to a diameter of 5 nm [193]. The intensity contrast c in the presence of a nanoparticle is defined as

$$c = \frac{I_m - I_r}{I_r} = 2\frac{E_s}{E_r}\cos\phi. \tag{3.12}$$

Equation 3.12 implies the engineering the balance between E_r and E_s is beneficial to increase the image contrast. This is done in our experiment by aligning the pinhole in the detection path. Additionally, we use a laser source with a low power flucturation and a good beam pointing stability for illumination. For detection, we use a low-noise photoreceiver with a 10Hz filter, so that the instrumental noises are strongly suppressed. Figure 3.4**d** shows an example of 20 nm gold spheres measured with our iSCAT experimental setup, where a destructive interference can be observed in the center of the gold sphere. Furthermore, the detection sensitivity is fundamentally limited by the shot-noise, given as the square root of photon number. Therefore, increasing the illumination power can enhance detection sensitivity significantly.

3.5 Experimental setups

3.5.1 Home-built laser-scanning inverted confocal microcope

In this dissertation, the experiment in Chapter 5 is carried out in a home-built laser-scanning inverted confocal microscope shown in Figure 3.5. For the excitation of the molecule, we used a pulsed diode driven by a laser controller (PILAS) that allows to be operated at the repetition rate up to 40 MHz. Light from the pulsed diode passes through polarization optics and dielectric filter, reflected at a piezo scanning-mirror (model S-334, Physik Instrumente). The reflected light is focused to a

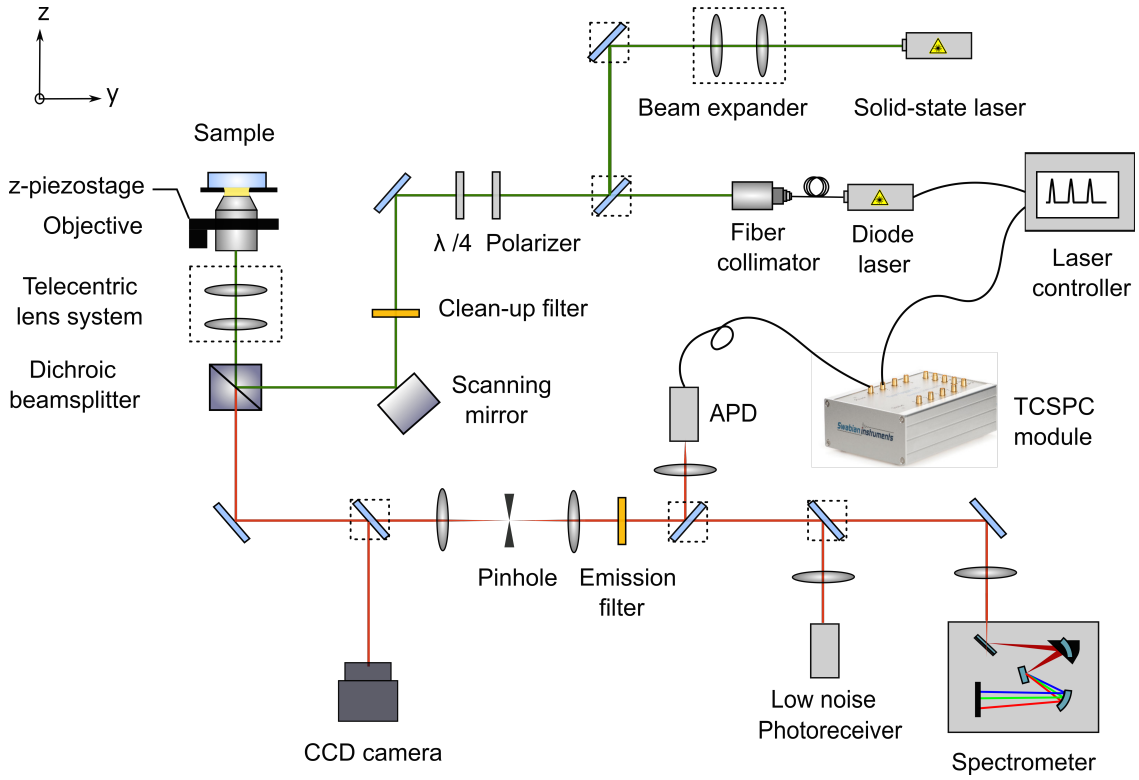

Figure 3.5: Schematic of a home-built laser scanning inverted confocal microscope.

diffraction-limited spot on the sample using an oil immersion objective (NA=1.49, Olympus). The objective is mounted with a piezo focusing unit (Physik Instrumente), which allows adjusting the focus by a stepwise of 100 nm. A telecentric system that consists of two 100 mm achromatic lenses, is installed before the objective.

The emitted fluorescence photons are collected with the same objective, separated from the excitation light using dielectric filters, and directed to a fast single-photon counting APD (PDM, Micro Photon Devices) or a spectrometer (IsoPlane SCT320 spectrograph, Teledyne Princeton Instruments) equipped with a CCD camera (PIXIS 400, Teledyne Princeton Instruments). A confocal pinhole with a diameter of 25 microns is placed in the detection path to block out-of-focus light. The fluorescence decay traces are recorded using time-correlated single-photon counting by connecting the timing output of the APD and the laser to a TCPSC module (Timetagger20, Swabian Instruments). For Atto 647N detection, we use a filter set (635 nm LED HC Filter Set, AHF analysentechnik), which consists of a clean up filter (635/18 BrightLine HC), a dichroic beamsplitter (Beamsplitter HC BS 652) and an emission filter (680/42 BrightLine HC).

The iSCAT experiment is performed based on the same microscope. All the dielectric filters are removed and the dichroic mirror is replaced by a non-polarizing 50/50 beamsplitter. The sample is

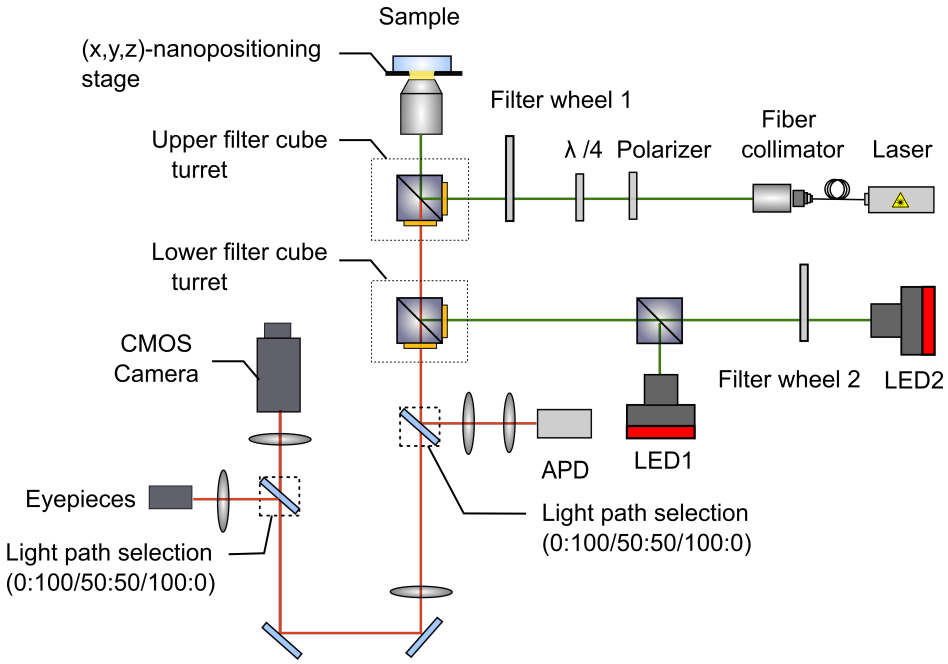

Figure 3.6: Schematic of a custom-built fluorescence microscope based on Olympus IX73 inverted microscope. Filter wheel 1: filter wheels with a selection of neutral density filters. Filter wheel 2: motorized filter wheel with a selection of bandpass filters. LED1: narrow-band LED with a central wavelength of 623 nm. LED2: a broad-band LED with warm white light.

illuminated by a high power solid-state Laser with a wavelength of 532 nm (gem, Laser Quantum). The reflected light serves as the reference beam. A low-noise photoreciever with a built-in 10 Hz low-pass filter (OE-200-SI, Femto) is used for detection. The position of the confocal pinhole needs to be adjusted for balancing the reflected and scatttered light.

3.5.2 Custom-built fluorescence microscope based on Olympus IX73

The localization microscopy is carried out with a custom-built fluorescence microscope based on an inverted microscope (IX 73, Olympus) (see Figure3.6). The sample is placed on a nanopositioning stage (P-545.xR85, Physik Instrumente). This microscope has the two illumination options: (1) focused laser illumination, where a multi-color fiber collimator (FC60, Schäfter+Kirchhoff) is installed to support switching the laser source; (2) wide-field continuous-wave illumination enabled by a narrow-band LED (SOLIS-623C, Thorlabs) and a broad-band LED (SOLIS-2C, Thorlabs) equipped with a selection of bandpass filters (Filter wheel 2). The illumination light is coupled to an oil immersion objective, and the emitted photons are collected with the same objective. The excitation and emission light are processed with a fluorescence filter set installed in the filter cube turret. The fluorescence light can be recorded by a CMOS camera (Zyla 4.2 Plus, Andor). Additionally, this

microscope also supports direct observation through the eyepiece and an external detection path such as an APD or a spectrometer.

We remark that the ventilation fan inside the CMOS camera can cause a mechanical vibration around 1 kHz. This fan can be manually switched off for a short period. Therefore, in a sensitive experiment that requires recording images using CMOS camera with a long integration time, it is better to use a CMOS camera with water cooling system.

CHAPTER 4

DNA-origami directed dynamic plasmonic walker

In the following section, we propose a dynamic light-matter interaction nanosystem enabled by the DNA origami techniques. Here the interaction of an isolated fluorophore molecule and a plasmonic nanorod can be modulated by moving the nanorod in steps of 7 nm along an origami template. This chapter contains the contribution from **Mo Lu**, Chao Zhou, Steffen Both, Markus Pfeiffer, Hao Yan, Thomas Weiss, Na Liu, and Klas Lindfors. I performed walker-release experiments and walking experiments. I characterized the process using single-molecule spectroscopy and scanning electron microscopy. This work is unpublished.

4.1 Introduction

DNA-origami techniques allow accurate placement and arrangement of light emitters and plasmonic nanoparticles. Incorporating DNA molecular machines, DNA-origami techniques enabled the fabrication of a dynamic plasmonic nanomachine with active optical properties that can be monitored *in situ*. So far, the dynamic optical response in the active plasmonic nanomachines is mainly realized by two means. The first way is to put plasmonic nanorods in a "cross" configuration, which gives rise to a change in the circular dichroism once the geometry is reconfigured [1, 24–26]. The second way is to use a gold nanoparticle as both a "slider" and a quencher, where a fluorescence spectrometer can used to monitor the distance-dependent non-radiative energy transfer between a gold nanoparticle and a fluorophore [195–197]. However, even though DNA-assembled active plasmonic nanomachines are expected to be an exceptional platform for studying light-matter interaction, plasmonic nanoparticles in all these structures serve mainly as reaction indicators to demonstrate the nanomachine's dynamic functionalities where little physical insight has been revealed. Most critically, as the dynamic movement of the nanomachine usually takes place in a liquid phase, most in-situ optical observations

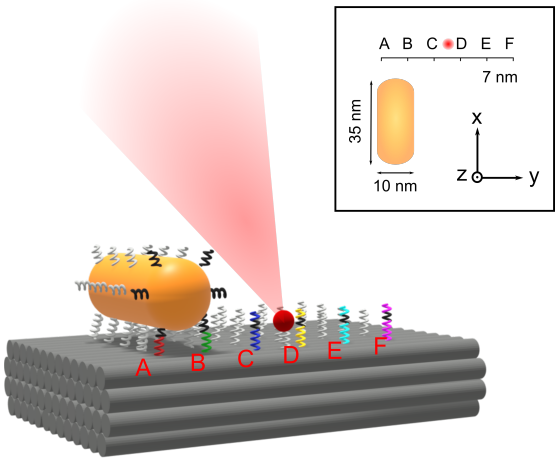

Figure 4.1: Schematic illustration of the plasmonic walker device. A gold nanorod (35 × 10 nm) and a fluorophore molecule (red sphere) are assembled on the DNA origami template (58 × 42 × 7(nm^2)). The gold nanorod is fully functionalized with DNA strands, which can execute a walking in a "rolling" fashion along the walking track. This walking track is made of extension strands from origami surface. It comprises six rows of footholds (A–F) forming five walking stations spaced by 7 nm. In each row, there are five binding sites with identical footholds, which are colored in the front line to illustrate the different strand segments. The fluorophore molecule (red sphere) is immobilized in the middle of footholds C and D. The red beam indicates the fluorescence emission from the molecule.

are performed on the ensemble level, which does not deliver dynamic information about the individual device. The ensemble-level measurement may disguise the diversity and even real product yield of the nanomachines, leading to a misinterpretation of the experimental result.

This chapter's motivation is to investigate the dynamic light-matter interaction on the level of single dynamic devices. Here, each DNA-origami assembled device contains a coupling system of a fluorophore and a plasmonic antenna. Their relative distance can be modulated dynamically, resulting in changes in the fluorophore's fluorescence intensity and lifetime. Using single-molecule spectroscopy, we can track in real-time the fluorescence changes in the individual device that is immobilized on a coverglass in the liquid cell.

4.2 Device design

The structural design of the walker device in this section is developed from Ref. [1]. Figure 4.1 illustrates the schematic of our walker device. In this device, a gold nanorod (AuNR) works as a plasmonic walker, which can perform stepwise progressive and reverse movements on the origami template. We position a fluorophore molecule (Atto 647N) at the selected walking step along the

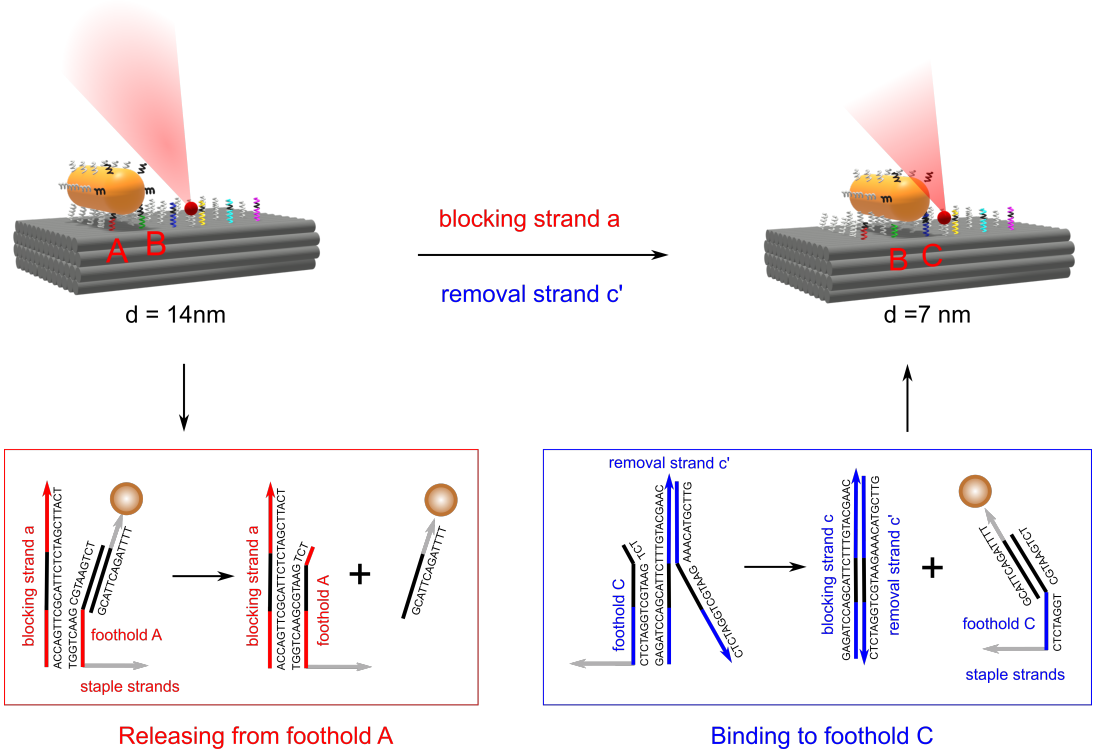

Figure 4.2: Walking mechanism. The walker is initially placed at AB. Adding blocking strand a triggers the dissociation of the walker's feet from footholds A. Simultaneously, adding removal strand c' releases the blocking strand c so that the walker's feet can bind to the footholds C. Therefore, a walker is moved from station AB to station BC. Adapted from Ref. [1]

.

nanorod's motion direction. Therefore, the nanorod can be programmed to approach or leave the fluorophore, giving rise to distance-dependent changes in the optical interaction.

The walking principle is illustrated in Figure 4.2. Six rows of foothold strands (A-F) with a separation of 7 nm extended from the origami surface, form the walking track. The nanorod is functionalized with foot strands and can bind with two foothold rows at each time. It is initially parked at station AB and the foothold rows C-F are deactivated by the corresponding blocking strands. The first walking step is triggered by adding the blocking strands for row A and removal strands for row C. Two toehold-mediated strand-displacement reactions take place simultaneously, resulting in a dissociation of the walker's feet from row A and activation of row C [198]. As row A now is deactivated by site-blocking, the walker, whose one-side feet are staying with row B, will eventually find foothold C. As a result, the walker moves one step forward from AB to BC. The following walking steps follow the same mechanism. Detailed description of the structural design and walking mechanism can be found in Ref. [1].

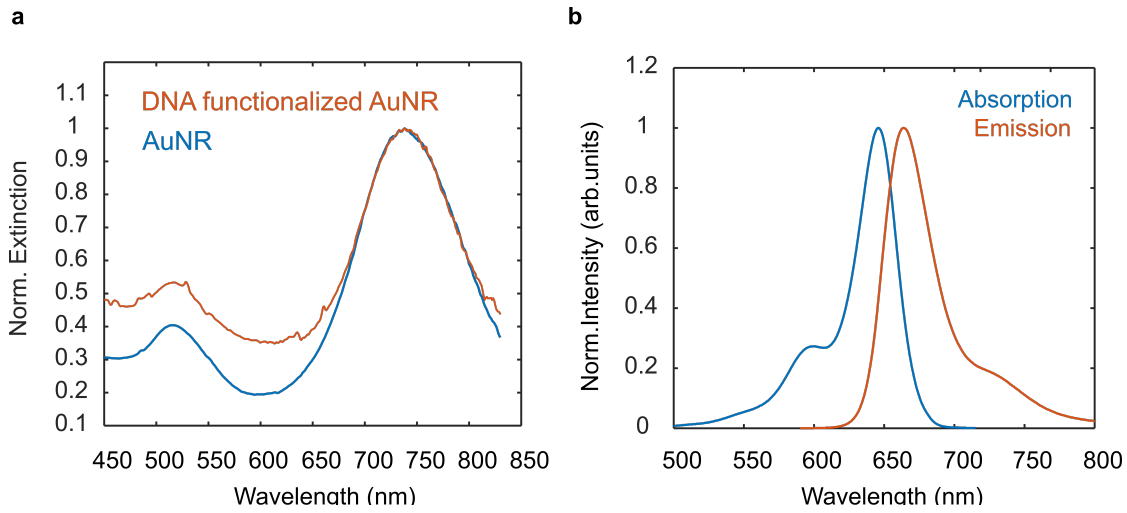

Figure 4.3: (**a**) Extinction spectra of gold nanorods and DNA functionalized gold nanorods used in the DNA-assembled plasmonic walker. The extinction intensity here is normalized to the maximum value. (**b**) Absorption and emission spectra of Atto 647N. Data are taken from the supplier [199]. The intensity here are normalized to the maximum value.

4.3 Optical interaction

For understanding the optical interaction between the gold nanorod and the fluorophore molecule, we perform finite element simulations using the commercial software COMSOL Multiphysics. Here we apply the Lorentz reciprocity theorem to deduce the modification in far-field fluorescence due to a local source near the plasmonic structure [200]. The incident plane wave is circularly polarized in xy plane and propogates along the substrate normal (z-axis). We use water as the medium surrounding the structure to simulate the buffer condition. The molecule is modeled as an electric point dipole.

We first consider the wavelength-dependent optical properties of the walker system (see Figure 4.4**a**). Here, the gold nanorod's displacement to the molecule is 0 nm, i.e., the nanorod is parked at station CD. The dipole orientation of the molecule is fixed along the x-axis. We can observe that the power dissipated to the nanorods $P_{\text{dissipation}}$ overwhelms over the power radiated into the far-field $P_{\text{far-field}}$, resulting in very low quantum yield. The quantum yield in the lower panel is calculated as the ratio of far-field radiation with the nanorod's presence and without, which gradually increases when the molecule's emission wavelength is red-detuned from the nanorod's plasmon resonance.

Figure 4.4**b** shows the calculated interaction enhancement (top) and quantum yield (bottom) as a function of nanorod displacement to molecule d for different dipole orientations. The emission wavelength is fixed at $\lambda = 670$ nm, corresponding to the emission maxima of Atto 647N (see Figure 4.3). The interaction enhancement is calculated as the ratio of the power radiated in the molecule's vicinity with the nanorod's presence and without. For a molecule with the dipole orientation along

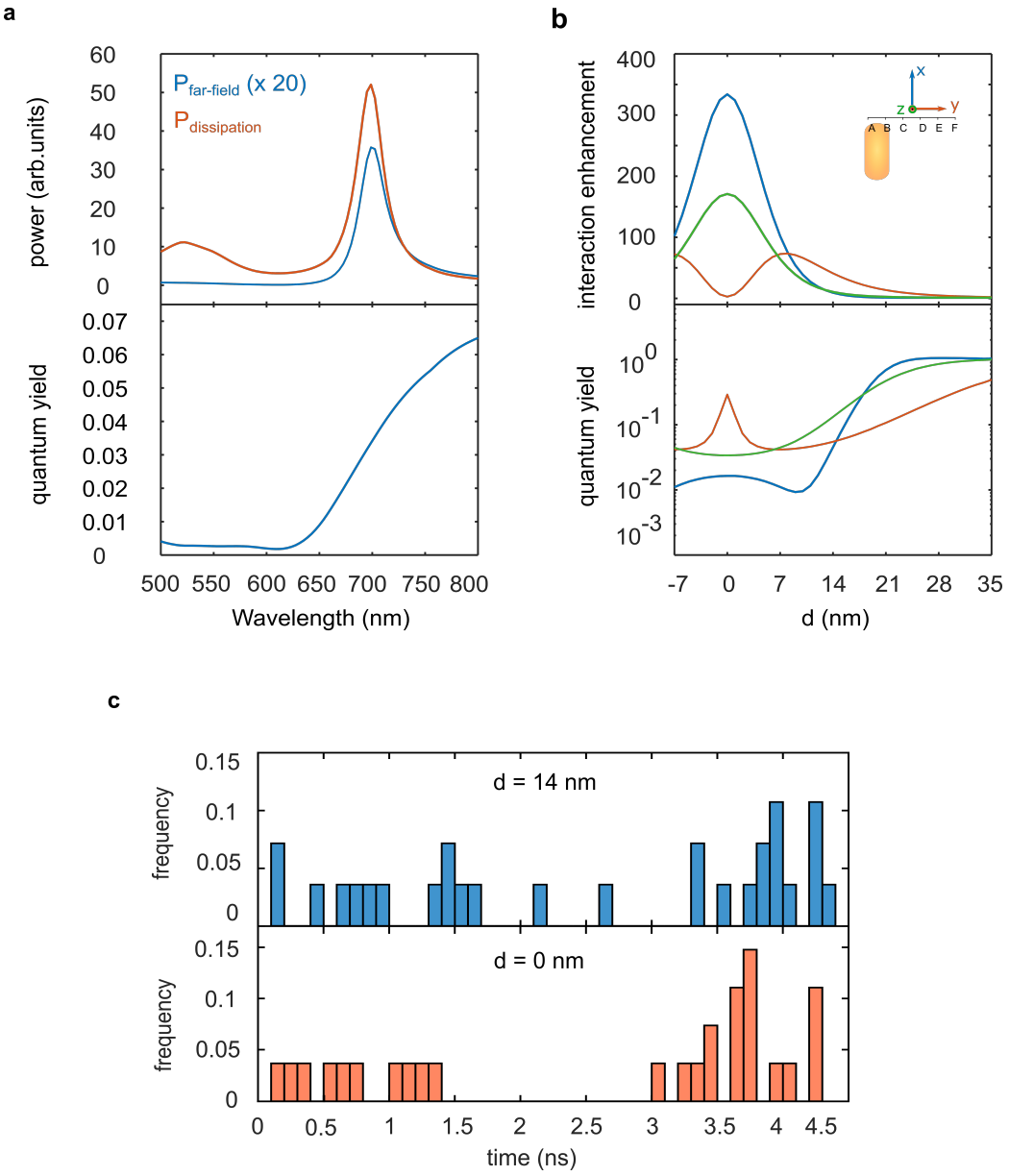

Figure 4.4: Quantification of the optical interaction. (**a**) Calculated dissipated power and far-field radiation power (top) and quantum yield (bottom) of the walker system as a function of emission wavelength. The displacement of nanorod to the fluorophore molecule is $d = 0$ nm. The far-field radiation power is magnified 20 times for better comparision. (**b**) Calculated interaction enhancement (top) and quantum yield for different dipole orientations as a function of displacement of nanorod to the fluorophore d. (**c**) Histograms of fluorescence lifetime for static devices with the displacement $d = 14$ nm (top) and $d = 0$ nm (bottom), respectively.

the nanorod's long axis (x-axis), the interaction becomes more pronounced as the nanorod is getting closer to the molecule, while the quantum yield drops drastically at the same time. For molecules with other dipole orientations, the interaction is rather weak and also shows distance dependency. From the simulation result, we can expect that the fluorescence emission in our walker system is partially quenched due to the gold nanorod's presence, while fluorescence lifetime will be shortened as the increase of the non-radiative rate. When the nanorod is next to the molecule, the emission is completely quenched.

We use single-molecule spectroscopy to experimentally characterize a number of static devices, where the gold nanorod is initially placed at $d = 0$ nm and $d = 14$ nm, respectively. The devices are immobilized on a coverglass in the liquid cell with a density of less than 1 device/μm^2 using the protocol in A.3. We measure the fluorescence decay trace of individual structures and plot the distribution of the fluorescence lifetimes in Figure 4.4**c**. Both devices show a peak around 4 ns, similar to the intrinsic fluorophore molecule, indicating an absence of gold nanorod in those devices. The peak below 1.5 ns suggests that the interaction with a nanorod modifies the fluorophore's emission. Most interestingly, there is an absence in the middle of the distribution for the device with $d = 0$ nm, which is different than the device with $d = 14$ nm. It indicates that in the device $d = 0$ nm, the nanorod is either missing or very close to the molecule, whereas, in the device $d = 14$ nm, the fluorescence decay rate can be partially modified by a nanorod in the vicinity.

4.4 Dynamic operation of gold nanorods

4.4.1 Release of gold nanorods

We first performed the release experiment of gold nanorods from the walker devices and track the change in gold nanorod's photoluminescence using single-molecule microscopy. The sample was illuminated with an excitation power of 120 µW at 630 nm wavelength, so that fluorophore molecules are bleached and only photoluminescence of gold nanorod can be detected. The fluorescence micrograph, therefore, contains only nanorods from the walker devices that are immobilized and free nanorods that are deposited on the surface (see Figure 4.5**a**). Then 1µL of solution with 100 µM releasing strand diluted with 100 µL PBS containing 10 mM $MgCl_2$, were added into the chamber to release the nanorods. The releasing strands contain a mixture of the blocking and removal strands solution of all footholds (A-F). After a few minutes of incubation, gold nanorods on the walker device start to detach from the origami template and diffuse into the buffer solution. We then collect fluorescence micrographs of the same region at a certain time interval after adding the releasing strands. We remark that each device is illuminated only for a few seconds a few times an hour to avoid destroying the origami structure by thermal heating.

Figure 4.5**a** displays a comparison of fluorescence micrographs before and after adding the releasing

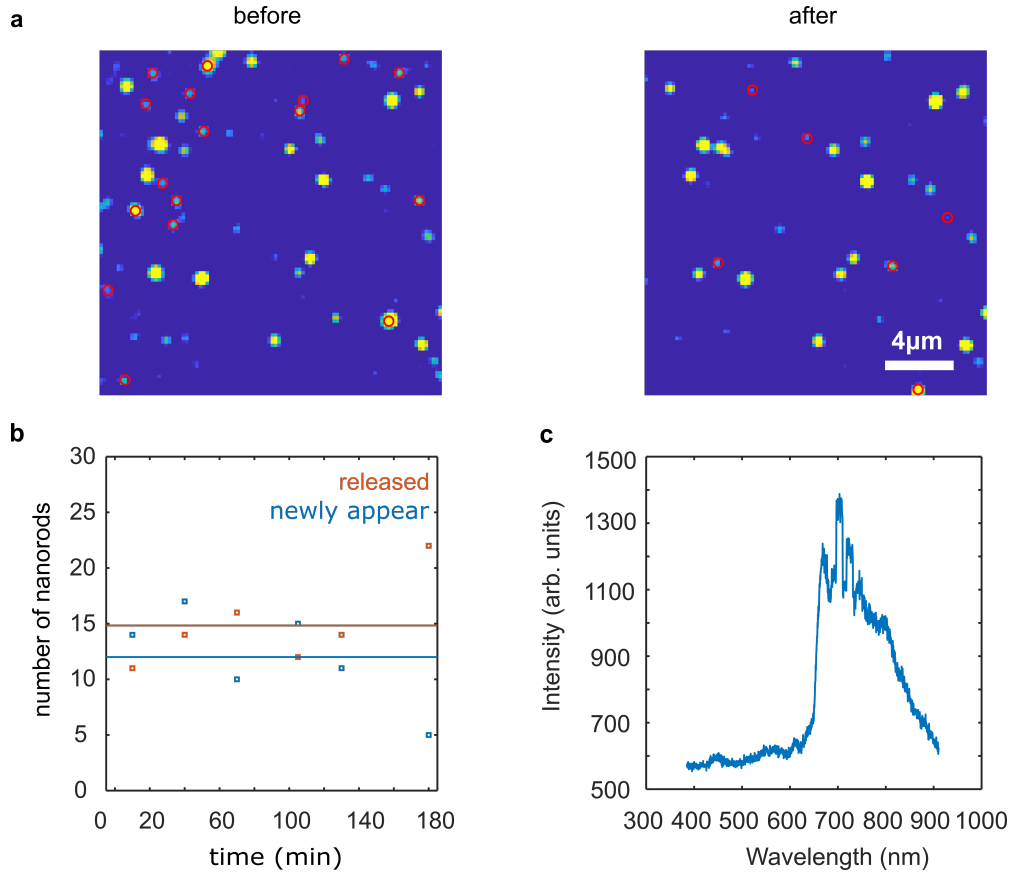

Figure 4.5: Release experiment of gold nanorods. (**a**) Fluorescence micrograph of gold nanorods before (left) and 180 minutes after (right) adding the releasing strands. We applied the median filter on the micrograph to remove the background noise for better presentation. The red circles on the left illustrate nanorods that are removed. The red circles on the right image illustrate nanorods that appear 180 minutes after adding releasing strands. (**b**) Evolution of the number of nanorods that are released and appear with time. The solid lines illustrate the mean value. (**c**) Photoluminescence spectra of a single DNA functionalized gold nanorod.

strands. We can observe that more than 60% of nanorods are removed. Additionally, there are a few newly appear nanorods, which were not detected before initiating the release. This may come from the deposition of nanorods from the solution. We plot the evolution of the number of nanorods that are removed and appear as a function of elapsed time in Figure 4.5**b**. The releasement for most of the nanorods already occurs in the first 15 minutes. Meanwhile, there is an increasing number of nanorods from the solution going to the surface over time.

4.4.2 One-step walking

We next investigated the dynamic light-matter interaction by performing the walking experiment. The illumination power is attenuated to 1 µW so that the photoluminescence of gold nanorod is neglectable compared to the fluorophore molecule. In the fluorescence micrograph shown in Figure 4.6, the observed bright spots correspond to immobilized individual structures. All measurements are performed using circularly polarized incident light in order to minimize the influence of the orientation of the absorption dipole moment of the fluorophore. The nanorods in the walker devices were initially parked at station CD with a $d = 0$ nm displacement. After identifying a region with sufficient devices, a 100 µL buffer solution containing walking strands (blocking strands d and removal strands b') was added into the liquid cell to initiate walking. Here an incubation of 20 minutes is required for the strand replacement reaction [1]. We recorded the fluorescence micrographs and fluorescence decay traces of selected individual devices in the same region before adding the walking strands (see Figure 4.6**a**) and 30 minutes after adding the walking strands (see Figure 4.6**b**). As a final step, we added the release strands to remove all nanorods from walker structures and recorded the fluorescence micrograph (see Figure 4.6**c**).

We perform a colocalization study on the walker device in each fluorescence micrograph using a custom-written Matlab code. Those devices emerging only after walking and releasing are marked with red crosses. Here we can observe that several fluorophore molecules appear after walking, indicating that the fluorophore's emission is less suppressed as the nanorod is moving away. This is consistent with the lifetime correlation, shown in Figure 4.6**d**, where several devices have experienced an increase of fluorescence lifetime. Finally, there is an outburst of emission from the fluorophore molecule after releasing the nanorods, as the fluorophore's emission is no-longer dissipated into metal.

4.4.3 Progressive and reverse walking

We continue by performing a progressive and reversibly walking experiment involving four walking steps. As illustrated in Figure 4.7**a**, the walking route starts from a displacement of 14 nm, reaches a position next to the fluorophore, and returns to the starting point. Here we expect that the fluorescence intensity of a walker device experiences a change in a sequence of "bright-dark-bright". Similar to before, we first identify a region with sufficient devices and then record fluorescence micrographs

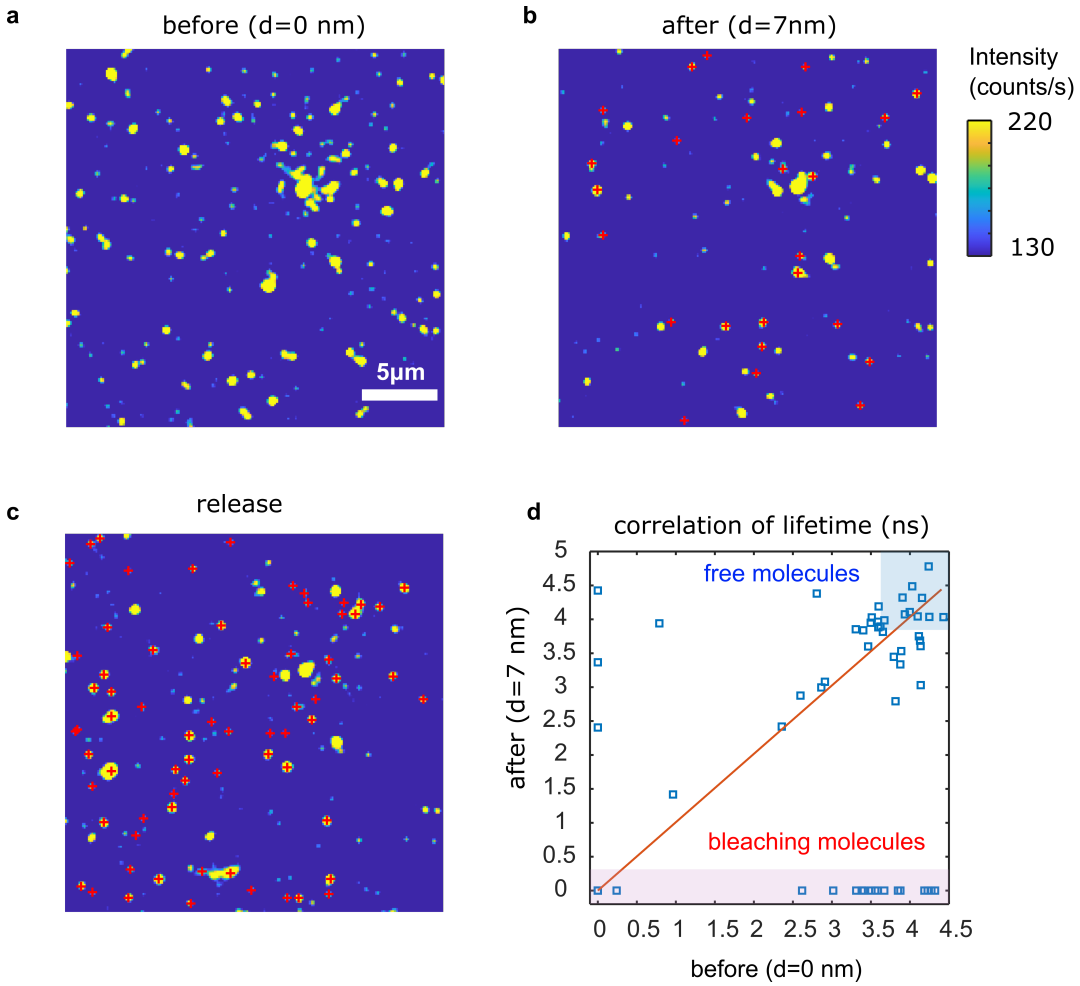

Figure 4.6: One-step walking experiment. (**a**) Fluorescence micrograph of the immobilized devices before walking. The nanorod is placed at station CD with a displacement $d = 0$ nm. (**b**) fluorescence micrograph of the immobilized devices after walking. The nanorod is expected to be at station BC with a displacement $d = 7$ nm. (**c**) fluorescence micrograph of the immobilized devices after releasing the nanorods. The red cross marks the device in (**b**) and (**c**), which were not found in (**a**). (**d**) a correlation of the fluorescence lifetime before and after the walk. Each data point corresponds to an individual device. The diagonal line illustrates the situation for no change in lifetime during the walk. We additionally mark the devices that are most likely with bleached molecules or missing nanorods.

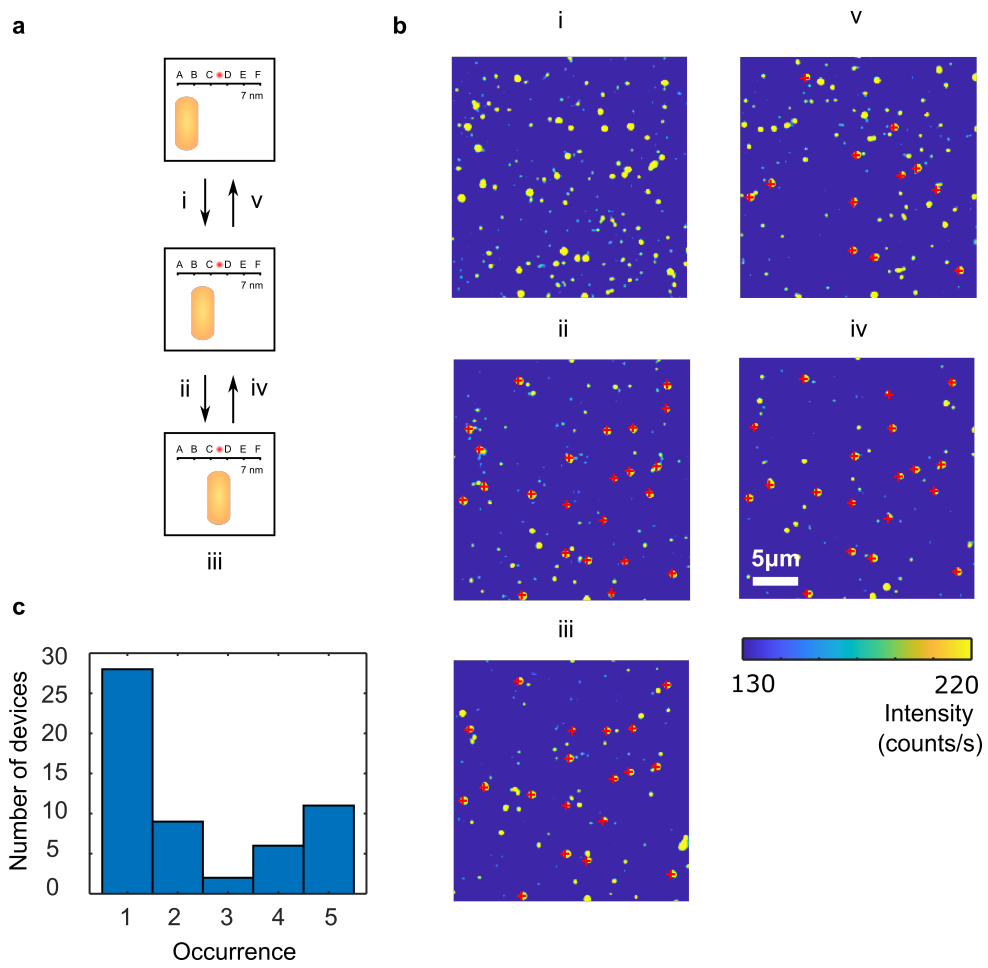

Figure 4.7: Progressive and reverse walking with four steps. (**a**) Schematic illustration of the walking route: AB-BC-CD-BC-AB. (**b**) A sequence of fluorescence micrographs ($i - v$) were recorded before and after each walking step. The red cross in the fluorescence micrograph $ii - v$ illustrate the device that colocalizes with a device in the fluorescence micrograph i that was recorded before walking. (**c**) Statistics of the same device's occurrence during walking.

during the walking process. We remark that for multiple steps operation on the nanorod walker, the buffer solution needs to be changed into fresh ones between two steps so that the released strands in the previous step will not disturb the following reaction.

The recorded fluorescence micrographs are presented as the walking sequence in Figure 4.7**b**. Here, fluorescence micrograph i was recorded before initiating the walk. The devices observed in the micrograph that are recorded after each walking step and colocalize with the devices in the micrograph i are marked with red crosses. The occurrence of identical devices during the walking process are summarized in Figure 4.7**c**. From here, we can observe that a large number of devices disappeared during the walk, which most likely arised from the photobleaching of the fluorophore.

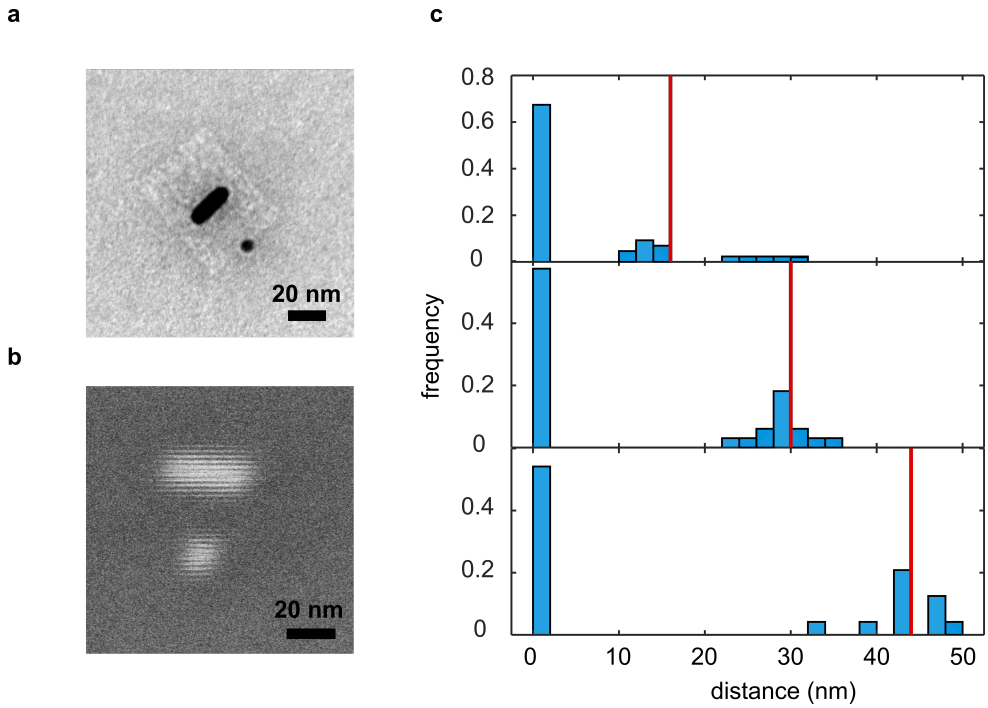

Figure 4.8: (**a**) Transmission electron micrograph of a walker device that contains a gold nanorod (35 nm×10 nm) and a gold nanosphere (10 nm in diameter). The nominal nanorod-sphere distance is 30 nm. (**b**) Scanning electron micrograph of a walker device with the same design as in (**a**). (**c**) Statistics of the relative distance of nanorod-nanosphere for three walker devices determined by transmission electron microscopy. The peak at 0 nm distance stands for the devices that are missing particles or contain more than one nanorods. The solid red lines illustrate the nominal relative nanorod-nanosphere distance: 16 nm, 30 nm, 44 nm (from top to down).

Additionally, many devices did not seem to change during walking. Only very few devices fulfilled the "bright-dark-bright" trend, which is insufficient to draw a conclusion.

4.5 *Ex-situ* characterization with electron microscopy

In our experiment, the origami template, which contains a walking track, is immobilized on the surface. Thus the walking yield of a walker device could be different from that in solution. For example, in solution, the 2D rectangular origami template is naturally bending at a certain angle, facilitating the strand displacement reaction [201, 202]. Additionally, as Bovine serum albumin (BSA) can bind to gold nanoparticles easily [203], it is also possible that the gold nanorods bind to BSA passivated surface during walking.

To investigate the nanorod walker devices' walking yield on the surface, we additionally fabricated the walker devices that would allow *ex-situ* electron microscopy characterization. In this structure, a

gold nanosphere with a 10 nm diameter is assembled on the origami template's edge, serving as a reference coordinate. A plasmonic nanorod is placed at a nominal distance with respect to the gold nanosphere (see Figure 4.8**a**). We first characterized a number of walker devices in a solution using transmission electron microscopy TEM, where the nanorods are placed at different positions. The statistics of the relative distance determined with TEM for each walker devices is shown in Figure 4.8**c**. We can observe that more than 50 % of the devices are wrongly assembled, either missing nanorods or containing multiple nanorods in one device. For the devices containing only one nanorod and one nanosphere, the relative distance distribution is very broad. In particular, there are two peaks in the distribution for the devices with 16 nm nominal nanorod-nanosphere separation, which indicates that the assembly accuracy decreases if two nanoparticles are positioned with a close distance.

We immobilized the walker devices on the cover glass in a liquid cell using the same approach as in Section 4.4. After performing two-step progressive walking on the walker devices, the coverglass in the liquid cell was then taken out, rinsed with deionized water to remove the salts in the buffer solution, and coated with a thin layer of conductive polymer. Then we used scanning electron microscopy (SEM) to characterize the change in relative distance between a nanorod and a nanosphere (see Figure 4.8**b**). However, it is technically difficult to make such an experiment under SEM. Apart from the imaging challenge due to the nanoparticles' small dimension, the broad distribution in the relative distance that is revealed by TEM also introduces the ambiguity. Moreover, many gold nanoparticles are detached or deformed in the post-processing procedures after walking experiments so that very few devices can be found under SEM that contain both nanorod and nanosphere.

4.6 Conclusions

In this chapter, we have studied a DNA-origami directed plasmonic nanosystem using single-molecule spectroscopy and SEM. We first performed a numerical simulation to understand the optical interaction in this nanosystem. It shows that the fluorescence of the fluorophore molecule is partially quenched due to the presence of the plasmonic nanorod. The quenching effect becomes more pronounced as the nanorod moves closer to the molecule. This is experimentally proved by the fluorescence lifetime measurement of a number of static devices. Second, we have demonstrated that on the addition of releasing strands, the gold nanorods can be removed from the origami templates and diffused into the solution. This has been observed the brightness change in both gold nanorods and the fluorophore molecule. Additionally, when the nanorods are moved 7 nm away from the fluorophore, we have observed that a number of devices are lightened up, and the few devices experienced an increase of lifetime. However, the observation from the multi-step walking experiment is rather inclusive, which is different from the case in Ref. [1], where the walking process has high fidelity.

The observed differences in the walking experiment can be caused for several reasons. First, the walking yield could be different in our case as the origami template containing walking track is

immobilized on the surface. Second, the TEM images indicate that there is a large portion of assembly imperfection in the sample. This imperfection, including missing nanoparticles due to the sample degradation, or the nanorods attached to the wrong foothold, impedes the walking process. A cease in the walking process will not be revealed in the ensemble-level circular dichroism measurement, but it can be observed and raise ambiguity in individual device studies. Most importantly, the optical interaction between a nanorod and a the molecule is very sensitive to the molecule's dipole orientation, nanorod geometry, and the local environment. For example, the variation of the aspect ratio in nanorod geometry can significantly change the plasmon resonance, resulting in a modification in the interaction with the fluorophore. Additionally, the nanorods are only captured on the side by footholds rows, so they can make thermal vibrations along the x-axis. As we are hunting for a very small change between a partial quenching and a complete quenching of the fluorophore, the factors mentioned above can make the observation even more difficult.

CHAPTER 5

DNA-origami directed dynamic fluorophore molecule walker

In this chapter, we have demonstrated a dynamic light-matter interaction nanosystem powered by DNAzyme-RNA reactions. Here, each DNA-origami assembled device contains a coupling system of a fluorophore and a plasmonic gap antenna that consists of two 60 nm gold nanoparticles. In contrast to the design in Chapter.4, their relative distance is modulated by the autonomous and unidirectional motion of a fluorophore walker. We first demonstrated the walking mechanism with an ensemble Fret experiment in the absence of gold nanoparticles. The fluorescence intensity of the fluorophore molecule, which assembled on the walking track, shows a trend that first decreases and then increases when a quencher molecule passes by. Then we optically tracked a number of devices, where a single fluorophore is transported along a zigzag track into the hotspot of a plasmonic nanoantenna. Our key result is the observation of accelerated fluorescence decay and simultaneously increased fluorescence brightness when the fluorophore enters a nanoantenna hotspot. Our experimental results are in agreement with simulations of the light-matter interaction. Such autonomous walking is based on a burnt-bridge mechanism, thus giving rise to unidirectional movements without any external intervention.

This chapter contains the contribution from **Mo Lu**, Ling Xin, Chao Zhou, Steffen Both, Markus Pfeiffer, Maximilian J. Urban, Hao Yan, Thomas Weiss, Na Liu and Klas Lindfors. I performed the walking experiment, optical characterization, and interpretation of the optical results. I prepared figures, supplementary materials, and wrote the methods part of the publication. I participated in finalizing the manuscript in close collaboration with Klas Lindfors. The following section of this chapter containing the published result is replaced by the Ref. [16] according to *Promotionsordnung der Mathematisch-Naturwissenschaftlichen Fakultät der Universität zu Köln vom März 2020 § 12 (1).*

CHAPTER 6

Plasmonically enhanced photoluminescence blinking from graphene nanoribbons

In this chapter, we probe the origin of the photoluminescence blinking in seven atom wide semiconducting armchair-edge graphene nanoribbons (7-AGNRs) observed previously by our group [2]. Importantly, the absence of Raman features from GNRs in the spectra of a photoluminescence burst indicates that the blinking purely relates to the emission process. By varying the size and material of optical antennas, we tune the spectral position of the plasmon through the fluorescence spectrum of the GNRs influencing the field enhancement and spatial confinement of the plasmonic hotspot at the emission wavelength. We find a clear correlation between the plasmonic field enhancement and the amplitude of the blinking events. This indicates that the plasmonic enhancement is the key element to being able to observe photoluminescence blinking from nanoribbons and that the blinking is thus intrinsic to the 7-AGNRs. Our experimental results thus exclude charge transfer between the metallic nanostructure and the semiconducting ribbons from being the source of the blinking.

This chapter contains contribution from **Mo Lu**, Markus Pfeiffer, Boris Vladimirovich Senkovskiy, Danny HG Haberer-Gehrmann, Dirk Hertel, Klaus Meerholz, Yoichi Ando, Felix Fischer, Alexander Grüneis, Klas Lindfors. I performed the optical characterization and data analysis, including extinction measurements, photoluminescence imaging, and super-resolution study. I extracted the data from numerical simulation, whose model was initially developed by Markus Pfeiffer. I wrote the manuscript, prepared the supplementary materials, and finalized them in close collaboration with Klas Lindfors. The following section of this chapter containing the published result is replaced by the Ref. [104] in publication according to *Promotionsordnung der Mathematisch-Naturwissenschaftlichen Fakultät der Universität zu Köln vom März 2020 § 12 (1).*

CHAPTER 7

Summary and Outlook

This dissertation applies the plasmon-exciton coupling effect in DNA origami nanosystems and nanostructured graphene to gain insight into nanoscale motion and interaction below the diffraction limit. The plasmon-exciton interaction is explored by using a far-field optical technique, in particular single-molecule spectroscopy. On the basis of the methods and findings provided here, more complex and intriguing plasmon-exciton coupling experiments can be proposed.

In the first part of the dissertation, we have discussed the plasmon-fluorophore dynamic nanosystem enabled by DNA origami techniques. This system was explored experimentally and theoretically. We first studied a plasmonic nanorod walker device, where the interaction of a fluorophore and nanorod can be modulated by moving the nanorod. We have demonstrated that the nanorod can be released from the origami template, but the observation of the dynamic interaction between the nanorod and the fluorophore is rather inconclusive. Either the walking process is hindered, or the coupling between the nanorod and fluorophore is not very efficient.

We then studied a dynamic nanosystem where two 60 nm gold nanoparticles and an RNA-coated track were assembled on a three-dimensional origami template. A fluorophore molecule attached to DNAzyme strands acts as an autonomous walker. By adding trigger DNA strand and divalent metal ions, the walker moves unidirectionally along the track into the hotspot using burnt-bridge mechanisms. As the fluorophore molecule approaches the hotspot, the fluorescence intensity increases, and the fluorescence lifetime decreases. We additionally discuss that the importance of dye orientation for fluorescence enhancement. For example, if the dye molecule can rotate freely at a time scale shorter than the fluorescence lifetime, it can be considered as an isotropic emitter.

Our findings in origami-directed plasmonic nanosystems have provided insights into designing dynamic plasmonic nanosystems: (1) there is always a ”trade-off” between flexibility and stability. In order to achieve a dynamic system that is optically resolvable, it is important to choose an interactive

manner of the antenna and the emitter that gives rise to a robust signal with a high signal-to-noise ratio. (2) DNA origami provides a rather complex chemical environment, where some species can chemically quench the molecule's fluorescence or influence the dipole orientation. It requires careful consideration of the chemical environment and the engineering of the photophysics of the fluorophore. (3) the origami assembled nanostructures will degrade with time and temperature (see A.5). It is therefore important to measure the sample as fresh as possible. Furthermore, the design has to consider that the plasmonic particle does not generate too much heat to destroy the origami assemblies under laser illumination.

DNA origami-directed dynamic plasmonic nanosystem provides a platform that allows to optically track the nanoscale motion of a DNA nanomachine with high temporal and spatial resolution. Using single-molecule microscopy, we can monitor the nanoscale motion on the individual device and gain the information of diversity and fidelity. Moreover, complex dynamic plasmonic architectures with tailored functionalities can be achieved using DNA origami assemblies. For instance, incorporating multiple fluorophores such as semiconductor quantum dots with a plasmonic antenna could allow for dynamic switching of the interactions between the emitters and their coupling to the far-field.

In the second part, this dissertation employs a plasmonic antenna to probe the origin of the photoluminescence blinking of the 7-AGNRs. By varying the size and material, we observed a clear correlation between field enhancement and the blinking amplitude of the GNRs. Importantly, we have proved that the observation of the photoluminescence blinking does not require direct contact with the metal nanostructure. This indicates that the photoluminescence of the blinking is purely coming from the intrinsic nature of the GNRs. It further strengthens our hypothesis that the Tamm states, which are spatially located at the termini of the 7-AGNR, are responsible for the fluorescence blinking. Although many open questions, such as the nature of the dark and bright states during blinking and the influence of defects, require further study, our result opens an inspiring direction to understand the light emission process for 7-AGNRs.

The emission blinking and spectral diffusion we observed in plasmonic-enhanced 7-AGNRs are the characteristic features of a single quantum emitter. It suggests that plasmonic-enhanced 7-AGNRs could be used as single-photon sources. In contrast to the conventional organic fluorophore, this system has the following advantages: (1) The ribbons are significantly more photostable, and we didn't observe any photobleaching with one week of continuous light illumination; (2) 7-AGNR can potentially be excited electrically; (3) 7-AGNR is more robust and compatible with standard top-down techniques such as electron beam lithography; (4) It is possible to prepare aligned GNRs in large areas, allowing full control of the dipole orientation. Plasmonic-enhanced GNRs can therefore be used as a novel nanoscale semiconductor for plasmonic circuits.

APPENDIX A

Scientific Appendix

A.1 Atto 647N molecules embedded in PVA thin film

A cover glass (Plano) is cleaned by Mucasol universal detergent (Sigma Aldrich) for 10 minutes in an ultrasound bath and 10 minutes in deionized water. This step is to remove the fluorescent organic ligands. Atto 647N is purchased from Atto-Tec. We diluted the Atto 647N solution into DMF suspensions with the concentration in the range of picomolar. The diluted Atto 647N solution is mixed with Polyvinyl alcohol aqueous solution and spin-coated at 3000 rpm for one minute.

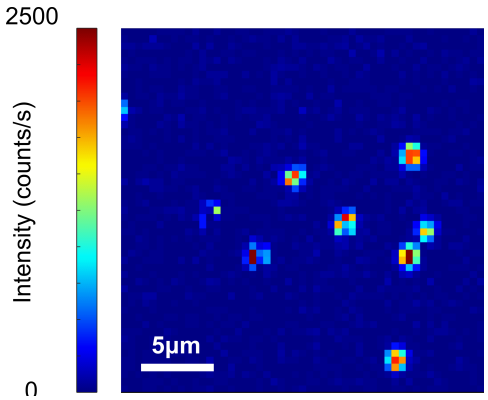

Figure A.1: Fluorescence micrograph of Atto 647N embedded in PVA thin film.

A.2 Colocalization of two color fluorophore system

Here two kinds of the fluorophore are assembled on the plasmonic nanorod walker device in Chapter 4. We used lasers with two different incident wavelengths to excite the same region. The colocalization devices are marked with red crosses.

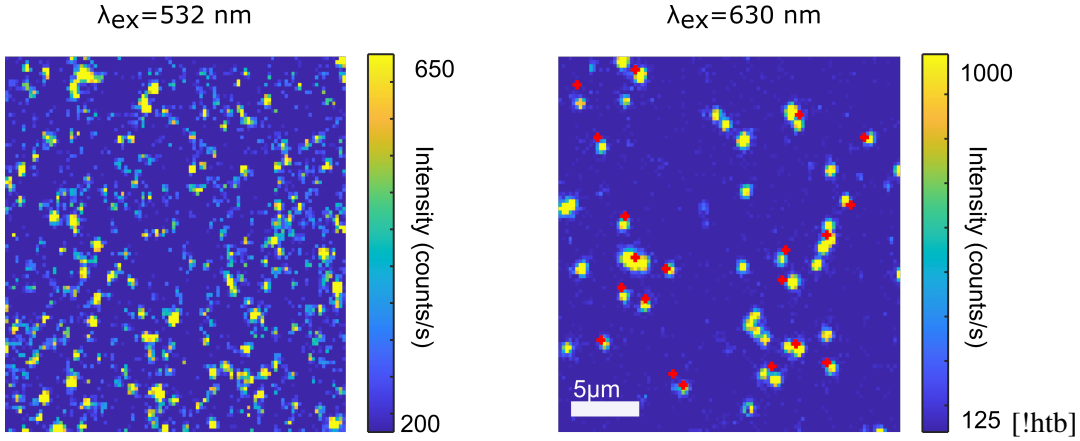

Figure A.2: Fluorescence micrographs of the DNA-origami assembled plasmonic system with two color fluorophore (Atto 647N and Atto 525). The excitation wavelength is 532 nm (left) and 630 nm (right), respectively. [!htb]

A.3 Immobilization of the DNA origami devices

DNA origami assembled plasmonic devices in Chapter 4 and Chapter 5 were immobilized on a BSA-biotin-neutravidin surface in a commercial LabTek chamber using the procedure of Ref. [204]:

1. The LabTek chambers were washed 3 times with 500 μL of PBS.
2. The chambers were incubated with 300 μL of BSA-biotin solution (0.5 mg/mL in PBS) for 10 min.
3. BSA-biotin solution was removed and the chambers were washed 3 times with 650 μL of PBS.
4. The chambers were incubated with 300 μL of neutravidin solution (0.8 mg/mL in PBS) for 5 min.
5. Neutravidin solution was removed and the chambers were washed 3 times with 650 μL of PBS.
6. 10 μL of the gel purified dynamic devices solution and control samples were diluted with 300 μL of PBS with the 11 mM $MgCl_2$ solution, respectively. Each LabTek chamber was then incubated with a specific sample solution for 3h. The chambers were then washed three times with 650 μL of PBS with the 11 mM $MgCl_2$. Each chamber was kept in 300 μL of PBS with the 11 mM $MgCl_2$ solution at 4 °C.

A.4 DNA functionalization of the gold nanoparticles

The gold nanoparticles (AuNP) in Chapter 5 are functionalized with 5' end thiolated DNA (HS-T15, 5'-HS-TTT TTT TTT TTT TTT-3' purchased from Sigma Aldrich, with RP1 purification). The functionalization was carried out following the procedure below. Thiolated DNA strands were incubated with TCEP [tris(2-carboxyethyl) phosphine] for at least 1 h to reduce the disulfide bonds. The ratio of DNA:TECP was 1:200. Before functionalization, the AuNPs were spun down and then resuspended with modification buffer (0.5 × TBE buffer containing 0.02% of SDS, pH 8.0) to remove excess cetyltrimethylammonium bromide. AuNPs (0.1 nM, 0.5 mL) were mixed with 80 μM thiolated DNA strands (5 μL). We used a well-established salt aging procedure [205], and the final concentration of NaCl reached 0.7 M. The AuNPs functionalized with DNA were then purified to remove excess free DNA strands by centrifugation. At least five times of centrifugation steps at a rate of 3000g for 5 min were carried out. Each time, the supernatant was carefully removed and then the AuNPs were resuspended in modification buffer. The supernatant was then removed and the remaining AuNPs were mixed with the purified dynamic/static devices with a ratio of 8:1 in modification buffer with 10 mM $MgCl_2$. The mixture was incubated overnight at room temperature.

A.5 Degradation of the DNA fluorophore walker with time

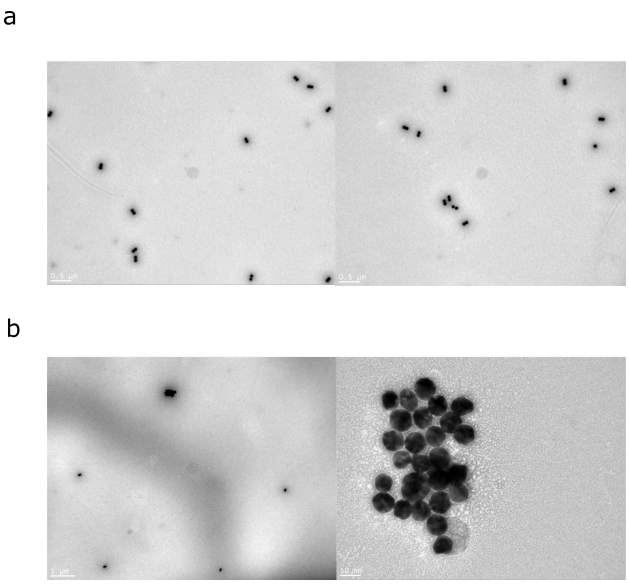

Figure A.3: Degradation of devices in Chapter 5 with time. (**a**) TEM microsgraph of freshly made devices. (**b**) TEM microsgraph of devices after 10 days.

A.6 Layout of aluminium plasmonic antenna

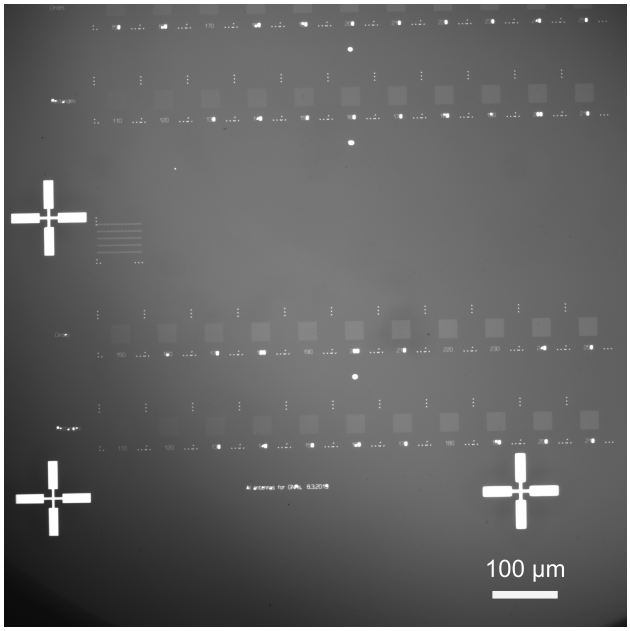

Figure A.4: A wide-field reflection image shows the layout of aluminium antenna that were studied in Chapter 6

APPENDIX B

List of publication

B.1 List of Publications

[16] Ling Xin[#], **Mo Lu**[#], Steffen Both, Markus Pfeiffer, Maximilian J. Urban, Chao Zhou, Hao Yan, Thomas Weiss, Na Liu, and Klas Lindfors
Watching a Single Fluorophore Molecule Walk into a Plasmonic Hotspot
ACS Photonics 2019, **6**, 4, 985–993
[#]These authors contribute equally.

[104] **Mo Lu**, Markus Pfeiffer, Boris Vladimirovich Senkovskiy, Danny H G Haberer-Gehrmann, Dirk Hertel, Klaus Meerholz, Yoichi Ando, Felix Fischer, Alexander Grüneis and Klas Lindfors
Probing the origin of photoluminescence blinking in graphene nanoribbons: Influence of plasmonic field enhancement
2D Materials 2020, **7**, 4, 045009

B.2 Conference as presenting author

[1] Klas Lindfors, Mo Lu, Thomas Weiss, Hao Yan, and Na Liu, *DNA-directed assembly of complex plasmonic nanoantenna for controlled*, Volkswagen Stiftung syposium: functional macroscopic systems, Hannover, Germany, poster (2016)

[2] Mo Lu, Markus Pfeiffer, Chao Zhou, Na Liu, and Klas Lindfors,*Optical microspectroscopy of DNA origami-assembled complex and dynamic plasmonic nanostructure*, DPG spring meeting, Dresden, Germany, Poster O 389(2017)

[3] Mo Lu, Markus Pfeiffer, Chao Zhou, Ling Xin, Steffen Both, Thomas Weiss, Na Liu, and Klas Lindfors, *Optical microspectroscopy of DNA origami-assembled complex and dynamic plasmonic nanostructure*, 20 Years Nano-optics Symposium, Erlangen, Germany, poster (2017)

[4] Mo Lu, Markus Pfeiffer, Ling Xin, Steffen Both , Thomas Weiss, Na Liu, and Klas Lindfors, *Watching a single molecule walk into the hotspot of a plasmonic antenna*, The 15th international conference on near field optics, nanophotonics, and related techniques, Troyes, France, poster (2018).

[5] Mo Lu, Markus Pfeiffer, Boris V. Senkovskiy, Danny Haberer, Felix R.Fischer, Fan Yang, Klaus Meerholz, Yoichi Ando, Alexander Grüneis, and Klas Lindfors, *Dependence of graphene photoluminescence blinking on the local field enhancement*, DPG Spring meeting, Regensburg, Germany, Talk O 841 (2019).

[6] Mo Lu, Ling Xin, Steffen Both, Markus Pfeiffer, Maximilian J. Urban, Chao Zhou, Hao Yan, Thomas Weiss, Na Liu, and Klas Lindfors,*Watching a single molecule walk into the hotspot of a plasmonic antenna*, DPG Spring meeting, Regensburg, Germany, Talk O 841 (2019).

[7] Mo Lu, Markus Pfeiffer, Boris V. Senkovskiy, Danny Haberer, Felix R.Fischer, Fan Yang, Klaus Meerholz, Yoichi Ando, Alexander Grüneis, and Klas Lindfors, *Observation of bright room-temperature photoluminescence bursts from armchair graphene nanoribbons using plasmonic nanoantennas*, the 9th international conference on surface plasmon photonics, Copenhagen, Denmark, poster (2019).

[8] Mo Lu, Ling Xin, Steffen Both, Markus Pfeiffer, Maximilian J. Urban, Chao Zhou, Hao Yan, Thomas Weiss, Na Liu, and Klas Lindfors,*Watching a single molecule walk into the hotspot of a plasmonic antenna*, 25th International workshop on single molecule spectroscopy and super-resolution microscopy in the life science, Berlin, Germany, talk (2019).

[9] Mo Lu, Ling Xin, Steffen Both, Maximilian J. Urban, Markus Pfeiffer, Boris V. Senkovskiy, Danny Haberer, Chao Zhou, Felix R.Fischer, Yoichi Ando, Klaus Meerholz, Hao Yan, Thomas Weiss, Na Liu, Alexander Grüneis, and Klas Lindfors, *Plasmon-exciton coupling: from DNA origami to nanostructured graphene*, PIERS 2019 in Xiamen, China, invited talk, SC2: Nanophotonics for Integration, Communication, and Biomedicine Applications (2019).

Bibliography

[1] C. Zhou, X. Duan and N. Liu, *A plasmonic nanorod that walks on DNA origami*, Nature communications **6** (2015) 1 (cit. on pp. v, 2, 23, 25, 41–43, 48, 52).

[2] M. Pfeiffer, B. V. Senkovskiy, D. Haberer, F. R. Fischer, F. Yang, K. Meerholz, Y. Ando, A. Grüneis and K. Lindfors, *Observation of Room-Temperature Photoluminescence Blinking in Armchair-Edge Graphene Nanoribbons*, Nano Letters **18** (2018) 7038 (cit. on pp. v, 2, 26, 27, 57).

[3] G. E. Moore et al., *Cramming more components onto integrated circuits*, 1965 (cit. on p. 1).

[4] L. Novotny and N. Van Hulst, *Antennas for light*, Nature photonics **5** (2011) 83 (cit. on pp. 1, 14).

[5] L. Cao, X. Wang, M. J. Meziani, F. Lu, H. Wang, P. G. Luo, Y. Lin, B. A. Harruff, L. M. Veca, D. Murray et al., *Carbon dots for multiphoton bioimaging*, Journal of the American Chemical Society **129** (2007) 11318 (cit. on pp. 1, 15).

[6] Y. Yang, Q. Zhao, W. Feng and F. Li, *Luminescent chemodosimeters for bioimaging*, Chemical Reviews **113** (2013) 192 (cit. on pp. 1, 15).

[7] A. Kuhn, M. Hennrich and G. Rempe, *Deterministic single-photon source for distributed quantum networking*, Physical review letters **89** (2002) 067901 (cit. on pp. 1, 15).

[8] A. Wallraff, D. I. Schuster, A. Blais, L. Frunzio, R.-S. Huang, J. Majer, S. Kumar, S. M. Girvin and R. J. Schoelkopf, *Strong coupling of a single photon to a superconducting qubit using circuit quantum electrodynamics*, Nature **431** (2004) 162 (cit. on pp. 1, 15).

[9] J. Sprengers, A. Gaggero, D. Sahin, S. Jahanmirinejad, G. Frucci, F. Mattioli, R. Leoni, J. Beetz, M. Lermer, M. Kamp et al., *Waveguide superconducting single-photon detectors for integrated quantum photonic circuits*, Applied Physics Letters **99** (2011) 181110 (cit. on pp. 1, 15).

[10] A. Kinkhabwala, Z. Yu, S. Fan, Y. Avlasevich, K. Müllen and W. Moerner, *Large single-molecule fluorescence enhancements produced by a bowtie nanoantenna*, Nature Photonics **3** (2009) 654 (cit. on pp. 1, 13, 20).

[11] P. Bharadwaj and L. Novotny,
Plasmon-enhanced photoemission from a single Y3N@ C80 fullerene,
The Journal of Physical Chemistry C **114** (2010) 7444 (cit. on pp. 1, 13, 20).

[12] S. Kühn, U. Håkanson, L. Rogobete and V. Sandoghdar, *Enhancement of single-molecule fluorescence using a gold nanoparticle as an optical nanoantenna*,
Physical review letters **97** (2006) 017402 (cit. on pp. 1, 7, 13).

[13] J. N. Farahani, D. W. Pohl, H.-J. Eisler and B. Hecht,
Single quantum dot coupled to a scanning optical antenna: a tunable superemitter,
Physical review letters **95** (2005) 017402 (cit. on pp. 1, 2, 13).

[14] M. Pfeiffer, K. Lindfors, H. Zhang, B. Fenk, F. Phillipp, P. Atkinson, A. Rastelli, O. G. Schmidt, H. Giessen and M. Lippitz, *Eleven nanometer alignment precision of a plasmonic nanoantenna with a self-assembled GaAs quantum dot*, Nano letters **14** (2014) 197 (cit. on pp. 1, 2, 13, 21).

[15] K. Matsuzaki, S. Vassant, H.-W. Liu, A. Dutschke, B. Hoffmann, X. Chen, S. Christiansen, M. R. Buck, J. A. Hollingsworth, S. Götzinger et al., *Strong plasmonic enhancement of biexciton emission: controlled coupling of a single quantum dot to a gold nanocone antenna*, Scientific reports **7** (2017) 42307 (cit. on pp. 1, 2, 13, 21).

[16] L. Xin, M. Lu, S. Both, M. Pfeiffer, M. J. Urban, C. Zhou, H. Yan, T. Weiss, N. Liu and K. Lindfors, *Watching a single fluorophore molecule walk into a plasmonic hotspot*,
ACS Photonics **6** (2019) 985 (cit. on pp. 1, 2, 13, 21, 23, 25, 55, 67).

[17] A. Thomas, L. Lethuillier-Karl, K. Nagarajan, R. M. Vergauwe, J. George, T. Chervy, A. Shalabney, E. Devaux, C. Genet, J. Moran et al.,
Tilting a ground-state reactivity landscape by vibrational strong coupling,
Science **363** (2019) 615 (cit. on pp. 1, 15).

[18] T. B. Hoang, G. M. Akselrod, C. Argyropoulos, J. Huang, D. R. Smith and M. H. Mikkelsen,
Ultrafast spontaneous emission source using plasmonic nanoantennas,
Nature communications **6** (2015) 1 (cit. on pp. 2, 21).

[19] R. Chikkaraddy, V. Turek, N. Kongsuwan, F. Benz, C. Carnegie, T. van de Goor, B. de Nijs, A. Demetriadou, O. Hess, U. F. Keyser et al., *Mapping nanoscale hotspots with single-molecule emitters assembled into plasmonic nanocavities using DNA origami*,
Nano letters **18** (2018) 405 (cit. on pp. 2, 21, 23–25).

[20] A. G. Curto, G. Volpe, T. H. Taminiau, M. P. Kreuzer, R. Quidant and N. F. van Hulst,
Unidirectional emission of a quantum dot coupled to a nanoantenna, Science **329** (2010) 930 (cit. on pp. 2, 21).

[21] A. Dousse, L. Lanco, J. Suffczyński, E. Semenova, A. Miard, A. Lemaıtre, I. Sagnes, C. Roblin, J. Bloch and P. Senellart, *Controlled light-matter coupling for a single quantum dot embedded in a pillar microcavity using far-field optical lithography*, Physical review letters **101** (2008) 267404 (cit. on pp. 2, 21).

[22] S. M. Douglas, H. Dietz, T. Liedl, B. Högberg, F. Graf and W. M. Shih, *Self-assembly of DNA into nanoscale three-dimensional shapes*, Nature **459** (2009) 414 (cit. on pp. 2, 21, 23).

[23] P. W. Rothemund, *Folding DNA to create nanoscale shapes and patterns*, Nature **440** (2006) 297 (cit. on pp. 2, 21, 22).

[24] A. Kuzyk, R. Schreiber, H. Zhang, A. O. Govorov, T. Liedl and N. Liu, *Reconfigurable 3D plasmonic metamolecules*, Nature materials **13** (2014) 862 (cit. on pp. 2, 23, 24, 41).

[25] A. Kuzyk, Y. Yang, X. Duan, S. Stoll, A. O. Govorov, H. Sugiyama, M. Endo and N. Liu, *A light-driven three-dimensional plasmonic nanosystem that translates molecular motion into reversible chiroptical function*, Nature communications **7** (2016) 1 (cit. on pp. 2, 24, 41).

[26] A. Kuzyk, M. J. Urban, A. Idili, F. Ricci and N. Liu, *Selective control of reconfigurable chiral plasmonic metamolecules*, Science Advances **3** (2017) e1602803 (cit. on pp. 2, 24, 41).

[27] G. Grosso, H. Moon, B. Lienhard, S. Ali, D. K. Efetov, M. M. Furchi, P. Jarillo-Herrero, M. J. Ford, I. Aharonovich and D. Englund, *Tunable and high-purity room temperature single-photon emission from atomic defects in hexagonal boron nitride*, Nature communications **8** (2017) 1 (cit. on pp. 2, 25).

[28] S. Zhao, J. Lavie, L. Rondin, L. Orcin-Chaix, C. Diederichs, P. Roussignol, Y. Chassagneux, C. Voisin, K. Müllen, A. Narita et al., *Single photon emission from graphene quantum dots at room temperature*, Nature communications **9** (2018) 1 (cit. on pp. 2, 25).

[29] M. Koperski, K. Nogajewski, A. Arora, V. Cherkez, P. Mallet, J.-Y. Veuillen, J. Marcus, P. Kossacki and M. Potemski, *Single photon emitters in exfoliated WSe 2 structures*, Nature nanotechnology **10** (2015) 503 (cit. on pp. 2, 25).

[30] K. F. Mak, K. He, J. Shan and T. F. Heinz, *Control of valley polarization in monolayer MoS 2 by optical helicity*, Nature nanotechnology **7** (2012) 494 (cit. on pp. 2, 25).

[31] H. Zeng, J. Dai, W. Yao, D. Xiao and X. Cui,
Valley polarization in MoS 2 monolayers by optical pumping,
Nature nanotechnology **7** (2012) 490 (cit. on pp. 2, 25).

[32] T. Cao, G. Wang, W. Han, H. Ye, C. Zhu, J. Shi, Q. Niu, P. Tan, E. Wang, B. Liu et al.,
Valley-selective circular dichroism of monolayer molybdenum disulphide,
Nature communications **3** (2012) 1 (cit. on pp. 2, 25).

[33] B. V. Senkovskiy et al., *Making Graphene Nanoribbons Photoluminescent*,
Nano Letters **17** (2017) 4029 (cit. on pp. 2, 26, 27).

[34] M. Pfeiffer, B. V. Senkovskiy, D. Haberer, F. R. Fischer, F. Yang, K. Meerholz, Y. Ando, A. Grüneis and K. Lindfors, *Enhanced light–matter interaction of aligned armchair graphene nanoribbons using arrays of plasmonic nanoantennas*, 2D Materials **5** (2018) 045006 (cit. on pp. 2, 13, 26, 27).

[35] J. Shi, M.-H. Lin, I.-T. Chen, N. M. Estakhri, X.-Q. Zhang, Y. Wang, H.-Y. Chen, C.-A. Chen, C.-K. Shih, A. Alù et al., *Cascaded exciton energy transfer in a monolayer semiconductor lateral heterostructure assisted by surface plasmon polariton*,
Nature communications **8** (2017) 1 (cit. on pp. 2, 26).

[36] D.-H. Lien, M. Amani, S. B. Desai, G. H. Ahn, K. Han, J.-H. He, J. W. Ager, M. C. Wu and A. Javey, *Large-area and bright pulsed electroluminescence in monolayer semiconductors*,
Nature communications **9** (2018) 1 (cit. on pp. 2, 15).

[37] Y.-C. Chen, D. G. De Oteyza, Z. Pedramrazi, C. Chen, F. R. Fischer and M. F. Crommie, *Tuning the band gap of graphene nanoribbons synthesized from molecular precursors*,
ACS nano **7** (2013) 6123 (cit. on pp. 2, 26).

[38] J. Cai, C. A. Pignedoli, L. Talirz, P. Ruffieux, H. Söde, L. Liang, V. Meunier, R. Berger, R. Li, X. Feng et al., *Graphene nanoribbon heterojunctions*, Nature nanotechnology **9** (2014) 896 (cit. on pp. 2, 26).

[39] P. Ruffieux, S. Wang, B. Yang, C. Sánchez-Sánchez, J. Liu, T. Dienel, L. Talirz, P. Shinde, C. A. Pignedoli, D. Passerone et al.,
On-surface synthesis of graphene nanoribbons with zigzag edge topology,
Nature **531** (2016) 489 (cit. on pp. 2, 26).

[40] L. Grill, M. Dyer, L. Lafferentz, M. Persson, M. V. Peters and S. Hecht,
Nano-architectures by covalent assembly of molecular building blocks,
Nature nanotechnology **2** (2007) 687 (cit. on pp. 2, 26).

[41] K. Nakada, M. Fujita, G. Dresselhaus and M. S. Dresselhaus,
Edge state in graphene ribbons: Nanometer size effect and edge shape dependence,
Physical Review B **54** (1996) 17954 (cit. on pp. 2, 26).

[42] Y.-W. Son, M. L. Cohen and S. G. Louie, *Half-metallic graphene nanoribbons*,
Nature **444** (2006) 347 (cit. on pp. 2, 26).

[43] X. Li, X. Wang, L. Zhang, S. Lee and H. Dai,
Chemically Derived, Ultrasmooth Graphene Nanoribbon Semiconductors,
Science **319** (2008) 1229 (cit. on pp. 2, 26).

[44] Y. C. Chen, D. G. De Oteyza, Z. Pedramrazi, C. Chen, F. R. Fischer and M. F. Crommie,
Tuning the band gap of graphene nanoribbons synthesized from molecular precursors,
ACS Nano **7** (2013) 6123 (cit. on pp. 2, 26).

[45] *Fabrication and optical probing of highly extended, ultrathin graphene nanoribbons in carbon nanotubes*, ACS Nano **9** (2015) 5034 (cit. on pp. 2, 26).

[46] D. Prezzi, D. Varsano, A. Ruini, A. Marini and E. Molinari,
Optical properties of graphene nanoribbons: The role of many-body effects,
Physical Review B **77** (2008) 041404 (cit. on pp. 2, 26, 27).

[47] M. Y. Han, B. Özyilmaz, Y. Zhang and P. Kim,
Energy band-gap engineering of graphene nanoribbons,
Physical Review Letters **98** (2007) 206805 (cit. on pp. 2, 26).

[48] M. Aliofkhazraei, N. Ali, W. I. Milne, C. S. Ozkan, S. Mitura and J. L. Gervasoni,
Graphene science handbook: Size-dependent properties, CRC Press, 2016 (cit. on pp. 2, 26).

[49] Y.-W. Son, M. L. Cohen and S. G. Louie, *Half-metallic graphene nanoribbons*,
Nature **444** (2006) 347 (cit. on pp. 2, 26).

[50] L. Yang, C.-H. Park, Y.-W. Son, M. L. Cohen and S. G. Louie,
Quasiparticle energies and band gaps in graphene nanoribbons,
Physical Review Letters **99** (2007) 186801 (cit. on pp. 2, 26, 27).

[51] S. Wang, L. Talirz, C. A. Pignedoli, X. Feng, K. Müllen, R. Fasel and P. Ruffieux,
Giant edge state splitting at atomically precise graphene zigzag edges,
Nature communications **7** (2016) 1 (cit. on pp. 2, 26).

[52] C. Stampfer, J. Güttinger, S. Hellmüller, F. Molitor, K. Ensslin and T. Ihn,
Energy gaps in etched graphene nanoribbons, Physical review letters **102** (2009) 056403
(cit. on pp. 2, 26).

[53] X. Li, X. Wang, L. Zhang, S. Lee and H. Dai,
Chemically derived, ultrasmooth graphene nanoribbon semiconductors,
science **319** (2008) 1229 (cit. on pp. 2, 26).

[54] A. Kimouche, M. M. Ervasti, R. Drost, S. Halonen, A. Harju, P. M. Joensuu, J. Sainio and P. Liljeroth, *Ultra-narrow metallic armchair graphene nanoribbons*,
Nature communications **6** (2015) 10177 (cit. on pp. 2, 26).

[55] O. Gröning, S. Wang, X. Yao, C. A. Pignedoli, G. B. Barin, C. Daniels, A. Cupo, V. Meunier, X. Feng, A. Narita et al.,
Engineering of robust topological quantum phases in graphene nanoribbons,
Nature **560** (2018) 209 (cit. on pp. 2, 26).

[56] D. J. Rizzo, G. Veber, T. Cao, C. Bronner, T. Chen, F. Zhao, H. Rodriguez, S. G. Louie, M. F. Crommie and F. R. Fischer, *Topological band engineering of graphene nanoribbons*,
Nature **560** (2018) 204 (cit. on pp. 2, 26).

[57] A. Puchkova, C. Vietz, E. Pibiri, B. Wünsch, M. Sanz Paz, G. P. Acuna and P. Tinnefeld,
DNA origami nanoantennas with over 5000-fold fluorescence enhancement and single-molecule detection at 25 μM, Nano letters **15** (2015) 8354 (cit. on pp. 3, 21, 23, 24).

[58] G. Acuna, F. Möller, P. Holzmeister, S. Beater, B. Lalkens and P. Tinnefeld,
Fluorescence enhancement at docking sites of DNA-directed self-assembled nanoantennas,
Science **338** (2012) 506 (cit. on pp. 3, 21, 23, 24).

[59] D.-K. Lim, K.-S. Jeon, H. M. Kim, J.-M. Nam and Y. D. Suh,
Nanogap-engineerable Raman-active nanodumbbells for single-molecule detection,
Nature materials **9** (2010) 60 (cit. on pp. 3, 21, 23).

[60] P. Zhan, T. Wen, Z.-g. Wang, Y. He, J. Shi, T. Wang, X. Liu, G. Lu and B. Ding,
DNA Origami Directed Assembly of Gold Bowtie Nanoantennas for Single-Molecule Surface-Enhanced Raman Scattering,
Angewandte Chemie International Edition **57** (2018) 2846 (cit. on pp. 3, 21, 23, 24).

[61] J. Prinz, C. Heck, L. Ellerik, V. Merk and I. Bald, *DNA origami based Au–Ag-core–shell nanoparticle dimers with single-molecule SERS sensitivity*, Nanoscale **8** (2016) 5612
(cit. on pp. 3, 21, 23).

[62] N. Aissaoui, K. Moth-Poulsen, M. Käll, P. Johansson, L. M. Wilhelmsson and B. Albinsson,
FRET enhancement close to gold nanoparticles positioned in DNA origami constructs,
Nanoscale **9** (2017) 673 (cit. on pp. 3, 21, 23).

[63] L. Novotny and B. Hecht, *Principles of nano-optics*, Cambridge university press, 2012
(cit. on pp. 6–9, 18, 31).

[64] M. Frasca, *A modern review of the two-level approximation*, Annals of Physics **306** (2003) 193 (cit. on p. 5).

[65] J. H. Eberly, *Optical resonance and two-level atoms*, Wiley-Interscience, 1975 (cit. on p. 5).

[66] M. Fox, *Quantum optics: an introduction*, vol. 15, OUP Oxford, 2006 (cit. on p. 5).

[67] R. Loudon, *The quantum theory of light*, OUP Oxford, 2000 (cit. on p. 6).

[68] K. Joulain, R. Carminati, J.-P. Mulet and J.-J. Greffet, *Definition and measurement of the local density of electromagnetic states close to an interface*, Physical Review B **68** (2003) 245405 (cit. on p. 6).

[69] P. Goy, J. Raimond, M. Gross and S. Haroche, *Observation of cavity-enhanced single-atom spontaneous emission*, Physical review letters **50** (1983) 1903 (cit. on p. 7).

[70] D. Kleppner, *Inhibited spontaneous emission*, Physical review letters **47** (1981) 233 (cit. on p. 7).

[71] J. D. Joannopoulos, P. R. Villeneuve and S. Fan, *Photonic crystals: putting a new twist on light*, Nature **386** (1997) 143 (cit. on p. 7).

[72] R. F. Oulton, V. J. Sorger, D. Genov, D. Pile and X. Zhang, *A hybrid plasmonic waveguide for subwavelength confinement and long-range propagation*, nature photonics **2** (2008) 496 (cit. on p. 7).

[73] M. I. Stockman, *Nanofocusing of optical energy in tapered plasmonic waveguides*, Physical review letters **93** (2004) 137404 (cit. on p. 7).

[74] Q. Gan, Z. Fu, Y. J. Ding and F. J. Bartoli, *Ultrawide-bandwidth slow-light system based on THz plasmonic graded metallic grating structures*, Physical review letters **100** (2008) 256803 (cit. on p. 7).

[75] A. Kabashin, P. Evans, S. Pastkovsky, W. Hendren, G. Wurtz, R. Atkinson, R. Pollard, V. Podolskiy and A. Zayats, *Plasmonic nanorod metamaterials for biosensing*, Nature materials **8** (2009) 867 (cit. on p. 7).

[76] S. Wang, P. C. Wu, V.-C. Su, Y.-C. Lai, M.-K. Chen, H. Y. Kuo, B. H. Chen, Y. H. Chen, T.-T. Huang, J.-H. Wang et al., *A broadband achromatic metalens in the visible*, Nature nanotechnology **13** (2018) 227 (cit. on pp. 7, 27).

[77] N. W. Ashcroft, N. D. Mermin et al., *Solid state physics*, 1976 (cit. on p. 7).

[78] W. Drube, F. Himpsel and P. J. Feibelman, *Inverse of the photoelectric effect in Al*, Physical review letters **60** (1988) 2070 (cit. on p. 8).

[79] U. Bovensiepen, H. Petek and M. Wolf, *Dynamics at Solid State Surfaces and Interfaces*, Wiley Online Library, 2010 (cit. on p. 8).

[80] P. B. Johnson and R.-W. Christy, *Optical constants of the noble metals*, Physical review B **6** (1972) 4370 (cit. on p. 9).

[81] L. Tao, S. Deng, H. Gao, H. Lv, X. Wen and M. Li, *Experimental Investigation of the Dielectric Constants of Thin Noble Metallic Films Using a Surface Plasmon Resonance Sensor*, Sensors **20** (2020) 1505 (cit. on p. 9).

[82] P. G. Etchegoin, E. Le Ru and M. Meyer, *An analytic model for the optical properties of gold*, The Journal of chemical physics **125** (2006) 164705 (cit. on p. 9).

[83] A. Vial, A.-S. Grimault, D. Macıas, D. Barchiesi and M. L. De La Chapelle, *Improved analytical fit of gold dispersion: Application to the modeling of extinction spectra with a finite-difference time-domain method*, Physical Review B **71** (2005) 085416 (cit. on p. 9).

[84] D. Barchiesi and T. Grosges, *Fitting the optical constants of gold, silver, chromium, titanium, and aluminum in the visible bandwidth*, Journal of Nanophotonics **8** (2014) 083097 (cit. on p. 9).

[85] H. Sehmi, W. Langbein and E. Muljarov, *Optimizing the Drude-Lorentz model for material permittivity: Method, program, and examples for gold, silver, and copper*, Physical Review B **95** (2017) 115444 (cit. on p. 9).

[86] J. D. Jackson, *Classical electrodynamics*, 1999 (cit. on p. 10).

[87] D. Tzarouchis and A. Sihvola, *Light scattering by a dielectric sphere: perspectives on the Mie resonances*, Applied Sciences **8** (2018) 184 (cit. on p. 11).

[88] C. F. Bohren and D. R. Huffman, *Absorption and scattering of light by small particles*, John Wiley & Sons, 2008 (cit. on pp. 11, 12).

[89] D. Boyer, P. Tamarat, A. Maali, B. Lounis and M. Orrit, *Photothermal imaging of nanometer-sized metal particles among scatterers*, Science **297** (2002) 1160 (cit. on p. 12).

[90] K. Lindfors, T. Kalkbrenner, P. Stoller and V. Sandoghdar, *Detection and Spectroscopy of Gold Nanoparticles Using Supercontinuum White Light Confocal Microscopy*, Phys. Rev. Lett. **93** (3 2004) 037401 (cit. on p. 12).

[91] M. Gluodenis and C. A. Foss, *The effect of mutual orientation on the spectra of metal nanoparticle rod- rod and rod- sphere pairs*, The Journal of Physical Chemistry B **106** (2002) 9484 (cit. on p. 12).

[92] M. Meier and A. Wokaun, *Enhanced fields on large metal particles: dynamic depolarization*, Optics letters **8** (1983) 581 (cit. on p. 12).

[93] T. Kokkinakis and K. Alexopoulos,
Observation of radiative decay of surface plasmons in small silver particles,
Physical Review Letters **28** (1972) 1632 (cit. on p. 12).

[94] S. Link and M. A. El-Sayed, *Shape and size dependence of radiative, non-radiative and photothermal properties of gold nanocrystals*,
International reviews in physical chemistry **19** (2000) 409 (cit. on p. 12).

[95] C. Sönnichsen, T. Franzl, T. Wilk, G. von Plessen, J. Feldmann, O. Wilson and P. Mulvaney,
Drastic reduction of plasmon damping in gold nanorods,
Physical review letters **88** (2002) 077402 (cit. on pp. 12, 13).

[96] A. Jakab, C. Rosman, Y. Khalavka, J. Becker, A. Trügler, U. Hohenester and C. Sonnichsen, *Highly sensitive plasmonic silver nanorods*, ACS nano **5** (2011) 6880 (cit. on p. 13).

[97] G. Mie, *Beiträge zur Optik trüber Medien, speziell kolloidaler Metallösungen*,
Annalen der physik **330** (1908) 377 (cit. on p. 13).

[98] U. C. Fischer and D. Pohl,
Observation of single-particle plasmons by near-field optical microscopy,
Physical review letters **62** (1989) 458 (cit. on p. 13).

[99] L. Tang, S. E. Kocabas, S. Latif, A. K. Okyay, D.-S. Ly-Gagnon, K. C. Saraswat and D. A. Miller,
Nanometre-scale germanium photodetector enhanced by a near-infrared dipole antenna,
Nature Photonics **2** (2008) 226 (cit. on p. 13).

[100] M. W. Knight, H. Sobhani, P. Nordlander and N. J. Halas,
Photodetection with active optical antennas, Science **332** (2011) 702 (cit. on p. 13).

[101] H. A. Atwater and A. Polman, "Plasmonics for improved photovoltaic devices",
Materials for Sustainable Energy: A Collection of Peer-Reviewed Research and Review Articles from Nature Publishing Group, World Scientific, 2011 1 (cit. on pp. 13, 14).

[102] J. N. Anker, W. P. Hall, O. Lyandres, N. C. Shah, J. Zhao and R. P. Van Duyne,
"Biosensing with plasmonic nanosensors",
Nanoscience and Technology: A Collection of Reviews from Nature Journals,
World Scientific, 2010 308 (cit. on p. 13).

[103] A. Hartschuh, E. J. Sánchez, X. S. Xie and L. Novotny,
High-resolution near-field Raman microscopy of single-walled carbon nanotubes,
Physical Review Letters **90** (2003) 095503 (cit. on p. 13).

[104] M. Lu, M. Pfeiffer, B. V. Senkovskiy, D. Haberer, D. Hertel, K. Meerholz, F. R. Fischer, Y. Ando, A. Grüneis and K. Lindfors, *Probing the origin of photoluminescence blinking in graphene nanoribbons: Influence of plasmonic field enhancement*, 2D Materials **7** (2020) 045009 (cit. on pp. 13, 21, 57, 67).

[105] L. Novotny, *Effective wavelength scaling for optical antennas*, Physical Review Letters **98** (2007) 266802 (cit. on p. 14).

[106] J.-S. Huang, V. Callegari, P. Geisler, C. Brüning, J. Kern, J. C. Prangsma, X. Wu, T. Feichtner, J. Ziegler, P. Weinmann et al., *Atomically flat single-crystalline gold nanostructures for plasmonic nanocircuitry*, Nature communications **1** (2010) 1 (cit. on p. 14).

[107] A. Dasgupta, M.-M. Mennemanteuil, M. Buret, N. Cazier, G. Colas-des-Francs and A. Bouhelier, *Optical wireless link between a nanoscale antenna and a transducing rectenna*, Nature communications **9** (2018) 1 (cit. on p. 14).

[108] R. Kullock, M. Ochs, P. Grimm, M. Emmerling and B. Hecht, *Electrically-driven Yagi-Uda antennas for light*, Nature communications **11** (2020) 1 (cit. on p. 14).

[109] J. C. Prangsma, J. Kern, A. G. Knapp, S. Grossmann, M. Emmerling, M. Kamp and B. Hecht, *Electrically connected resonant optical antennas*, Nano letters **12** (2012) 3915 (cit. on p. 14).

[110] J. Chen, M. Badioli, P. Alonso-González, S. Thongrattanasiri, F. Huth, J. Osmond, M. Spasenović, A. Centeno, A. Pesquera, P. Godignon et al., *Optical nano-imaging of gate-tunable graphene plasmons*, Nature **487** (2012) 77 (cit. on p. 15).

[111] D. Brinks, M. Castro-Lopez, R. Hildner and N. F. van Hulst, *Plasmonic antennas as design elements for coherent ultrafast nanophotonics*, Proceedings of the National Academy of Sciences **110** (2013) 18386 (cit. on p. 15).

[112] M. R. Beversluis, A. Bouhelier and L. Novotny, *Continuum generation from single gold nanostructures through near-field mediated intraband transitions*, Physical Review B **68** (2003) 115433 (cit. on p. 15).

[113] C. Bradac, T. Gaebel, N. Naidoo, M. Sellars, J. Twamley, L. Brown, A. Barnard, T. Plakhotnik, A. Zvyagin and J. Rabeau, *Observation and control of blinking nitrogen-vacancy centres in discrete nanodiamonds*, Nature nanotechnology **5** (2010) 345 (cit. on pp. 16, 17).

[114] T. Basché, S. Kummer and C. Bräuchle,
Direct spectroscopic observation of quantum jumps of a single molecule,
Nature **373** (1995) 132 (cit. on p. 16).

[115] W. Nagourney, J. Sandberg and H. Dehmelt,
Shelved optical electron amplifier: Observation of quantum jumps,
Physical Review Letters **56** (1986) 2797 (cit. on p. 16).

[116] T. Basché, W. Moerner, M. Orrit and U. Wild,
Single-molecule optical detection, imaging and spectroscopy, John Wiley & Sons, 2008
(cit. on pp. 16, 17).

[117] J. Vogelsang, R. Kasper, C. Steinhauer, B. Person, M. Heilemann, M. Sauer and P. Tinnefeld,
A reducing and oxidizing system minimizes photobleaching and blinking of fluorescent dyes,
Angewandte Chemie International Edition **47** (2008) 5465 (cit. on pp. 17, 24).

[118] T. Cordes, J. Vogelsang and P. Tinnefeld,
On the mechanism of Trolox as antiblinking and antibleaching reagent,
Journal of the American Chemical Society **131** (2009) 5018 (cit. on p. 17).

[119] C. Eggeling, J. Widengren, R. Rigler and C. Seidel, *Photobleaching of fluorescent dyes under conditions used for single-molecule detection: Evidence of two-step photolysis*,
Analytical chemistry **70** (1998) 2651 (cit. on p. 17).

[120] M. A. Bopp, Y. Jia, L. Li, R. J. Cogdell and R. M. Hochstrasser,
Fluorescence and photobleaching dynamics of single light-harvesting complexes,
Proceedings of the National Academy of Sciences **94** (1997) 10630 (cit. on p. 17).

[121] F. Cichos, C. von Borczyskowski and M. Orrit, *Power-law intermittency of single emitters*,
Current Opinion in Colloid & Interface Science **12** (2007) 272 (cit. on p. 17).

[122] R. Neuhauser, K. Shimizu, W. Woo, S. Empedocles and M. Bawendi, *Correlation between fluorescence intermittency and spectral diffusion in single semiconductor quantum dots*,
Physical Review Letters **85** (2000) 3301 (cit. on p. 17).

[123] W. Ambrose and W. Moerner,
Fluorescence spectroscopy and spectral diffusion of single impurity molecules in a crystal,
Nature **349** (1991) 225 (cit. on p. 17).

[124] J. P. Hoogenboom, J. Hernando, E. M. van Dijk, N. F. van Hulst and M. F. Garcıa-Parajó,
Power-Law Blinking in the Fluorescence of Single Organic Molecules,
ChemPhysChem **8** (2007) 823 (cit. on p. 17).

[125] R. H. Brown and R. Q. Twiss, *Correlation between photons in two coherent beams of light*,
Nature **177** (1956) 27 (cit. on p. 17).

[126] P. Bharadwaj and L. Novotny,
Spectral dependence of single molecule fluorescence enhancement,
Optics Express **15** (2007) 14266 (cit. on p. 18).

[127] R. Carminati, M. Nieto-Vesperinas and J.-J. Greffet,
Reciprocity of evanescent electromagnetic waves, JOSA A **15** (1998) 706 (cit. on p. 18).

[128] K. J. Russell, T.-L. Liu, S. Cui and E. L. Hu,
Large spontaneous emission enhancement in plasmonic nanocavities,
Nature Photonics **6** (2012) 459 (cit. on p. 20).

[129] N. Kongsuwan, A. Demetriadou, R. Chikkaraddy, F. Benz, V. A. Turek, U. F. Keyser, J. J. Baumberg and O. Hess, *Suppressed quenching and strong-coupling of purcell-enhanced single-molecule emission in plasmonic nanocavities*, Acs Photonics **5** (2018) 186 (cit. on p. 20).

[130] J. J. Baumberg, J. Aizpurua, M. H. Mikkelsen and D. R. Smith,
Extreme nanophotonics from ultrathin metallic gaps, Nature materials **18** (2019) 668 (cit. on p. 20).

[131] A. L. Falk, F. H. Koppens, L. Y. Chun, K. Kang, N. de Leon Snapp, A. V. Akimov, M.-H. Jo, M. D. Lukin and H. Park,
Near-field electrical detection of optical plasmons and single-plasmon sources,
Nature Physics **5** (2009) 475 (cit. on p. 21).

[132] B. Ding, Z. Deng, H. Yan, S. Cabrini, R. N. Zuckermann and J. Bokor,
Gold nanoparticle self-similar chain structure organized by DNA origami,
Journal of the American Chemical Society **132** (2010) 3248 (cit. on p. 21).

[133] R. Schreiber, J. Do, E.-M. Roller, T. Zhang, V. J. Schüller, P. C. Nickels, J. Feldmann and T. Liedl, *Hierarchical assembly of metal nanoparticles, quantum dots and organic dyes using DNA origami scaffolds*, Nature nanotechnology **9** (2014) 74 (cit. on p. 21).

[134] X. Shen, C. Song, J. Wang, D. Shi, Z. Wang, N. Liu and B. Ding, *Rolling up gold nanoparticle-dressed DNA origami into three-dimensional plasmonic chiral nanostructures*, Journal of the American Chemical Society **134** (2012) 146 (cit. on pp. 21, 23).

[135] A. Kuzyk, R. Schreiber, Z. Fan, G. Pardatscher, E.-M. Roller, A. Högele, F. C. Simmel, A. O. Govorov and T. Liedl,
DNA-based self-assembly of chiral plasmonic nanostructures with tailored optical response,
Nature **483** (2012) 311 (cit. on pp. 21, 23).

[136] A. Gopinath, E. Miyazono, A. Faraon and P. W. Rothemund,
Engineering and mapping nanocavity emission via precision placement of DNA origami,
Nature **535** (2016) 401 (cit. on pp. 21, 23, 24).

[137] H. Bui, C. Onodera, C. Kidwell, Y. Tan, E. Graugnard, W. Kuang, J. Lee, W. B. Knowlton, B. Yurke and W. L. Hughes,
Programmable periodicity of quantum dot arrays with DNA origami nanotubes,
Nano letters **10** (2010) 3367 (cit. on p. 21).

[138] J. Sharma, Y. Ke, C. Lin, R. Chhabra, Q. Wang, J. Nangreave, Y. Liu and H. Yan,
DNA-tile-directed self-assembly of quantum dots into two-dimensional nanopatterns,
Angewandte Chemie International Edition **47** (2008) 5157 (cit. on p. 21).

[139] H. T. Maune, S.-p. Han, R. D. Barish, M. Bockrath, W. A. Goddard III, P. W. Rothemund and E. Winfree, *Self-assembly of carbon nanotubes into two-dimensional geometries using DNA origami templates*, Nature nanotechnology **5** (2010) 61 (cit. on p. 21).

[140] H. Yan, S. H. Park, G. Finkelstein, J. H. Reif and T. H. LaBean,
DNA-templated self-assembly of protein arrays and highly conductive nanowires,
science **301** (2003) 1882 (cit. on p. 21).

[141] A. Kuzyk, K. T. Laitinen and P. Törmä,
DNA origami as a nanoscale template for protein assembly,
Nanotechnology **20** (2009) 235305 (cit. on p. 21).

[142] A. Kuzyk, R. Jungmann, G. P. Acuna and N. Liu, *DNA origami route for nanophotonics*,
ACS photonics **5** (2018) 1151 (cit. on p. 22).

[143] S. M. Douglas, A. H. Marblestone, S. Teerapittayanon, A. Vazquez, G. M. Church and W. M. Shih, *Rapid prototyping of 3D DNA-origami shapes with caDNAno*,
Nucleic acids research **37** (2009) 5001 (cit. on p. 23).

[144] P. C. Nickels, B. Wünsch, P. Holzmeister, W. Bae, L. M. Kneer, D. Grohmann, P. Tinnefeld and T. Liedl,
Molecular force spectroscopy with a DNA origami–based nanoscopic force clamp,
Science **354** (2016) 305 (cit. on p. 23).

[145] E.-M. Roller, L. V. Besteiro, C. Pupp, L. K. Khorashad, A. O. Govorov and T. Liedl,
Hotspot-mediated non-dissipative and ultrafast plasmon passage,
Nature physics **13** (2017) 761 (cit. on p. 23).

[146] G. P. Acuna, M. Bucher, I. H. Stein, C. Steinhauer, A. Kuzyk, P. Holzmeister, R. Schreiber, A. Moroz, F. D. Stefani, T. Liedl et al., *Distance dependence of single-fluorophore quenching by gold nanoparticles studied on DNA origami*, ACS nano **6** (2012) 3189 (cit. on p. 24).

[147] P. Holzmeister, G. P. Acuna, D. Grohmann and P. Tinnefeld, *Breaking the concentration limit of optical single-molecule detection*, Chemical Society Reviews **43** (2014) 1014 (cit. on p. 24).

[148] F. Nicoli, T. Zhang, K. Hübner, B. Jin, F. Selbach, G. Acuna, C. Argyropoulos, T. Liedl and M. Pilo-Pais, *DNA-Mediated Self-Assembly of Plasmonic Antennas with a Single Quantum Dot in the Hot Spot*, Small **15** (2019) 1804418 (cit. on p. 24).

[149] I. Kaminska, J. Bohlen, S. Mackowski, P. Tinnefeld and G. P. Acuna, *Strong plasmonic enhancement of a single peridinin–chlorophyll a–protein complex on DNA origami-based optical antennas*, ACS nano **12** (2018) 1650 (cit. on p. 24).

[150] S. E. Ochmann, C. Vietz, K. Trofymchuk, G. P. Acuna, B. Lalkens and P. Tinnefeld, *Optical nanoantenna for single molecule-based detection of zika virus nucleic acids without molecular multiplication*, Analytical chemistry **89** (2017) 13000 (cit. on p. 24).

[151] K. Trofymchuk, V. Glembockyte, L. Grabenhorst, F. Steiner, C. Vietz, C. Close, M. Pfeiffer, L. Richter, M. L. Schütte, F. Selbach et al., *Addressable Nanoantennas with Cleared Hotspots for Single-Molecule Detection on a Portable Smartphone Microscope*, bioRxiv (2020) (cit. on p. 24).

[152] Y.-W. Son, M. L. Cohen and S. G. Louie, *Energy gaps in graphene nanoribbons*, Physical review letters **97** (2006) 216803 (cit. on p. 25).

[153] C. Chakraborty, L. Kinnischtzke, K. M. Goodfellow, R. Beams and A. N. Vamivakas, *Voltage-controlled quantum light from an atomically thin semiconductor*, Nature nanotechnology **10** (2015) 507 (cit. on p. 25).

[154] X. He, N. F. Hartmann, X. Ma, Y. Kim, R. Ihly, J. L. Blackburn, W. Gao, J. Kono, Y. Yomogida, A. Hirano et al., *Tunable room-temperature single-photon emission at telecom wavelengths from sp 3 defects in carbon nanotubes*, Nature Photonics **11** (2017) 577 (cit. on p. 25).

[155] K.-D. Park, T. Jiang, G. Clark, X. Xu and M. B. Raschke, *Radiative control of dark excitons at room temperature by nano-optical antenna-tip Purcell effect*, Nature nanotechnology **13** (2018) 59 (cit. on p. 26).

[156] J. Huang, G. M. Akselrod, T. Ming, J. Kong and M. H. Mikkelsen, *Tailored emission spectrum of 2D semiconductors using plasmonic nanocavities*, ACS Photonics **5** (2018) 552 (cit. on p. 26).

[157] P. Gonçalves, L. Bertelsen, S. Xiao and N. A. Mortensen, *Plasmon-exciton polaritons in two-dimensional semiconductor/metal interfaces*, Physical Review B **97** (2018) 041402 (cit. on p. 26).

[158] J. Cuadra, D. G. Baranov, M. Wersäll, R. Verre, T. J. Antosiewicz and T. Shegai, *Observation of tunable charged exciton polaritons in hybrid monolayer WS2- plasmonic nanoantenna system*, Nano letters **18** (2018) 1777 (cit. on p. 26).

[159] W. Han, R. K. Kawakami, M. Gmitra and J. Fabian, *Graphene spintronics*, Nature Nanotechnology **9** (2014) 794, ISSN: 1748-3395 (cit. on p. 26).

[160] S. Kawai, S. Saito, S. Osumi, S. Yamaguchi, A. S. Foster, P. Spijker and E. Meyer, *Atomically controlled substitutional boron-doping of graphene nanoribbons*, Nature communications **6** (2015) 1 (cit. on p. 26).

[161] T. H. Vo, U. G. E. Perera, M. Shekhirev, M. Mehdi Pour, D. A. Kunkel, H. Lu, A. Gruverman, E. Sutter, M. Cotlet, D. Nykypanchuk et al., *Nitrogen-doping induced self-assembly of graphene nanoribbon-based two-dimensional and three-dimensional metamaterials*, Nano Letters **15** (2015) 5770 (cit. on p. 26).

[162] J. Cai, P. Ruffieux, R. Jaafar, M. Bieri, T. Braun, S. Blankenburg, M. Muoth, A. P. Seitsonen, M. Saleh, X. Feng et al., *Atomically precise bottom-up fabrication of graphene nanoribbons*, Nature **466** (2010) 470 (cit. on p. 26).

[163] M. C. Chong, N. Afshar-Imani, F. Scheurer, C. Cardoso, A. Ferretti, D. Prezzi and G. Schull, *Bright electroluminescence from single graphene nanoribbon junctions*, Nano letters **18** (2018) 175 (cit. on p. 27).

[164] P. Ruffieux, J. Cai, N. C. Plumb, L. Patthey, D. Prezzi, A. Ferretti, E. Molinari, X. Feng, K. Müllen, C. A. Pignedoli et al., *Electronic structure of atomically precise graphene nanoribbons*, Acs Nano **6** (2012) 6930 (cit. on p. 27).

[165] B. V. Senkovskiy, D. Y. Usachov, A. V. Fedorov, T. Marangoni, D. Haberer, C. Tresca, G. Profeta, V. Caciuc, S. Tsukamoto, N. Atodiresei et al., *Boron-doped graphene nanoribbons: electronic structure and Raman fingerprint*, ACS nano **12** (2018) 7571 (cit. on p. 26).

[166] J. Overbeck, G. Borin Barin, C. Daniels, M. L. Perrin, L. Liang, O. Braun, R. Darawish, B. Burkhardt, T. Dumslaff, X.-Y. Wang et al., *Optimized substrates and measurement approaches for Raman spectroscopy of graphene nanoribbons*, physica status solidi (b) **256** (2019) 1900343 (cit. on p. 26).

[167] R. Denk, M. Hohage, P. Zeppenfeld, J. Cai, C. A. Pignedoli, H. Söde, R. Fasel, X. Feng, K. Müllen, S. Wang et al., *Exciton-dominated optical response of ultra-narrow graphene nanoribbons*, Nature communications **5** (2014) 1 (cit. on p. 26).

[168] S. K. Alavi, B. V. Senkovskiy, M. Pfeiffer, D. Haberer, F. R. Fischer, A. Grüneis and K. Lindfors, *Probing the origin of photoluminescence brightening in graphene nanoribbons*, 2D Materials **6** (2019) 035009 (cit. on pp. 26, 27).

[169] S. Zhao, G. B. Barin, T. Cao, J. Overbeck, R. Darawish, T. Lyu, S. Drapcho, S. Wang, T. Dumslaff, A. Narita et al., *Optical imaging and spectroscopy of atomically precise armchair graphene nanoribbons*, Nano letters **20** (2020) 1124 (cit. on p. 26).

[170] Z. Fei, M. Goldflam, J.-S. Wu, S. Dai, M. Wagner, A. McLeod, M. Liu, K. Post, S. Zhu, G. Janssen et al., *Edge and surface plasmons in graphene nanoribbons*, Nano letters **15** (2015) 8271 (cit. on p. 26).

[171] E. Abbe, *Beiträge zur Theorie des Mikroskops und der mikroskopischen Wahrnehmung*, Archiv für mikroskopische Anatomie **9** (1873) 413 (cit. on p. 29).

[172] T. A. Klar, S. Jakobs, M. Dyba, A. Egner and S. W. Hell, *Fluorescence microscopy with diffraction resolution barrier broken by stimulated emission*, Proceedings of the National Academy of Sciences **97** (2000) 8206 (cit. on p. 30).

[173] G. Patterson, M. Davidson, S. Manley and J. Lippincott-Schwartz, *Superresolution imaging using single-molecule localization*, Annual review of physical chemistry **61** (2010) 345 (cit. on p. 31).

[174] K. I. Mortensen, L. S. Churchman, J. A. Spudich and H. Flyvbjerg, *Optimized localization analysis for single-molecule tracking and super-resolution microscopy*, Nature methods **7** (2010) 377 (cit. on p. 31).

[175] B. Zhang, J. Zerubia and J.-C. Olivo-Marin, *Gaussian approximations of fluorescence microscope point-spread function models*, Applied optics **46** (2007) 1819 (cit. on p. 31).

[176] N. Bobroff, *Position measurement with a resolution and noise-limited instrument*, Review of Scientific Instruments **57** (1986) 1152 (cit. on p. 32).

[177] R. E. Thompson, D. R. Larson and W. W. Webb, *Precise Nanometer Localization Analysis for Individual Fluorescent Probes*, Biophysical Journal **82** (2002) 2775 (cit. on p. 32).

[178] R. J. Ober, S. Ram and E. S. Ward, *Localization Accuracy in Single-Molecule Microscopy*, Biophysical Journal **86** (2004) 1185 (cit. on p. 32).

[179] A. Yildiz, J. N. Forkey, S. A. McKinney, T. Ha, Y. E. Goldman and P. R. Selvin, *Myosin V walks hand-over-hand: single fluorophore imaging with 1.5-nm localization*, science **300** (2003) 2061 (cit. on p. 32).

[180] M. Raab, C. Vietz, F. D. Stefani, G. P. Acuna and P. Tinnefeld,
Shifting molecular localization by plasmonic coupling in a single-molecule mirage,
Nature Communications **8** (2017) 13966 (cit. on p. 32).

[181] C. Ropp, Z. Cummins, S. Nah, J. T. Fourkas, B. Shapiro and E. Waks,
Nanoscale probing of image-dipole interactions in a metallic nanostructure,
Nature Communications **6** (2015) 6558 (cit. on p. 32).

[182] E. Wertz, B. P. Isaacoff, J. D. Flynn and J. S. Biteen, *Single-molecule super-resolution microscopy reveals how light couples to a plasmonic nanoantenna on the nanometer scale*,
Nano letters **15** (2015) 2662 (cit. on p. 32).

[183] L. Saemisch, M. Liebel and N. F. van Hulst, *Isolating strong nanoantenna–molecule interactions by ensemble-level single-molecule detection*, Nanoscale **12** (2020) 3723
(cit. on p. 32).

[184] H. Lin, S. P. Centeno, L. Su, B. Kenens, S. Rocha, M. Sliwa, J. Hofkens and H. Uji-i,
Mapping of Surface-Enhanced Fluorescence on Metal Nanoparticles using Super-Resolution Photoactivation Localization Microscopy, ChemPhysChem **13** (2012) 973 (cit. on p. 32).

[185] H. Cang, A. Labno, C. Lu, X. Yin, M. Liu, C. Gladden, Y. Liu and X. Zhang,
Probing the electromagnetic field of a 15-nanometre hotspot by single molecule imaging,
Nature **469** (2011) 385 (cit. on p. 32).

[186] B. Fu, B. P. Isaacoff and J. S. Biteen, *Super-Resolving the Actual Position of Single Fluorescent Molecules Coupled to a Plasmonic Nanoantenna*, ACS Nano **11** (2017) 8978
(cit. on p. 32).

[187] M. Wahl, *Time-correlated single photon counting*, Technical Note (2014) 1 (cit. on p. 33).

[188] D. O'Connor, W. Ware and J. Andre,
Deconvolution of fluorescence decay curves. A critical comparison of techniques,
Journal of Physical Chemistry **83** (1979) 1333 (cit. on p. 34).

[189] S. Preus, *DecayFit-Fluorescence Decay Analysis Software 1.4*,
FluorTools: www.fluortools.com (2014) (cit. on p. 34).

[190] J. Becker, A. Trügler, A. Jakab, U. Hohenester and C. Sönnichsen,
The optimal aspect ratio of gold nanorods for plasmonic bio-sensing,
Plasmonics **5** (2010) 161 (cit. on p. 36).

[191] I. Ament, J. Prasad, A. Henkel, S. Schmachtel and C. Sonnichsen,
Single unlabeled protein detection on individual plasmonic nanoparticles,
Nano letters **12** (2012) 1092 (cit. on p. 36).

[192] C. L. Baciu, J. Becker, A. Janshoff and C. Sönnichsen, *Protein–membrane interaction probed by single plasmonic nanoparticles*, Nano Letters **8** (2008) 1724 (cit. on p. 36).

[193] K. Lindfors, T. Kalkbrenner, P. Stoller and V. Sandoghdar, *Detection and spectroscopy of gold nanoparticles using supercontinuum white light confocal microscopy*, Physical review letters **93** (2004) 037401 (cit. on p. 36).

[194] R. W. Taylor and V. Sandoghdar, *Interferometric scattering microscopy: seeing single nanoparticles and molecules via Rayleigh scattering*, Nano letters **19** (2019) 4827 (cit. on p. 36).

[195] P. Zhan, M. J. Urban, S. Both, X. Duan, A. Kuzyk, T. Weiss and N. Liu, *DNA-assembled nanoarchitectures with multiple components in regulated and coordinated motion*, Science Advances **5** (2019) eaax6023 (cit. on p. 41).

[196] P. Zhan, S. Both, T. Weiss and N. Liu, *DNA-Assembled Multilayer Sliding Nanosystems*, Nano letters **19** (2019) 6385 (cit. on p. 41).

[197] M. J. Urban, S. Both, C. Zhou, A. Kuzyk, K. Lindfors, T. Weiss and N. Liu, *Gold nanocrystal-mediated sliding of doublet DNA origami filaments*, Nature communications **9** (2018) 1 (cit. on p. 41).

[198] B. Yurke, A. J. Turberfield, A. P. Mills, F. C. Simmel and J. L. Neumann, *A DNA-fuelled molecular machine made of DNA*, Nature **406** (2000) 605 (cit. on p. 43).

[199] *Atto 647 N spectra*, https://www.atto-tec.com () (cit. on p. 44).

[200] O. Janssen, A. Wachters and H. Urbach, *Efficient optimization method for the light extraction from periodically modulated LEDs using reciprocity*, Optics express **18** (2010) 24522 (cit. on p. 44).

[201] C. Steinhauer, R. Jungmann, T. L. Sobey, F. C. Simmel and P. Tinnefeld, *DNA origami as a nanoscopic ruler for super-resolution microscopy*, Angewandte Chemie International Edition **48** (2009) 8870 (cit. on p. 51).

[202] M. Raab, I. Jusuk, J. Molle, E. Buhr, B. Bodermann, D. Bergmann, H. Bosse and P. Tinnefeld, *Using DNA origami nanorulers as traceable distance measurement standards and nanoscopic benchmark structures*, Scientific reports **8** (2018) 1 (cit. on p. 51).

[203] S. H. Brewer, W. R. Glomm, M. C. Johnson, M. K. Knag and S. Franzen, *Probing BSA binding to citrate-coated gold nanoparticles and surfaces*, Langmuir **21** (2005) 9303 (cit. on p. 51).

[204] J. J. Schmied, M. Raab, C. Forthmann, E. Pibiri, B. Wünsch, T. Dammeyer and P. Tinnefeld, *DNA origami–based standards for quantitative fluorescence microscopy*, Nature protocols **9** (2014) 1367 (cit. on p. 63).

[205] S. J. Hurst, A. K. Lytton-Jean and C. A. Mirkin, *Maximizing DNA loading on a range of gold nanoparticle sizes*, Analytical chemistry **78** (2006) 8313 (cit. on p. 63).

List of Acronyms

2D Two-dimensional.

APD Avalanched photon diode.

AuNP Gold nanoparticle.

AuNR Gold nanorod.

BSA Bovine serum albumin.

FRET Förster resonance energy transfer.

GNR Graphene nanoribbons.

IRF Instrument response function.

iSCAT Interferometric scattering microscopy.

LDOS Local density of state.

PSF Point-spread function.

QED Quantum electrodynamics.

RF Radio-frequency.

SEM Scanning electron microscopy.

SMLM Single molecule localization microscopy.

TCSPC Time-correlated single photon counting.

TEM Transmission electron microscopy.

TMD Transition metal dichalcogenides.

Acknowledgements

I would like to express my heartiest gratitude and sincere thanks to Prof. Klas Lindfors for all his great supports, generous, long guidance, long discussions, and all encouragement. I appreciate his help in science, optics labs, writing, and life and all the support I received during these years. I appreciate that he always shares his ideas and thoughts honestly and directly.

I would like to thank Prof. Malte Gather, Prof. Axel Griesbeck and Dr. Nils Kronnberg for being so kind to be the examination committee.

I would like to thank my collaborators that make the work possible. Particular thanks to the collaborators Prof. Na Liu, Dr. Ling Xin, and Dr. Chao Zhou in Stuttgart. It has been very challenging for this long-distance collaboration with such a fragile sample. It is also a very challenging project in all aspects. I am also grateful to Prof. Alexander Grüneis and Dr. Boris V. Senkovskiy for providing the GNR samples.

I would like to thank Prof. Klaus Meerholtz and Dr. Dirk Hertl for their discussions, collaborations and for giving me access to many experiment facilities. I would like to thank Prof. Yoichi Ando for granting access to cleanroom facilities and all the help from his postdoc fellow Dr. Dingxun Fan.

I would like to express my gratitude to the staff members of the Physical chemistry institute and the Physics institute II. Particular thanks to Viktor Klippert's Werkstatt team, who has always surprised me with creative and complex solutions for the experimental setup.

I am very grateful to Dr. Markus Pfeiffer for all his guidance, long-lasting discussions, and all the fun in the lab. I owe special thanks to all the Lindforces: Dr. Igor Sharvin, Dr. Seyed Alavi, and Lukas Böhner. I would like to also thank Ionela for all the interesting chats. She has always been a role model for me being a female scientist.

I would like to thank the Cologne Graduate School Chemistry (CGSC) and especially Dr. Heike Henneken for taking care of the paperwork, scientific integrity training, and helpful advice.

Finally, I would like to thank my parents for supporting me to pursue my Ph.D. in Germany.

Lebenslauf

Persönliche Daten:

Name	Lu
Vorname	Mo
Geburtsdatum/-ort	17.4.1989/ Nei Mongol
Familienstand	ledig
Addresse	Volksgartenstr. 60 50677 Köln, Deutschland

Postdoktorale Laufbahn:

11/2020 – heute	Wissenschaflicher Mitarbeiterin, Institut für Physikalische Chemie, Universität zu Köln, Deutschland

Ausbildung:

09/2007 – 07/2011	B.Sc. Chemie, University of Science and Technology of China, China
04/2013 – 06/2015	M.Sc. Materialwissenschaften, Universität Augsburg, Deutschland
01/2016 – 11/2020	Ph.D. Chemie, Institut für Physikalische Chemie, Universität zu Köln, Deutschland

Lu, Mo